EXPERIMENTS ON SUPERCONDUCTING JOSEPHSON PHASE QUANTUM BITS

Den Naturwissenschaftlichen Fakultäten der
Friedrich-Alexander-Universität Erlangen-Nürnberg

zur

Erlangung des Doktorgrades

vorgelegt von

Jürgen Lisenfeld

aus Nürnberg

Als Dissertation genehmigt von den Naturwissenschaftlichen Fakultäten der
Universität Erlangen-Nürnberg

Tag der mündlichen Prüfung: 19.12.2007

Vorsitzender der Promotionskommission: Prof. Dr. Eberhard Bänsch

Erstberichterstatter: Prof. Dr. A. V. Ustinov

Zweitberichterstatter: Prof. Dr. C. Cosmelli

Contents

Chapter 1

Introduction

Nature, on atomic scale, is described very accurately by the quantum theory. This description requires the use of concepts which have no equivalent in our everyday perception of physical reality. Entanglement, for instance, binds two objects together plainly through their common history. This connection goes beyond locality as it manifests itself instantaneously and without energy exchange. The superposition principle, as another concept, allows a system to be in two or more distinct states simultaneously.

In his famous "Cat Paradox", Erwin Schrödinger [1] emphasized the strange appearance of quantum theoretical laws when they were transferred to our everyday world. In his gedanken experiment, the quantum state of a radioactive substance is linked through an entanglement apparatus to the health of a cat. If this system would be allowed to evolve quantum mechanically and not being watched, the animal would end up in a state that is a superposition of a living and a dead cat. Though there were no confirmed sightings of half-dead half-living cats, we know that quantum theory correctly describes the atomic world. The question arises where the reign of quantum theory ends and the classical world begins. Moreover, would it be possible to design an experiment in which a macroscopic object consisting of some 10^{23} particles behaves quantum mechanically just like a single atom does ?

The aim of this thesis was to perform such an experiment. By making use of superconductivity, which is a macroscopic quantum effect by itself, we were able to operate an electrical circuit in the coherent quantum regime. We applied recently developed novel experimental techniques and sample designs to confirm the ability of preparing the circuit in an arbitrary superposition of two quantum states and monitor its coherent evolution in the time domain.

1.1 Macroscopic quantum coherence in superconducting circuits

In the superconducting state, the conduction electrons of a metal give up their individuality and condense into a macroscopic quantum state which is described by a single wavefunction. As the electrons then move uniformly, they are no more subject to scattering and allow the current to flow without electrical resistance. A Josephson junction is formed when two superconductors are separated by a weak link, as for instance, a thin dielectric barrier. The single degree of freedom of such a system is the phase difference between the wavefunctions of the two superconductors, which is also called the

Josephson phase. In Chapter 2, the principles of the Josephson junction are reviewed in detail.

First experiments to investigate whether the Josephson phase obeys quantum theory were done in the year 1981 [2]. By then, it could be shown that the junction switches from a discrete superconducting state to a resistive continuum by tunneling through a potential barrier [3], in analogy to the decay of a radioactive atom. Moreover, the existence of quantized energy levels of the superconducting state was proven directly by spectroscopic measurements [4, 5]. More than one decade later, in the year 1999 a superposition of two macroscopic states was first demonstrated [6, 7] in a superconducting ring which is interrupted by a Josephson junction, a so-called *rf-SQUID* [8, 9]. The persistent current which circulates in such a device was proven to flow in a superposition of clockwise and counter-clockwise directions when an appropriate magnetic field is applied.

These experimental findings boosted the research on macroscopic quantum coherence in superconducting circuits, and within a few years time it was achieved to observe Rabi oscillation in current-biased Josephson junctions [10], rf-SQUIDs [11], junctions operated in the charge regime [12] and hybrid flux-charge systems [13]. Beneath the appealing feasibility of creating custom-tailored quantum objects, the rapid advancement was stimulated by the potentiality of these circuits to be used as quantum bits in a realization of a solid-state quantum computer.

1.2 The Josephson phase qubit

The aim of this thesis was to experimentally observe and manipulate the coherent temporal evolution of Josephson junction circuits. For the system to be studied we chose the flux-biased phase qubit, which consists of a Josephson junction integrated in a superconducting loop. This qubit realization has certain advantages which make it an ideal test bed for the experimental apparatus. Most prominently, relatively large Josephson junctions can be used in phase qubits, which are easy to fabricate using standard lithographic technology. In fact, working qubit samples could be obtained from a commercial foundry [14], where they were produced according to our designs.

Chapter 3 explains in detail the physical principles of this system, how it is operated as a qubit and how its state is measured by using an integrated dc-SQUID as sensitive flux detector. That chapter also includes our sample layouts and discusses relevant parts of the experimental setup.

1.3 Quantum computation

The idea of quantum computation[1] arose when the difficulty of simulating a quantum system with a deterministic classical computer was discussed. To describe a system of n two-level quantum systems (qubits) classically, a number of 2^n variables are necessary. This exponential scaling has the consequence that for each additional qubit the required memory and so the computational complexity is doubled, quickly exceeding the tractable limit of classical computers. R. P. Feynman noted [17] that this problem could be overcome by using a quantum computer - a manipulatable system of coupled quantum objects, onto which the system to be simulated would be mapped. Looking at such a hypothetical quantum computer from the reverse side, it came in view that

[1] For an introduction to quantum computing, see for example [15] and [16].

it might also be useful to tackle other computational problems which are intractable to classical computers. This notion was later confirmed [18], showing that a quantum computer could be used as a general purpose calculator, in principle exceeding the capabilities of any classical computer.

What is the basis of the power of a quantum computer ? Similar to a normal computer, the quantum computer encodes information in a multitude of bits which constitute its memory. It performs calculations by unravelling them into a series of logical operations on the memory, consisting of bit comparisons and conditional bit-flips. The key difference is that in a quantum computer the information is encoded in the state of objects which behave according to the laws of quantum physics. Like Schrödinger's cat, a quantum bit can be in a superposition of both its logical states "0" and "1". Hence, while a classical memory consisting of n bits allows to store *one* out of 2^n numbers, n quantum bits can store *all* 2^n numbers simultaneously. Logical operations on a quantum memory therefore work *in parallel* to all these numbers, whereas a classical computer would need to repeat the calculation 2^n times. A quantum computer can therefore work exponentially faster and lastly allow to solve calculation problems in seconds which would take thousands of years for todays fastest computers.

Evidently, it is impossible to directly access all the information which is stored in a quantum computer's memory, because its measurement will force the superposition to collapse into a classical state. However, clever programming allows to increase the probability that the final classical state after measurement contains the desired information. Many algorithms have been devised so far which proved that this is possible [19]. Peter Shor created a significant stir in 1994 by proposing a quantum algorithm which allows to factorize very large numbers in short time. While it is an easy task to multiply two numbers, the required time to find the prime factors of a large number grows exponentially with its digits when classical algorithms are applied. This asymmetry is the basis of the security of today's widely used RSA encryption algorithm, which is also used in electronic money transfer and credit card payments. Hence strikingly, a quantum computer running Shor's algorithm could be used to decipher encrypted information and to crack PIN codes. The struggle to investigate the possibilities of building a quantum computer therefore renders vital to no less than preserving security in the information age.

1.4 Implementation of a quantum computer

Physicists have demonstrated the ability to implement and control quantum bits in a variety of approaches. Among these are trapped ions, photons, nuclear spins of molecules, atoms in beams, quantum dots and superconducting circuits. A comprehensive comparison of these technologies, each having its strengths and drawbacks, is given in [20]. To be suitable for building a large-scale quantum computer, a qubit system must comply with five necessary requirements which are listed in DiVincenzo's checklist [21]. These are briefly reviewed in the following and discussed with regard to superconducting phase qubits, the system to be studied in the frame of this thesis.

A scalable physical system with well characterized qubits

A qubit can be made of any quantum object which has at least two individually addressable and distinguishable states. If the system has more than two states, the population probability of these additional levels must be kept small to avoid computational errors.

Phase qubits are characterized by mapping out their energy level structure with microwave spectroscopy. Section 4.4 of this thesis is dedicated to a comprehensive description of our spectroscopic experiments which include the observation of multi-photon transitions, measurements of qubit decoherence which appears as inhomogeneous resonance broadening and a possibility to determine the coupling (Rabi-) frequency by the resonance shift. Population of additional energy levels is avoided in phase qubits by limiting the driving strength and hence the operation speed as discussed in Sec. 4.6.1.

The excellent scalability is the prominent advantage of superconducting quantum bits. Josephson junctions are manufactured with lithographic fabrication procedures similar to conventional computer processors, and circuits involving thousands of junctions can be reliably produced. Moreover, an attractive possibility is to combine the already developed rapid single flux quantum logic (RSFQ) [22] with superconducting qubits. This technology in principle allows to integrate very fast qubit control and readout circuits in the same Josephson junction-based technology and eventually arrive at a monolithic integrated quantum computing chip.

The ability to initialize the state of the qubits

The quantum memory must be reset to a known initial state prior to computation. Since the logical states of phase qubits are separated by an energy gap ΔE which corresponds typically to a temperature $\Delta E/k_B \approx 0.5$ K, initialization in the ground state is accomplished by cooling the sample well below this temperature and letting the system relax. Recently, a procedure for active cooling in analogy to optical cooling of trapped ions has been demonstrated for superconducting flux qubits [23]. This technique allows to prepare the ground state with good fidelity even at elevated temperatures.

Long relevant coherence times, much longer than the gate operation time

Decoherence occurs through undesired interaction of the qubit with its environment and can lead to an irreversible collapse into a classical state. For superconducting qubits, preventing decoherence is the major difficulty, which appears as the downside of their good manageability owing to integration in a solid-state environment. Error-correcting techniques have been devised [24, 25] which are based on encoding one logical qubit in many (at least 5) physical qubits. These allow for arbitrarily long fault-tolerant quantum computation when a minimum number of $\approx 10^4 - 10^5$ quantum gates can be applied before decoherence occurs. The best currently existing phase qubits [26] have coherence times of about 200 ns, during which approximately 100 gate operations can be done. As the recent development has shown [27], understanding the sources of decoherence can lead to a significant improvement of qubit fidelity.

In Chapter 4 of this thesis, measurements of phase qubit coherence times are presented. This includes a first systematical study of the influence of temperature on qubit decoherence, shedding new light on its origins.

A "universal" set of quantum gates

Algorithms are executed on classical as well as quantum computers by decomposing them into a series of logical operations on the memory, so-called gates. A set of gates is "universal" when it contains all necessary ingredients to realize any calculation by

repeated executions of these basic operations, whereas it is sufficient to consider only single- or two-bit operations.

In quantum computers, single bit operations like the NOT-gate are realized through driven Rabi oscillation. Going beyond the possibilities of classical computation, the same mechanism is used to generate an equal superposition of both logical qubit states. This operation can be described as a half a bit inversion, which is therefore also called a $\sqrt{\mathrm{NOT}}$-gate. As quantum bits have two degrees of freedom, a further single-qubit gate is necessary, which is called the z-gate or *phase gate*. An experimental demonstration of all these gates using phase qubits is presented in detail in Chapter 4 of this thesis.

To complete the universal set, nearly any two qubit quantum gate can be used [28]. One example is the iSWAP gate, which was demonstrated experimentally on two capacitively coupled phase qubits [29].

What comes along the requirement of two-qubit gates is the need for a controllable coupling between qubits. For phase qubits, several strategies can be followed. A straightforward scheme uses a fixed capacitive coupling which is controlled by tuning the qubits in and out of a common resonance. Also, an inductive coupling via tunable Josephson-junction-based flux transformers [30, 31, 32] and entangling bus [33] have been proposed.

A qubit-specific measurement capability

After a quantum algorithm is completed, all involved qubits must be measured. While it is possible to compensate a reduced readout fidelity by rerunning the algorithm [21], it is important that the measurement of one qubit does not change the rest of the memory.

In our experiments on phase qubits, we use a fast and high-fidelity readout technique [34, 35, 36] which is based on application of a nanosecond-long magnetic flux pulse. It has been shown that measurement crosstalk can hereby be avoided when measuring all phase qubits simultaneously [29].

A detailed discussion of this readout technique and the temperature-dependence of its fidelity is given in Sec. 4.3.

1.5 Outlook

The preceding discussion of the DiVincenzo criteria showed that currently existing phase qubits, and likewise other superconducting qubit approaches, are promising candidates to realize a solid-state quantum computer. However, their short coherence times still hinder scaling up to multi-qubit circuits. As research progresses continues, it is expected that sources of decoherence become better understood, eventually allowing to increase qubit fidelity further.

Even if it will turn out that building a practical quantum computer using superconducting circuits stays beyond reach, strong research effort remains justified. In the past 20 years, the Josephson junction played an important role as an ideal system to study quantum tunneling. The new experimental achievements are likely to render these junctions the system of choice for the study of macroscopic quantum coherence.

Chapter 2

Principles of the phase qubit

This chapter starts with a brief review of superconductivity and the basics of Josephson junctions. The dynamics of the phase difference across the superconducting weak link are discussed, providing the basis of the phase quantum bit.

2.1 Superconductivity

Heike Kamerlingh Onnes in the year 1911 discovered that the electrical resistance of mercury, when cooled below a certain temperature, drops suddenly to zero. He understood that the metal has passed into a new state, which he called the superconductive state. The next major discovery was that a magnetic field is expelled from a superconductor, as it had been observed in the year 1933 by W. Meissner and R. Ochsenfeld. A phenomenological description of this so-called Meissner effect was given two years later by F. and H. London and is cast into the London equations

$$\frac{\mathrm{d}(\Lambda\vec{j_s})}{\mathrm{dt}} = \vec{E}, \tag{2.1}$$

expressing that in a conductor with zero resistance the temporal deviation of the current density $\vec{j_s}$ is directly proportional to the electrical field $\vec{E}$, and

$$\mathrm{rot}(\Lambda\vec{j_s}) = -\vec{B} \tag{2.2}$$

which explains the cancellation of the magnetic Field $\vec{B}$ deep inside the superconductor by the induced circulating current $\mathrm{rot}(\Lambda\vec{j_s})$. In these equations, the paramter Λ is given by

$$\Lambda = \frac{m_s}{n_s e_s^2}, \tag{2.3}$$

where m_s and n_s are respectively the mass and density of the particles carrying the charge e_s.

A microscopic theory explaining the superconductive state has been formulated not until the year 1957 by Bardeen, Cooper and Schrieffer. According to their theory, conduction electrons of opposite spin and momentum form bound pairs under the influence of a lattice phonon-induced attraction. The resulting particle, a so-called Cooper pair, has a spin of zero and hence obeys the Bose-Einstein statistics. This implies that, at low temperatures, all Cooper pairs condense into a ground state of lowest energy, while

single electron states, which are called *quasiparticles*, are energetically separated by a gap Δ that is related to the binding energy of the Cooper pair. Since the charge and mass of a Cooper pair is twice the electron mass, and their density n_s corresponds to half the electron density, Eq. (2.3) still holds even though F. and H. London assumed the charge carriers to be single electrons.

The range of the coherent pair correlation (the BCS coherence length) exceeds by far the mean spacing between two electrons. Therefore, the wave functions describing individual Cooper pairs overlap strongly, allowing to describe the condensate by a single, complex wavefunction Ψ, which is also called the superconducting order parameter. It has been introduced already in the year 1950 by Ginzberg and Landau and is formulated as

$$\Psi \;=\; \Psi_0(\vec{x},t)\;\exp\{i\phi(\vec{x},t)\}, \tag{2.4}$$

where $\phi(\vec{x},t)$ is its phase and the amplitude

$$|\Psi_0(\vec{x},t)|^2 = n_s \tag{2.5}$$

is given by the Cooper pair density. Superconductivity was thus recognized as a macroscopic quantum effect underlying the coherent motion of all the electrons pairs in the metal.

2.2 The current-biased Josephson junction

While the amplitude $|\Psi_0^2(\vec{x},t)|$ of the order parameter is constant inside a bulk superconductor, beyond its edges it declines exponentially. This long-range coherence gives rise to a coupling of the order parameters in two superconductors which are seperated by a thin dielectric barrier, as illustrated in Fig. 2.1.

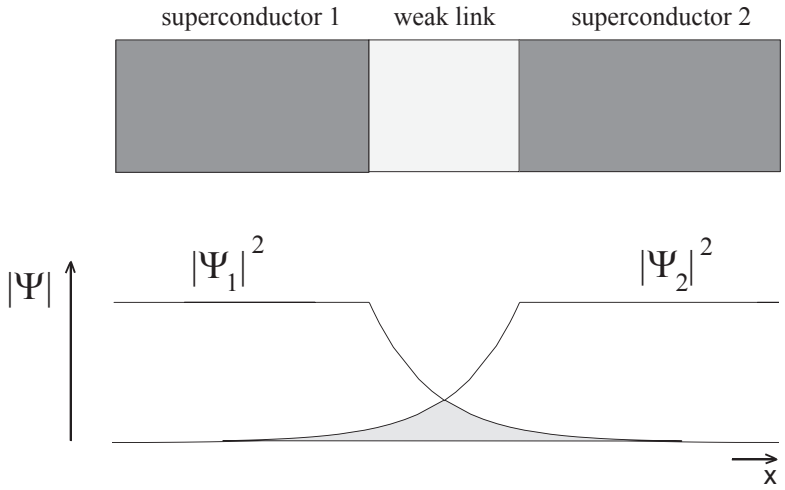

Figure 2.1: Top: A superconductor-insulator-superconductor system forming a Josephson junction. Bottom: At the boundary of a superconductor, the amplitude of the order parameter decays exponentially. This allows an overlap (shaded grey) of the two wavefunctions and provides a coupling between them.

2.2.1 Josephson equations

The theory describing a superconductor-insulator-superconductor system has been formulated by B. D. Josephson [37] in the year 1962. He predicted that a supercurrent would tunnel through the insulating barrier even in the absence of voltage. Its magnitude depends only on the phase difference $\varphi = \phi_1 - \phi_2$ between the order parameters of the two junction electrodes, also called the *Josephson phase*, and obeys the first Josephson equation

$$I \;=\; I_c \;\sin(\varphi), \tag{2.6}$$

where I_c is the maximum (called *critical*) current which can flow without dissipation. I_c depends on the energy gap Δ of the superconductor, the normal resistance of the tunnel barrier and the Cooper pair density. As long as the amplitude of a constant current I_b flowing through the barrier does not exceed the critical current I_c , there is no voltage drop across the junction, and the Josephson phase according to Eq. (2.6) will be constant,

$$\varphi = \arcsin \frac{I_b}{I_c} + 2\pi \mathrm{n}. \tag{2.7}$$

The second Josephson equation relates the time evolution of the phase difference φ to the voltage V across the junction:

$$\frac{\mathrm{d}\varphi}{\mathrm{dt}} \;=\; \frac{2\pi}{\Phi_0}\, V \;=\; \frac{2e}{\hbar}\, V, \tag{2.8}$$

where $\Phi_0 = h/2e = 2.07\ 10^{-15}\ Vs$ is the magnetic flux quantum, e is the electron charge and h is Planck's constant. Combining both equations implies that a constant voltage applied to the junction results in an alternating current

$$I = I_c\ \sin\left(\varphi_0\ + \frac{2\pi}{\Phi_0}\, Vt\right), \tag{2.9}$$

where the frequency-to-voltage ratio is given by

$$\frac{1}{\Phi_0} = 483.6\ \frac{\mathrm{MHz}}{\mu V}. \tag{2.10}$$

Vice versa, any change in the supercurrent and hence the Josephson phase will result in a nonzero voltage. The junction thus acts like an ideal but nonlinear inductance. By differentiating Eq. (2.6) and inserting Eq. (2.8), the Josephson inductance L can be obtained:

$$L = V\ \left(\frac{dI}{dt}\right)^{-1} = \frac{\hbar}{2e}\frac{1}{I_c\ \cos\varphi}. \tag{2.11}$$

One should note that this inductance depends through the Josephson phase φ on the bias current through the junction and will also take negative values.

2.2.2 The RCSJ model

The dynamics of the Josephson phase can be understood in the frame of the resistively and capacitively shunted junction model (RSCJ model) introduced by Stewart [38] and McCumber [39]. The model applies to small junctions, whose dimensions are smaller

than the characteristic length λ_J of spatial variations of the Josephson phase, typically 5 to 30 μm. This length is calculated as [40]

$$\lambda_J = \sqrt{\frac{\Phi_0}{2\pi j_c(2\lambda_L + t)}}, \tag{2.12}$$

where j_c is the critical current density in A/cm^2, λ_L the London penetration depth of the electrode material, t is the thickness of the insulating barrier and the electrodes are assumed to have a thickness larger than λ_L.

The junction is modeled by an equivalent circuit consisting of an ohmic resistor R, which represents its effective shunt resistance, a capacitor C accounting for the total capacitance of the junction electrodes and an element which behaves according to Eq. (2.6), see inset to Fig. 2.2.

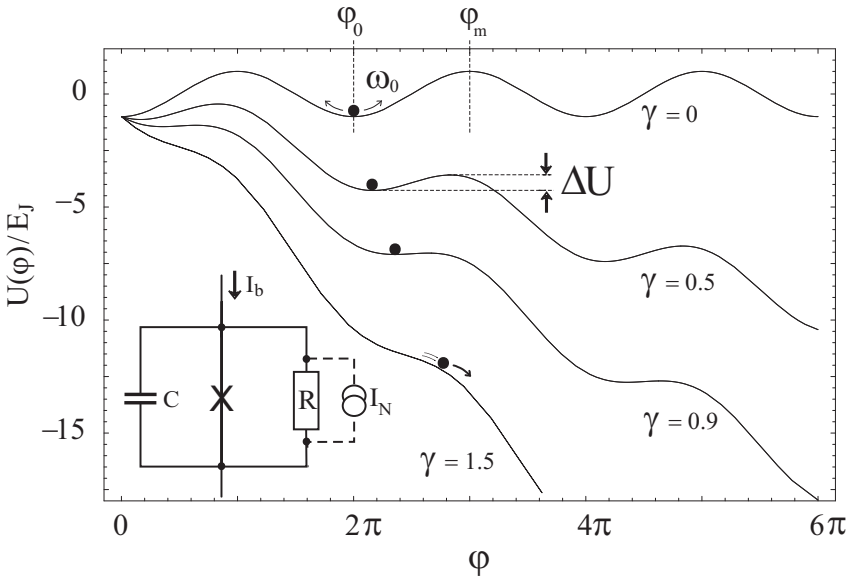

Figure 2.2: The washboard potential plotted for four different normalized bias currents γ. The virtual particle is indicated by a solid disc. For $\gamma = 0.5$, the potential barrier height ΔU is also shown. Inset: Equivalent circuit model of a Josephson junction. The Josephson supercurrent is symbolized by an X and the intrinsic capacitance and resistance are indicated as C and R, respectively. The fluctuation current source is connected by dashed lines to the resistor.

According to Kirchhoff's law, the total current flowing through such a system is the sum of the currents in each of the three paths. Using Eq. (2.9), this yields

$$I = I_c \sin\varphi + \frac{V}{R} + C\frac{dV}{dt} = I_c \sin\varphi + \frac{1}{R}\frac{\Phi_0}{2\pi}\dot{\varphi} + C\frac{\Phi_0}{2\pi}\ddot{\varphi}. \tag{2.13}$$

The right hand side of this equation can be written as an equation of motion,

$$m\ddot{\varphi} + m\frac{1}{RC}\dot{\varphi} + \frac{\partial U(\varphi)}{\partial\varphi} = 0, \tag{2.14}$$

for a virtual particle of mass

$$m = C\left(\frac{\Phi_0}{2\pi}\right)^2 \tag{2.15}$$

moving along its generalized coordinate φ in a potential $U(\varphi)$. The factor $(1/RC)$ represents the damping of the particle which is proportional to its velocity $\dot{\varphi}$, while $U(\varphi)$ is given by

$$U(\varphi) = \frac{I_c\Phi_0}{2\pi}\left(-\frac{I}{I_c}\,\varphi - \cos\varphi\right) = E_J\,(-\gamma\,\varphi - \cos\varphi), \tag{2.16}$$

where the Josephson energy $E_J = I_c\Phi_0/2\pi$ has been introduced. The potential has the form of a cosine which is tilted proportional to the normalized bias current γ, and is therefore called a *washboard potential*. See figure 2.2 for a plot of $U(\varphi)$ at several values of the normalized bias current γ.

The potential barrier height U_0 of a metastable well can be calculated from the potential difference $U(\varphi_m) - U(\varphi_0)$ between the local maximum at $\varphi_m = \pi - \arcsin(\gamma)$ and the minimum of the well located at $\varphi_0 = \arcsin(\gamma)$,

$$\begin{aligned} U_0 &= 2E_J\left[\sqrt{1-\gamma^2} - \gamma\,\arccos(\gamma)\right] \\ &\cong E_J\frac{4\sqrt{2}}{3}(1-\gamma)^{3/2} \;\text{ for }\; \gamma \;\to 1. \end{aligned} \tag{2.17}$$

2.2.3 Classical phase dynamics

The Josephson potential allows for two modes of motion of the virtual particle. If it remains trapped in one potential well, it may undergo small oscillations around the potential minimum. This motion corresponds to the *zero-voltage state* of the junction, because the time average of the Josephson phase will be constant, and hence the average DC voltage will be zero according to Eq. (2.8). The small oscillation frequency ω_0 can either be obtained from the curvature of the potential

$$U''(\varphi) \;=\; \frac{d^2U(\varphi)}{d\varphi^2}, \tag{2.18}$$

and the the effective mass m by calculating

$$\omega_0 \;=\; \sqrt{U''(\varphi)/m}, \tag{2.19}$$

or using the junction capacitance and the definition of the Josephson inductance,

$$\omega_0 = \frac{1}{\sqrt{L\,C}} = \omega_p\;(\cos\varphi)^{1/2} \;= \omega_p\;\left(1-\gamma^{\,2}\right)^{1/4}, \tag{2.20}$$

where the *plasma frequency* ω_p has been introduced:

$$\omega_p = \left(\frac{2e\,I_c}{\hbar\,C}\right)^{1/2}. \tag{2.21}$$

Since both the critical current I_c and junction capacitance C scale with area, the plasma frequency is determined by the fabrication process and can only be reduced by an

additional shunt capacitance to the junction. For typical tunnel junctions, $\nu_p = \omega_p/2\pi$ is in the microwave range with several tens of GHz.

If the particle once escaped from a well and the damping is not too high, i.e. $(\omega_p RC)^{-1} \ll 1$, its kinetic energy will exceed the barrier height of the next well and the particle continues to run down the washboard. The junction is then in its *voltage state*: the phase increases steadily and a nonzero dc voltage appears according to the second Josephson equation (2.8). To retrap the particle in one well and hence to switch back to the zero-voltage state, it will be necessary to reduce the potential tilt substantially by reducing the applied bias current. This is the origin of the hysteresis observed on the current-voltage characteristics of a Josephson junction with low damping (see Fig. 2.3).

From the IV-curve, one can estimate the resistance of the barrier R_n when the junction is in its normal state for currents larger than the critical current. The so-called subgap-resistance $R_{\rm sg}$ is given by the slope of the voltage dependence for currents just above the retrapping current. The quasi-particle resistance at temperature T is then given by

$$R_{\rm qp} = R_n \, \exp\left(\frac{\Delta}{k_B T}\right), \tag{2.22}$$

where $k_B = 1.38 \cdot 10^{-23} J/K$ denotes Boltzmann's constant and the energy gap Δ is found from the measured gap voltage via $\Delta = V_g \, e/2$. This equation shows that $R_{\rm qp}$ should become extremely high at low temperatures, since the quasiparticle density exponentially decreases with temperature as stated within the BCS theory.

Beneath a damping, the resistance provides another important contribution to the phase dynamics since every resistive element constitutes a source of current fluctuations at finite temperatures. This is indicated in Fig. 2.2 (a) as the additional current source I_N which is connected with dashed lines to the resistor. The temporal average of the noise current $I_N(t)$ at temperature T is given by the Johnson-Nyquist noise formula and satisfies [41]

$$\int_{-\infty}^{\infty} < I_N(t) I_N(0) >_T \, e^{i\omega t} dt = 2 k_B T / R. \tag{2.23}$$

These fluctuations in the bias current result in variations of the position of the classical particle, which describes the state of the junction. This gives rise to a temperature-induced escape from the metastable well as discussed in chapter 2.2.5.

Quality Factor

A measure for the damping of the plasma oscillation by the effective shunt resistance R of the junction is the dimensionless *quality factor* (Q factor). It relates the energy W stored in the oscillating system to the energy $W_{\rm diss}$ dissipated during one cycle via $Q = \omega_0 W / W_{\rm diss}$. Thus, the Q factor estimates the number of periods during which the oscillation energy will be dissipated. When considering pure Ohmic damping, the quality factor of a Josephson junction is defined as

$$Q = RC \, \omega_0. \tag{2.24}$$

High frequency contributions to dissipation

Although the RSCJ model predicts many properties of the Josephson junction correctly and straightforward, one should be aware of the fact that the model is simplified

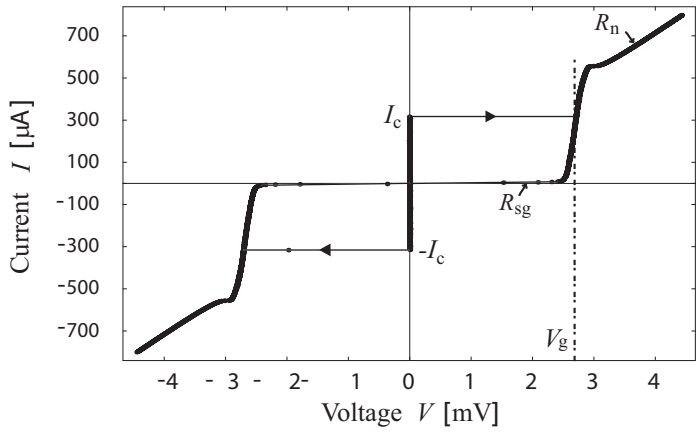

Figure 2.3: Current-voltage characteristic of a typical Josephson junction fabricated from a Nb/Al/AlO$_x$/Nb trilayer, measured at 20 mK temperature. Indicated by I_c is the critical current and V_g denotes the gap voltage. The slope of the curve at higher voltages displays the normal resistance $R_n \backsimeq 5.2\,\Omega$ of the barrier. Also indicated is the subgap-resistance $R_{\rm sg} \approx 400\,\Omega$.

by assuming a frequency-independent shunt resistance which furthermore neglects any contributions to the junction impedance at high frequencies arising from the bias circuitry.

2.2.4 Macroscopic quantum effects

At low temperatures and weak damping, the particle analog is no more suitable for an appropriate description of the phase dynamics because quantum effects become apparent. Experimentally, macroscopic quantum tunneling [2] and indications for energy level quantization [42, 4] were found already 20 years ago.
However, there should be a smooth transition between quantum and classical limits of the macroscopic system, and experimental results can often be interpreted in both pictures [43]. One example described in the following is the resonantly driven oscillator. This involves adding a small microwave (μW) current component $I_{\mu\rm W}$ of the form

$$I_{\mu\rm W} = I_{\rm m} \sin(\omega_{\mu W}\, t + \phi_{\mu W}) \tag{2.25}$$

to the bias current. Its frequency and amplitude are denoted as $\omega_{\mu\rm W}$ and $I_{\rm m}$, $\phi_{\mu W}$ is its phase.

In the classical picture, the effects arising from the microwave current can be understood as due to a periodic force driving the particle [44]. A maximum of energy is transferred to the particle when the frequency $\omega_{\mu\rm W}$ of the microwave is close to the natural frequency of the oscillation in the well ω_0.

For the same situation but in terms of the quantum picture, the photon energy $\hbar\omega_{\mu\rm W}$ must be equal to the energy separation of the ground state and the first excited state to allow transitions between levels by the absorption or emission of one photon (see figure 2.4).

The discrete energy levels in the quadratic potential well of a quantum mechanical harmonic oscillator are located at $(n+1/2)\,\hbar\omega_0$, with $n \geq 0$. The potential wells of the

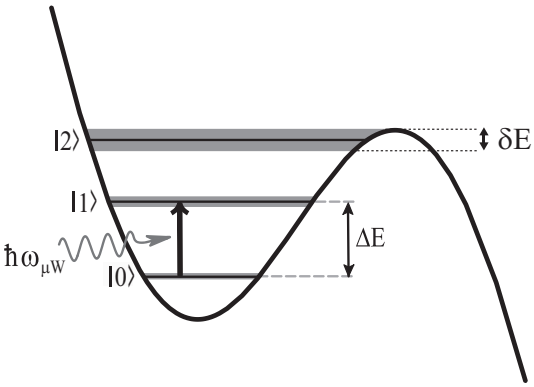

Figure 2.4: Illustration of resonant activation. The phase is activated from the ground state to the first excited state by absorbing a photon, if the photon energy $\hbar\omega_{\mathrm{RF}}$ is equal to the energy difference ΔE.

biased Josephson junction in contrast are tilted sinusoids, and so the spacing between adjacent levels decreases with increasing energy. Only due to the anharmonicity of the potential well it becomes possible to address the excited states individually, since an applied microwave will be resonant only to a certain transition.

The fact that the classical anharmonic oscillator also responds to frequencies satisfying

$$\omega_{\mathrm{rf}} = \frac{p}{q}\,\omega_0 \tag{2.26}$$

with p and q being integers [45] can be interpreted quantum mechanically as a transition involving more than one photon at once, thus called *multi-photon* transition, which has been observed experimentally [46]. For the case of a transition over a level spacing ΔE involving a number of q photons, the individual photon energies E_{ph} must comply $\Delta E = qE_{\mathrm{ph}}$, corresponding to an microwave frequency of $\omega_0/(2\pi\, q)$.

Whether a Josephson junction is described more exactly by a quantum system having a small number of discrete states rather than as a classical anharmonic oscillator is decided by the effective particle mass $m \propto C$ and the strength of dissipation. Both the effective damping resistance R as well as a the capacitance C give rise to a broadening of the energy levels by an amount δE [5] following

$$\delta E \propto \frac{1}{RC}. \tag{2.27}$$

In the quantum limit at low damping, the energy levels are narrow enough to remain clearly separated. Increasing the damping, for instance by raising the temperature according to Eq. (2.22), will eventually result in broad overlapping energy levels which are seen as a continuum. In practice, the discreteness of the energy levels may be shadowed already at much lower temperatures due to the additional energy uncertainty given by temperature fluctuations.

2.2.5 Escape mechanisms

An ideal classical particle at zero temperature is expected to escape from a metastable well only when the barrier height vanishes. In the junction model, this corresponds to a bias current equal to the critical current. In reality, thermal fluctuations and quantum tunnelling allow the phase to escape from the well already at smaller bias currents. The

probability of escape may be expressed in terms of the lifetime τ of the zero-voltage state, which is the inverse of the escape rate Γ

$$\tau \equiv \Gamma^{-1}. \tag{2.28}$$

In the following, the two escape processes are discussed and formulas for the escape rate from the zero-voltage state are given for particular regimes.

Thermal activation

In the classical analog, the virtual particle can be regarded as being subject to Brownian motion. The formula which describes the temperature dependence of the rate at which the particle can overcome the potential barrier of height U_0 was found by Arrhenius. It is given by the exponential negative ratio of the potential barrier height U_0 (Eq. 2.17) to the thermal energy as the product of Boltzmann's constant k_B and temperature T. The rate of escape $\Gamma_{\rm th}$ due to thermal activation hence follows the equation

$$\Gamma_{\rm th} = a_t \frac{\omega_0}{2\pi} \exp\left(-\frac{U_0}{k_B T}\right), \tag{2.29}$$

where the pre-exponential factor $\frac{\omega_0}{2\pi}$ resembles the attempt frequency towards the barrier. Figure 2.5 illustrates the process of thermal activation.

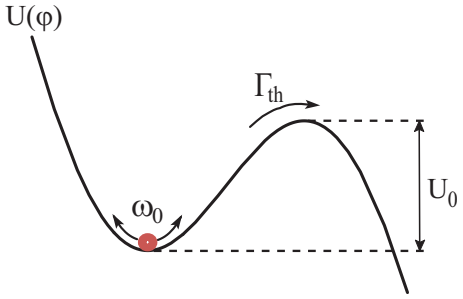

Figure 2.5: A zoom into one metastable well where the analogous classical particle oscillates at frequency ω_0 around the potential minimum. The brownian particle is pushed across the barrier height U_0 by thermal fluctuations in its energy at the thermal escape rate $\Gamma_{\rm th}$.

Friction reduces the thermal excape rate nonexponentially as discussed in Kramer's seminal paper [47] for the case of frequency independent (ohmic) damping. In the moderate to large damping regime, the escape is reduced due to back-diffusion over the barrier top, while for very weak friction the highly excited states are depleted because of weaker influence of the heat bath to the system, which prevents it from being in thermal equilibrium. See [48] for a detailed review. These effects are taken into account in the damping prefactor a_t, which can be approximated in the limit of low damping as [49]

$$a_t = \frac{4a}{[(1+\frac{Q\,k_B T}{1.8 U_0})^{1/2}+1]^2} \lesssim 1, \tag{2.30}$$

where a is a numerical constant close to unity.

Macroscopic quantum tunnelling

As the temperature approaches zero, the thermal escape rate is exponentially suppressed and the metastable state can only decay via macroscopic quantum tunnelling.

The term *macroscopic* emphasizes the fact that this tunnelling concerns the Josephson phase as a whole rather than single Cooper pairs.

The quantum tunnel rate $\Gamma_{\rm qu}$ may be calculated using the semi-classical Wentzel-

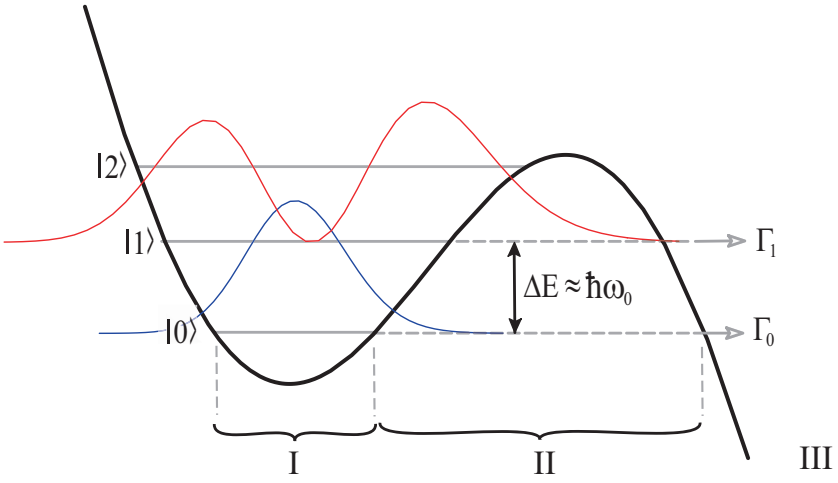

Figure 2.6: Quantum picture of the state of the Josephson phase inside the well, wherein the discrete energy levels are indicated as grey horizontal lines. Tunnelling from the excited state occurs at a rate Γ_1, which is about 1000 times larger than the tunnel rate from the ground state Γ_0 since the corresponding barrier height is reduced by the energy difference ΔE. Additionally shown is a sketch of the squared wavefunctions $|\Psi|^2$ of the ground state $|0\rangle$ and the first excited state $|1\rangle$.

Kramers-Brillouin (WKB) approximation. In region I, the ground state wavefunction Ψ_I coincides with that of an anharmonic oscillator, whereas it declines exponentially in the classical forbidden region II, where $E_0 < U_0(\varphi)$. The escape rate is then found [50] by relating the remaining probability $|\Psi_{\rm III}|^2$ in region III to $|\Psi_{\rm I}|^2$, resulting in

$$\Gamma_{\rm qu} = \frac{\omega_0}{2\pi}\left(\frac{864\pi\, U_0}{\hbar\omega_0}\right)^{1/2} \exp\left(-\frac{36}{5}\frac{U_0}{\hbar\omega_0}\right). \tag{2.31}$$

The effect of damping on quantum tunnelling was investigated in the work of Caldeira and Leggett [51, 52] by modelling the friction as a coupling to an infinite set of harmonic oscillators. The tunnel rate is then expressed as

$$\Gamma_{\rm qu} = A\ \exp(-B) \tag{2.32}$$

with

$$\begin{aligned} A &= \sqrt{60}\,\omega_0\left(\frac{B}{2\pi}\right)^{1/2}(1+\mathcal{O}(Q^{-1})),\\ B &= \frac{36}{5}\frac{U_0}{\hbar\omega_0}(1+\frac{1.74}{Q}+O(Q^{-2})), \end{aligned} \tag{2.33}$$

where the WKB-result is recovered for $Q \gg 1$. Note that damping affects the quantum tunnel rate exponentially, in contrast to the thermal activation rate.

Tunnelling from excited states happens at an exponentially higher rate, since the

corresponding barrier height is reduced by the energy of the excited level. For typical bias currents where tunnelling becomes observable ($\gamma \gtrsim 0.99$), the escape rate from the first excited state is three orders of magnitude higher than the one from the ground state. This allows to deduce the quantum state of the phase before it tunnelled by measurements of the lifetime of the zero-voltage state.

Cross-over regime

The transition from the dominance of thermal activation to macroscopic tunnelling happens around the cross-over temperature T^*, for which an estimation is [48]

$$T^* \simeq \frac{\hbar\omega_0}{2\pi k_B}\left[\left(1+\frac{1}{2Q}^2\right)^{1/2}-\frac{1}{2Q}\right]. \tag{2.34}$$

The Q-dependent damping factor in this equation decreases the cross-over temperature by less than 1% for junctions with $Q \geqslant 50$.

Quantum corrections have to be applied to the thermal activation rate already above the cross-over temperature, since the tunnelling from thermally excited states is exponentially increased due to the smallness of the remaining barrier. Indications for the existence of quantized energy levels above the crossover temperature were found experimentally by Silvestrini et. al. [53]. At finite temperature and in thermal equilibrium, the occupation probability ρ_n for the $n-$th level is given by the Boltzmann distribution [54]

$$\rho_n = \Xi^{-1}\exp\left(-E_n/k_BT\right), \quad \Xi = \sum_{n=0}^{\infty}\exp\left(-E_n/k_BT\right). \tag{2.35}$$

The total escape rate is then the sum of the rates from each individual level multiplied by its occupation probability. A useful approximation to the escape rate in the intermediate temperature regime $1.4\,T^* \lesssim T \lesssim 3\,T^*$ is [55]

$$\Gamma_{T^*} = a_i\frac{\omega_0}{2\pi}\exp\left(-\frac{U_0}{k_BT}\right) \tag{2.36}$$

where the prefactor a_i valid to first order in 1/Q is

$$a_i = \frac{\sinh(\hbar\omega_0/2k_BT)}{\sin(\hbar\omega_0/2k_BT)}. \tag{2.37}$$

Equation (2.36) assumes the population in the excited levels to strictly obey the Boltzmann distribution. At higher temperatures, the escape rate is therefore correctly given only by Eq. (2.29), where the depletion of excited states through tunnelling is considered in the thermal prefactor a_t.

2.3 Coherent dynamics in the two-state system

The theoretical treatment of two-level quantum systems is of fundamental importance for the description of a great variety of quantum effects. A well-studied example is the spin-1/2 particle in an external magnetic field which constitutes an analogon to any two-state system, and hence quantum bits also fall into this categorie. The same mathematical apparatus can be used to describe a current-biased Josephson junction if

its energy spectrum can be truncated to the lowest to levels. In this case, an external perturbation is realized by an applied microwave current at close resonance, i.e. its frequency ω_{rf} is practically equal to the small oscillation frequency ω_{10} given by Equation (2.20).

The effect of such a perturbation or coupling is two-fold. Statically, it results in a change of the position of the energy levels. Dynamically, coherent oscillations between the two states appear, which are of particular experimental interest for the creation of state superpositions.

2.3.1 Rabi oscillation

Rabi oscillations are coherent oscillations between the eigenstates of a two-level quantum system which is subject to a resonant perturbation. The calculation of the Rabi frequency and amplitude poses a standard problem which is discussed in many books on quantum mechanics. Here, I follow the notation of [56]. The result is then be applied to the current-biased Josephson junction.

A two-level system without any perturbation is described by its Hamiltonian $\mathcal{H}_0$. By using its eigenstates $|\varphi_0\rangle$ and $|\varphi_1\rangle$ as a basis, the stationary Schrödinger equation reads

$$\begin{aligned} \mathcal{H}_0 |\varphi_0\rangle &= E_0 |\varphi_0\rangle \\ \mathcal{H}_0 |\varphi_1\rangle &= E_1 |\varphi_1\rangle , \end{aligned} \tag{2.38}$$

where E_0 and E_1 are the corresponding eigenenergies and the Hamiltonian has the diagonal form

$$\mathcal{H}_0 = \begin{pmatrix} E_0 & 0 \\ 0 & E_1 \end{pmatrix}. \tag{2.39}$$

When the perturbation is switched on, the new Hamiltonian becomes

$$\mathcal{H} = \mathcal{H}_0 + \mathcal{W}, \tag{2.40}$$

where $\mathcal{W}$ denotes the perturbation or coupling operator. As a result, we expect both new eigenstates, denoted $|\Psi_+\rangle$ and $|\Psi_-\rangle$, and new eigenenergies E_+ and E_-. Equation (2.38) then becomes

$$\begin{aligned} \mathcal{H} |\Psi_+\rangle &= E_+ |\Psi_+\rangle \\ \mathcal{H} |\Psi_-\rangle &= E_- |\Psi_-\rangle . \end{aligned} \tag{2.41}$$

The coupling is represented by the hermitian matrix

$$\mathcal{W} = \begin{pmatrix} W_{00} & W_{01} \\ W_{10} & W_{11} \end{pmatrix} \tag{2.42}$$

with W_{00} as well as W_{11} being real and $W_{01} = W_{10}^*$. We can assume that both W_{00} and W_{11} are equal to zero since their effect can be implicitly taken into account by replacing E_0 and E_1 in equation (2.39) by $E_0' = E_0 + W_{00}$ and $E_1' = E_1 + W_{11}$, respectively. For the diagonalization of the new hamiltonian (2.40) we shall follow the procedure given in [56], which yields the two eigenvalues

$$E_\pm = \frac{1}{2}(E_0 + E_1) \pm \frac{1}{2}\sqrt{(E_0 - E_1)^2 + 4|W_{01}|^2} \tag{2.43}$$

and the two eigenvectors

$$\begin{aligned} |\Psi_+\rangle &= \cos\left(\frac{\theta}{2}\right) e^{-i\varphi/2}\,|\varphi_0\rangle + \sin\left(\frac{\theta}{2}\right) e^{i\varphi/2}\,|\varphi_1\rangle \\ |\Psi_-\rangle &= -\sin\left(\frac{\theta}{2}\right) e^{-i\varphi/2}\,|\varphi_0\rangle + \cos\left(\frac{\theta}{2}\right) e^{i\varphi/2}\,|\varphi_1\rangle\,. \end{aligned} \tag{2.44}$$

The angels θ and φ refer to those used in the Bloch-sphere description of section 2.3.3, and are defined as

$$\begin{aligned} \tan\theta &= \frac{2|W_{01}|}{E_0 - E_1}, \quad 0 \le \theta < \pi, \\ W_{10} &= e^{i\varphi}\,|W_{10}|. \end{aligned} \tag{2.45}$$

Since the time evolution of the quantum state follows the Schrödinger equation

$$i\hbar\,\frac{\mathrm{d}}{\mathrm{d}t}\;|\Psi(t)\rangle = \mathcal{H}\;|\Psi(t)\rangle\,, \tag{2.46}$$

we can write

$$|\Psi(t)\rangle = \alpha\, e^{-i\,E_+ t/\hbar}\,|\Psi_+\rangle + \beta\, e^{-i\,E_- t/\hbar}\,|\Psi_-\rangle\,. \tag{2.47}$$

α and β are determined by the initial condition, for which we define the system to be in the ground state $|\Psi(0)\rangle = |\varphi_0\rangle$ at time $t = 0$. We can now rewrite Eq. (2.47) by solving Eq. (2.44) for $|\varphi_0\rangle$,

$$|\Psi(0)\rangle = |\varphi_0\rangle = e^{i\varphi/2}\,[\cos\left(\frac{\theta}{2}\right)|\Psi_+\rangle - \sin\left(\frac{\theta}{2}\right)|\Psi_-\rangle] \tag{2.48}$$

and we obtain

$$|\Psi(t)\rangle = e^{i\varphi/2}\,[\,e^{-i\,E_+ t/\hbar}\;\cos\left(\frac{\theta}{2}\right)\;|\Psi_+\rangle - \;e^{-i\,E_- t/\hbar}\sin\left(\frac{\theta}{2}\right)\;|\Psi_-\rangle]. \tag{2.49}$$

To show that the state (2.49) indeed oscillates between the unperturbed states $|\varphi_0\rangle$ and $|\varphi_1\rangle$, we first write

$$\langle\varphi_1|\Psi(t)\rangle = e^{i\varphi/2}\;\sin\left(\frac{\theta}{2}\right)\cos\left(\frac{\theta}{2}\right)[\,e^{-i\,E_+ t/\hbar}\; - e^{-i\,E_- t/\hbar}] \tag{2.50}$$

and use this to calculate the probability $\mathcal{P}_1(t) = |\langle\varphi_1|\Psi(t)\rangle|^2$ to find the system in state $|\varphi_1\rangle$ at time t: [1]

$$\begin{aligned} \mathcal{P}_1(t) &= \frac{1}{2}\sin^2\theta\;\left[1 - \cos\left(\frac{E_+ - E_-}{\hbar}\;t\right)\right] \\ &= \sin^2\theta\;\sin^2\left(\frac{E_+ - E_-}{2\hbar}\;t\right), \end{aligned} \tag{2.51}$$

which after substitution of (2.43) and (2.45) reads

$$\mathcal{P}_1(t) = \frac{4|W_{01}|^2}{4|W_{01}|^2 + (E_0 - E_1)^2}\sin^2\left[\sqrt{4|W_{01}|^2 + (E_0 - E_1)^2}\;\;\frac{t}{2\hbar}\right] \tag{2.52}$$

[1] By making use of the identity $\sin^2(\theta/2)\cos^2(\theta/2) = \frac{1}{4}\sin^2(\theta)$ and Euler's formula we find $|\,e^{-i\,E_+ t/\hbar}\; - e^{-i\,E_- t/\hbar}\,|^2 = 2[1 - \cos(\frac{E_+ - E_-}{\hbar}\;t)]$.

Known as Rabi's formula, equation (2.52) describes a sinusoidal oscillation of $\mathcal{P}_1$ at the so-called Rabi-frequency

$$\omega_R = \sqrt{4|W_{01}|^2 + (E_0 - E_1)^2}\,\frac{1}{2\hbar} \tag{2.53}$$

and with an amplitude which is close to one if the coupling is strong, or $|W_{01}| \gg |E_0 - E_1|$.

Decoherence effects

As it was mentioned before, the discrete phase eigenstates of a Josephson junction are not stable. For example, the ground state can decay by tunnelling at the rate Γ_0 towards the continuum, and the excited state can additionally fall back to the ground state due to dissipation at the rate Γ_d. Furthermore, the coherence of the superposition state is affected by dephasing at the rate Γ_ϕ.

To show how this influences the time-dependent level population as calculated in equation (2.52), we can define the total off-diagonal decay rate Γ as the sum of individual decoherence rates [57], i.e. $\Gamma = \Gamma_0 + \Gamma_1 + \Gamma_d + 2\Gamma_\phi$. Quantum mechanics allows to phenomenologically take into account the finite lifetime of a state by adding an imaginary term to its energy, which is then given by[2]

$$E_n' = E_n - i\,\hbar\,\frac{\Gamma}{2}. \tag{2.54}$$

Following the calculation in section 2.3.1, we note that the time-evolution operator will be replaced by

$$e^{-i\,E_n' t/\hbar} = e^{-i\,E_n\,t/\hbar} \cdot e^{-\frac{\Gamma}{2}\,t/\hbar}. \tag{2.55}$$

For the time-dependent population of the excited level we obtain

$$\mathcal{P}_1(t) = \frac{|W_{01}|^2}{|W_{01}|^2 - \left(\frac{\hbar}{2}\Gamma\right)^2}\, e^{-\Gamma t}\, \sin^2\left[\sqrt{|W_{01}|^2 - \left(\frac{\hbar}{2}\,\Gamma\right)^2}\;\;\frac{t}{2\hbar}\right]. \tag{2.56}$$

Equation (2.56) is valid for $|W_{01}| > \frac{\hbar}{2}\Gamma$. This means that the excited level population will undergo damped sinusoidal oscillations if the coupling is strong enough to sufficiently increase the Rabi frequency so that the system can oscillate before it becomes incoherent, see Fig. 2.7.

Detuning

The externally applied microwave frequency might not be tuned exactly to the transition frequency and differ by a value of

$$\Delta = \frac{|E_1 - E_0|}{\hbar} - \omega_{\mathrm{rf}}. \tag{2.57}$$

Any detuning Δ results in a higher oscillation frequency and decreases the amplitude. The oscillating population probability of the excited level corrected for detuning is

$$\mathcal{P}_1(t) = \frac{|W_{01}|^2}{|W_{01}|^2 + \Delta^2}\, \sin^2\left[\sqrt{|W_{01}|^2 + \Delta^2}\;\;\frac{t}{2\hbar}\right]. \tag{2.58}$$

Figure 2.8 shows that for larger detuning the amplitude decreases, while the Rabi frequency increases.

[2] see [56], complement $\mathrm{H_{IV}}$.

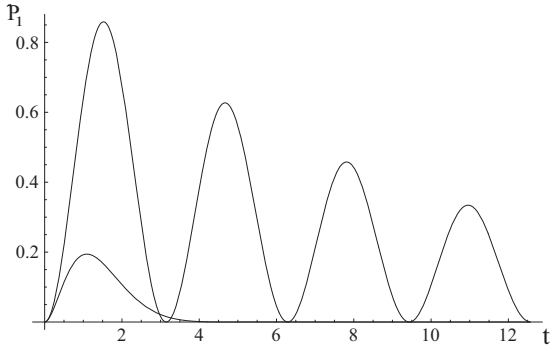

Figure 2.7: A plot of equation (2.56) for a low decoherence rate $\left(\frac{\hbar}{2}\Gamma\right) = 0.1|W_{01}|$ shows exponentially decaying oscillations. For a large decoherence rate, $\left(\frac{\hbar}{2}\Gamma\right) = 1.5|W_{01}|$, oscillations do not occur.

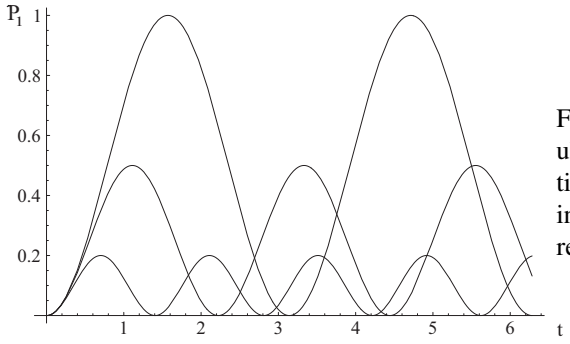

Figure 2.8: The excited level population $\mathcal{P}_1(t)$ as given by equation (2.58), plotted for the detunings $\Delta = 0$, $2|W_{01}|$ and $4|W_{01}|$, respectively.

Mapping to the case of the Josephson junction

For the microwave-irradiated Josephson junction, we can write its bias current as $I(t) = I + I_{dc}(t) + \Delta I_{\rm rf}(t)$, which is the sum of the constant I, a component $I_{dc}(t)$ varying slowly compared to the small oscillation frequency and the microwave component $\Delta I_{\rm rf}(t) = I_{\rm rf}[\cos(\omega_{\rm rf}\, t) + i\, \sin(\omega_{\rm rf}\, t)]$. $I_{\rm rf}$ is the absolute amplitude of the alternating current. Slow variations of $I_{\rm dc}$ will result in a change of the energy scale of the system and hence affect only the diagonal components of the Hamiltonian. Its non-diagonal (coupling) matrix element can be reduced to be proportional just to the microwave amplitude by applying the rotating wave approximation and is then given by [58]

$$W_{01} = \langle 0|\, \phi\, |1\rangle\, \frac{\Phi_0}{2\pi} I_{\rm rf}. \tag{2.59}$$

If we assume that the potential is sufficiently harmonic for $U(\phi) \lesssim E_1$, the overlap matrix element of the harmonic oscillator can be used, which is

$$\langle 0|\, \varphi\, |1\rangle = \sqrt{\frac{\hbar}{2\, m\, \omega_0}} = \frac{2\pi}{\Phi_0}\, \sqrt{\frac{\hbar}{2\, \omega_0\, C}}\,, \tag{2.60}$$

where the effective mass of the virtual particle (2.15) has been inserted for m. We find the Rabi frequency from equation (2.53), which reduces to

$$\omega_R = \frac{|W_{01}|}{\hbar} \tag{2.61}$$

for the case of strong coupling and low damping ($|W_{01}| \gg |E_0 - E_1| \gg |\hbar\Gamma/2|$) and a resonant ($\omega_{\rm rf} = \omega_{01}$) stimulation. The strong coupling condition is preferred

in experiments in order to obtain both large frequency and amplitude of the coherent oscillation, which will then be less affected by detuning and decoherence. Finally, we obtain

$$\omega_R = \frac{I_{\rm rf}}{\hbar}\sqrt{\frac{\hbar}{2\omega_0 C}} = \eta\,|\langle 0|\,\varphi\,|1\rangle|\,\frac{E_J}{\hbar} \tag{2.62}$$

where we have defined $\eta = I_{\rm rf}/I_c$ as the microwave amplitude normalized to the critical current and we make use of the Josephson energy $E_J = I_c\Phi_0/(2\pi)$.

2.3.2 Energy-level repulsion

To discuss the modifications of the energy levels due to the coupling, we rewrite equation (2.43) for the energy eigenvalues:

$$\begin{aligned} E_+ &= E_m + \sqrt{{E_\Delta}^2 + |W_{01}|^2} \\ E_- &= E_m - \sqrt{{E_\Delta}^2 + |W_{01}|^2}, \end{aligned} \tag{2.63}$$

$$\begin{aligned} E_m &= \frac{1}{2}(E_0 + E_1) \\ E_\Delta &= \frac{1}{2}(E_0 - E_1) \end{aligned} \tag{2.64}$$

where E_0 and E_1 are still the energies of the unperturbed states. For conditions where these are equal ($E_\Delta = 0$), the most striking feature is that the coupling separates them by the amount of $2|W_{01}|$. Figure 2.9 shows a plot of the eigenenergies. The asymptotes to the eigenenergies for large E_Δ are the unperturbed energies E_0 and E_1. This anti-crossing of the energy levels has been observed in the tunable double-well potential of a SQUID [7, 59] and was the first experimental proof of coherence for the phase variable in a Josephson junction incorporated into a superconducting loop.

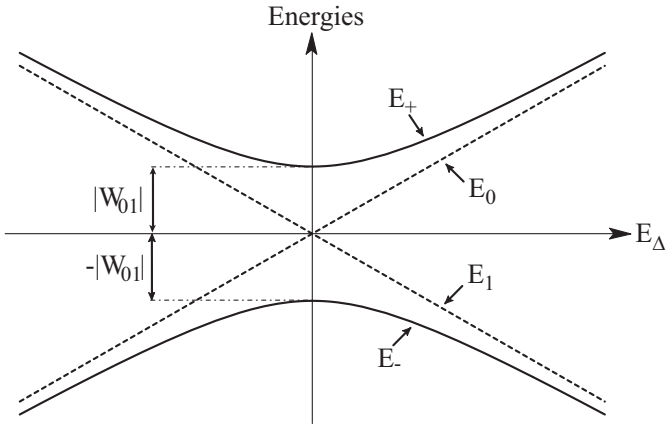

Figure 2.9: A plot of the eigenenergies of the states without coupling (E_0 and E_1) and with non-diagonal coupling (E_+ and E_-) versus their energy difference $E_\Delta = (E_0 - E_1)/2$.

In the case where the levels are separated but the coupling is weak ($E_\Delta \gg |W_{01}|$,

equation (2.63) can be approximated as

$$E_{\pm} = E_m \pm E_\Delta \left(1 + \frac{1}{2}\left|\frac{W_{01}}{E_\Delta}\right|^2 + \dots\right), \tag{2.65}$$

showing that the effect on the energies is of second order in the coupling strength. In contrast, for strong coupling or $E_\Delta \ll |W_{01}|$, we obtain

$$E_{\pm} = E_m \pm |W_{01}| \tag{2.66}$$

which results in a more significant change of the eigenenergies since it is an effect of first-order in $|W_{01}|$.

2.3.3 Bloch-sphere description of the qubit state

The state of the quantum bit can be represented by a vector $|\Psi\rangle$ contained in the Hilbert space which is spanned in the computational basis by the two logical states $|0\rangle$ and $|1\rangle$,

$$|\Psi\rangle = a\,|0\rangle + b\,|1\rangle\,, \tag{2.67}$$

where the square of the amplitudes $|a|^2$ and $|b|^2$ correspond to the probability to find the qubit in state $|0\rangle$ or $|1\rangle$, respectively. Accordingly, these probabilities must sum to one, leading to the normalization condition $\langle\Psi|\Psi\rangle = |a|^2 + |b|^2 = 1$. While in general a and b are complex numbers, it is only the absolute value of the coefficients which is observable by a measurement of the qubit state, and therefore only the phase difference between the coefficients remains to be considered. Together with the normalization condition, the four dimensional configuration space therefore reduces to a two dimensional subspace [60, 19].

It is instructive to illustrate the quantum state of a single qubit within the Bloch vector picture. If the qubit remains in a pure state, that is, $|a|^2 + |b|^2 = 1$, then the Bloch vector points to the surface of a unit sphere as shown in Fig. 2.10. The qubit state is determined by the polar and azimuthal angels ϕ and θ according to

$$|\Psi\rangle = \cos(\theta/2)\,|0\rangle + e^{i\,\phi}\sin(\theta/2)\,|1\rangle\,. \tag{2.68}$$

The squared projection of the state vector to the $\vec{z}$-axis, which is assumed to be the quantization axis, gives the occupation probability of the two logical states, which for the ground state reads $p_0 = \cos^2(\theta/2)$. The precession around the $\vec{z}$-axis at the Larmor frequency ω_{10} arising from the energy difference between the two states is taken into account conveniently by changing to the ω_{10}-rotating frame. This implies that the phase ϕ does not change as long as all external parameters remain constant.

Logical operations on qubits are also called quantum gates and correspond to transformations of the state vector which must be unitary (and hence reversible) to ensure that a pure state gets mapped to a pure state. In the Bloch picture, these single-qubit operations correspond to rotations around the three axis $\vec{x}, \vec{y}$ and $\vec{z}$. A unitary rotation operator $\hat{R}_{\vec{n}}(\alpha)$ defining a rotation around the unit vector $\vec{n}$ by an angle α can be written with the use of the set of Pauli spin operators $\sigma = \{\hat{\sigma}_x, \hat{\sigma}_y, \hat{\sigma}_z\}$ and reads

$$\hat{R}_{\vec{n}}(\alpha) = \exp\left(-i\,\frac{\alpha}{2}\,\vec{n}\cdot\sigma\right) \tag{2.69}$$

$$= \mathbb{I}\cos(\alpha/2) - i\,\sin(\alpha/2)\,\vec{n}\cdot\sigma, \tag{2.70}$$

where $\mathbb{I}$ denotes the unity operator. For example, the qubit is transferred from the ground state $|0\rangle$ to the superposition state $(|0\rangle + |1\rangle)/\sqrt{2}$ by rotating the Bloch vector around the $\vec{y}$-axis by an angle of $\pi/2$ with the matrix operator

$$\hat{R}_{\vec{y}}(\pi/2) = \begin{pmatrix} \cos(\pi/2) & -\sin(\pi/2) \\ \sin(\pi/2) & \cos(\pi/2) \end{pmatrix} = \frac{1}{\sqrt{2}} \begin{pmatrix} 1 & -1 \\ 1 & 1 \end{pmatrix}. \tag{2.71}$$

This operation is therefore referred to as a "$\pi/2$-pulse" in literature and has the same effect as the Hadamard transformation[3]. Experimentally, rotating the Bloch vector around the $\hat{x}-$ or $\hat{y}-$axis is possible via the discussed mechanism of Rabi oscillation by applying a resonant perturbation. Another important single-qubit operation is the NOT-gate which is defined by $NOT\ |0\rangle = |1\rangle$ and $NOT\ |1\rangle = |0\rangle$. It is obviously realized by rotating the Bloch vector around $\theta = 180^o$ by applying a π-pulse.

2.3.4 Decoherence

In the discussed approach of using the phase eigenstates of a superconducting tunnel junction as a quantum bit, the two logical states are of different energies. This implies that energy has to be interchanged with the environment to modify the angle θ. It has been discussed in the previous chapters that this is possible either by dissipating energy

[3] In quantum information theory, for the Hadamard transformation one uses the idempotent matrix $\frac{1}{\sqrt{2}} \begin{pmatrix} 1 & 1 \\ 1 & -1 \end{pmatrix}$ rather than (2.71).

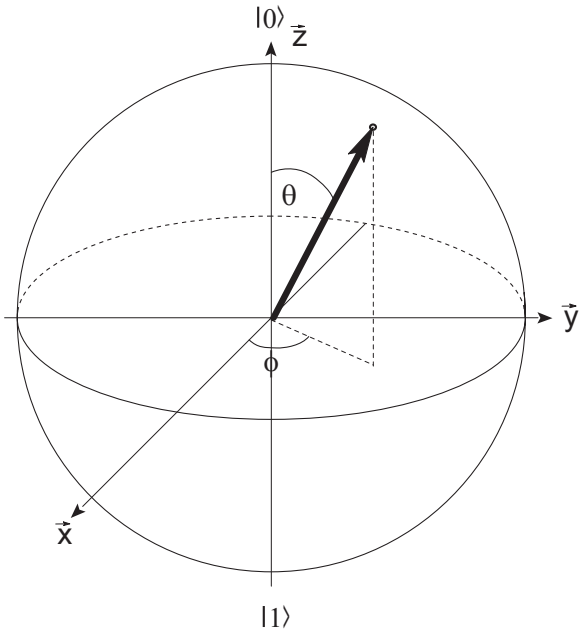

Figure 2.10: Bloch-sphere representation of the qubit state. The ground state $|0\rangle$ is represented by a vector pointing to the north pole , the state $|1\rangle$ corresponds to a vector pointing to the south pole and all equally weighted superpositions are found along the equator for $\theta = \pi/2$.

or by an alternating bias current component near the transition frequency between the levels. The Josephson junction is coupled to the enviroment mainly by the necessary biasing wires. Noise currents flowing in these lines at frequencies close to the transition frequency ω_{10} will therefore alter the occupation probabilities of the two levels by processes similar to stimulated absorption and emission. It has been shown in [58] that the probability p to measure the initially prepared state $|0\rangle$ or $|1\rangle$ would decay exponentially in time to $p \rightarrow 0.5$ if dissipation would be neglected, because noise-induced emission as well as absorption occurs at an equal rate. In fact, dissipation plays a major role and gives rise to the relaxation of an excited state to the ground state following an exponential decay law with the mean lifetime ${\Gamma_d}^{-1}$ as defined in equation (3.4).

Fluctuating currents at low frequencies result in changes of the transition frequency according to Eq. (2.20). This has the effect that the state vector drifts from the rotating frame, giving rise to a change of the phase ϕ of the Bloch vector. The probability that a given state is not altered by dephasing decreases exponentially in time, and so it is possible to define the dephasing rate Γ_ϕ. Although fluctuations in the phase ϕ do not change the level population directly, they may alter the outcome of subsequent qubit operations, because the result of any rotation around one of the three axis depends on the direction of the Bloch vector. It is, for instance, obvious from Fig. 2.10 that for $\theta = 0$ or $\theta = \pi$ the quantum state is not altered by rotations around $\vec{z}$, i.e. the ground and the excited state will not be sensitive to low frequency noise. In turn, the superposition state of the quantum bit is subject to modifications by current fluctuations even without the need to interchange energy with the environment.

Chapter 3

The flux-biased phase qubit

In this chapter, it will be discussed that the fidelity of directly current-biased phase qubits suffers from two major decoherence sources: the strong coupling to the electrical environment as given by the electrical wires connecting the junction, and the presence of quasiparticles which are created in the readout process during which a switching to the resistive state occurs. Both these problems are overcome when the junction bias current is sent through a superconducting transformer, hereby enclosing the junction in a superconducting loop and thus creating an rf-SQUID. After a brief review of the rf-SQUID principles, the technique to operate it as a phase qubit will be explained. The required ingredients for qubit bias and readout are discussed from the viewpoint of the experimentalist, arriving at a presentation of the sample layouts and a discussion of relevant parts of the measurement apparatus.

3.1 Qubit isolation

3.1.1 Dissipation in the environment

As it has been discussed in the preceding chapter, the two logical states of the phase qubit are Josephson phase eigenstates of different energies. Dissipation of energy therefore causes relaxation of the excited state towards the stable ground state of lower energy, limiting the qubit coherence time T_1.

One source of dissipation is the intrinsic subgap resistance R_{sg} of the junction dielectric, which has been introduced within the frame of the RCSJ model discussed in section 2.2.2. As it has been shown in Ref. [61], this resistance can be optimized by an epitaxial growth of the junction base electrode, hereby creating an atomically flat surface which after subsequent oxidation results in a smooth dielectric film. However, in a directly current-biased junction, the dominant source of dissipation occurs in the electrical environment. Any circuit connected to the junction will provide a complex impedance $Z_e(\omega)$ to the Josephson element which is defined as the ratio of the complex amplitudes of the voltage response of the environment to the current oscillating at frequency ω. The dissipative contributions from the external impedance $Z_e(\omega)$ are contained in its real part $R_{\mathrm{e}}(\omega) = Re[Z_e(\omega)]$. The effective junction resistance arising from the parallel shunt impedance is calculated from $1/R_{\mathrm{eff}}(\omega) = 1/R_{\mathrm{sg}} + 1/R_e(\omega)$. This expression shows that an external impedance Z_e which is large compared to the impedance of the junction Z_J will reduce dissipation to the amount determined by the

subgap resistance. By defining the reactive part of the junction impedance as [62]

$$Z_J = \sqrt{\frac{L}{C}} = \frac{1}{\omega_0 C}, \tag{3.1}$$

hereby using the inductance L defined in Eq. (2.20), the junction remains isolated from the environment response as long as $|Z_e(\omega_0)| \gg Z_J(\omega_0)$ at the frequency of the plasma oscillations ω_0. Because typical junction impedances of the order of ten ohms are comparable to these of biasing wires and on-chip transmission lines ($\sim 100\,\Omega$), a significant portion of loss may occur in these lines, resulting in enhanced damping and fast relaxation.

3.1.2 Relaxation rate

The life time of the excited state T_1 is proportional to the effective resistance R_{eff}. The decay rate from the excited state to the ground state $\Gamma_{01} \equiv 1/T_1$ can be calculated from [57]

$$\Gamma_d = \frac{2\pi(E_1 - E_0)}{\hbar} \frac{R_Q}{R_{\text{eff}}} \left|\langle 0| \frac{\varphi}{2\pi} |1\rangle\right|^2 \left[1 + \coth\left(\frac{E_1 - E_0}{2k_B T}\right)\right] \tag{3.2}$$

with $E_1 - E_0$ being the energy separation between the states $|1\rangle$ and $|0\rangle$ and $R_q = h/4e^2$ being the resistance quantum. In the limit of low temperatures $k_B T \ll E_1$, by using the harmonic oscillator matrix element [58]

$$\langle 0| \varphi |1\rangle = (2\pi/\Phi_0)\sqrt{\hbar/2\omega_{10}C}, \tag{3.3}$$

one obtains

$$\Gamma_d = 1/\, R_{\text{eff}}C. \tag{3.4}$$

For a typical junction capacitance C of order 1 pF and an effective wire resistance $R_{\text{eff}} \sim 100\,\Omega$, the life time $T_1 \equiv \Gamma_d^{-1}$ according to Eq. (3.4) is less than 1 ns, emphasizing the cruciality of special means to isolate the qubit junction from a low impedance environment.

3.1.3 Inductive isolation

To avoid energy relaxation, the electrodynamic environment of the junction must be carefully designed. One possibility is to isolate the qubit junction by means of an inductive isolation network [63], which can be realized from on-chip capacitors and superconducting inductors. The output impedance of a parallel LC-resonant filter at working frequencies beyond its resonance frequency of $1/\sqrt{LC}$ grows with its inductance L. Effective isolation therefore demands high values of both inductance and capacitance which accordingly consume large space on chip. By exploiting the Josephson inductance of an additional junction which is connected in parallel to the smaller qubit junction [10], the circuit can be kept small and the amount of isolation can furthermore be adjusted *in situ* [64]. A disadvantage of this approach, beneath the additional subgap resistance of the isolating junction, is that the qubit junction is still switching to a resistive state during the readout process. In the non-zero voltage state, the potential difference across the junction gives rise to generation of quasiparticles, which will persist for some time after the junction is reset to the superconducting state. These quasiparticles remain a source of decoherence because they provide normal current channels effectively shunting the qubit and give rise to shot-noise and charge fluctuations [65].

Above mentioned problems are avoided when the qubit junction is isolated from the bias circuitry by means of a superconducting transformer [27]. We adopted this approach in our experiments on phase qubits.

3.1.4 Isolation by impedance transformation

It has been suggested by J. Martinis *et. al.* [27] to send the current bias to the junction through a superconducting dc-flux transformer. This approach provides broadband isolation, limits the generation of quasiparticles and can be realized in compact dimensions.

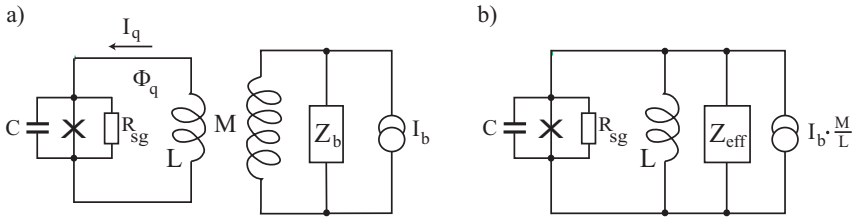

Figure 3.1: (a) Schematic of the transformer circuit. The qubit junction is embedded in a superconducting loop of inductance L, which is coupled via a mutual inductance M to the primary coil. This coil is connected by wires of low impedance Z_b to the current source. (b) Equivalent schematic of the transformer circuit. The junction remains isolated from the environment by a large effective impedance Z_{eff}.

The transformer is fabricated on-chip by placing two superconducting coils close to each other. A schematic is shown in Fig. 3.1. The primary coil is connected to the current source which generates a magnetic bias flux Φ_b proportional to the applied current I_b. Since the two coils are coupled by the mutual inductance M, the secondary coil receives a magnetic flux $\Phi_q = MI_b$ which induces a current I_q flowing through the qubit junction according to

$$I_q = \frac{\Phi_q}{L} = \frac{M}{L} I_b. \tag{3.5}$$

Here, L is the inductance of the secondary coil which will be referred to as the qubit loop in the following.

Beneath the advantage that the qubit junction remains galvanically isolated from the electronics, also the impedance of the bias wires Z_b is transformed to an effective value Z_{eff}. For an ideal (non-dissipative) transformer, the output power P_q is equal to the input power P_b,

$$P_q = I_q^2 Z_{\text{eff}} = P_b = I_b^2 Z_b. \tag{3.6}$$

This results in an impedance transformation of

$$Z_{\text{eff}} = \left(\frac{L}{M}\right)^2 Z_b, \tag{3.7}$$

where Eq. (3.5) has been used to find $I_q/I_b = M/L$. Assuming a practical ratio $L/M \approx 100$, the wire impedance $Z \approx 100\,\Omega$ is stepped up to $Z_{\text{eff}} \approx 1$ MΩ.

In addition, generation of quasiparticles is effectively reduced in this approach because the dc voltage across the junction remains zero all the time due to the superconducting short. This not only increases the coherence time but also renders an idle time

after each measurement unnecessary, which is otherwise essential to allow unpaired electrons to recondense into Cooper pairs.

3.2 rf-SQUID principles

By embedding the junction in the superconducting loop, the circuit becomes an rf-SQUID [8, 9]. In this section, the principles of the rf-SQUID are reviewed.

3.2.1 Potential energy

Flux quantization links the total flux Φ_q in the rf-SQUID loop to the phase drop φ across the junction [8],

$$\varphi + \frac{2\pi\Phi_q}{\Phi_0} = 2\pi n, \tag{3.8}$$

where n is an integer. From this equation, the phase-flux relation

$$\varphi = -\frac{2\pi\Phi_q}{\Phi_0}, \tag{3.9}$$

is deduced for n = 0. The Josephson phase φ is in turn related by the first Josephson equation (2.6) to the supercurrent flowing in the loop, which using Eq. (3.9) reads

$$I_q = -I_c \sin(2\pi\Phi_q/\Phi_0). \tag{3.10}$$

Due to the loop inductance L, this current I_q generates a magnetic flux which adds up to an externally applied flux $\Phi_{\rm ext}$. The resulting total flux threading the qubit loop Φ_q is therefore

$$\Phi_q = \Phi_{\rm ext} + LI_q = \Phi_{\rm ext} - LI_c \sin(2\pi\Phi_q/\Phi_0). \tag{3.11}$$

In Figure 3.2, Φ_q given by Eq. (3.11) is plotted for different values of the parameter $\beta_L \equiv 2\pi LI_c/\Phi_0$. For $\beta_L > 1$, the flux in the loop Φ_q is multivalued in some regions of the external flux $\Phi_{\rm ext}$, which causes Φ_q to switch in a hysteretic manner between flux states when the external magnetic flux is varied. This behavior was first observed experimentally in the year 1967 by Silver and Zimmermann [66]. The plot of the loop current versus the external flux shown in Fig. 3.2 (b) reveals that the switching between flux states is related to a reversal of the circulation direction of the loop current, while its amplitude is always smaller than the critical current of the junction.

The potential energy of the rf-SQUID is the sum of the junction energy given in Eq. (2.16) and the magnetic energy $LI_q^2/2$ which is stored in the loop inductance L. Rewriting Eq. (3.11) to obtain the circulating current in the form $I_q = (\Phi_q - \Phi_{\rm ext})/L$, we arrive at the rf-SQUID potential

$$U(\varphi) = E_J \left[1 - \cos\varphi + \frac{(\varphi - 2\pi\Phi_{\rm ext}/\Phi_0)^2}{2\beta_L}\right], \tag{3.12}$$

using the Josephson energy $E_J = \hbar I_C/2e$. This potential has the form of a parabola centered at $\varphi_0 = 2\pi\Phi_{\rm ext}/\Phi_0$ and modulated by a cosine. As it is shown in Fig. 3.3, for larges values of β_L the potential has many minima, while for $\beta_L < 1$ only a single minimum exists. Each minimum corresponds to a certain number of flux quanta in the loop, and accordingly, the mentioned switching between flux states is associated with a transition between the wells.

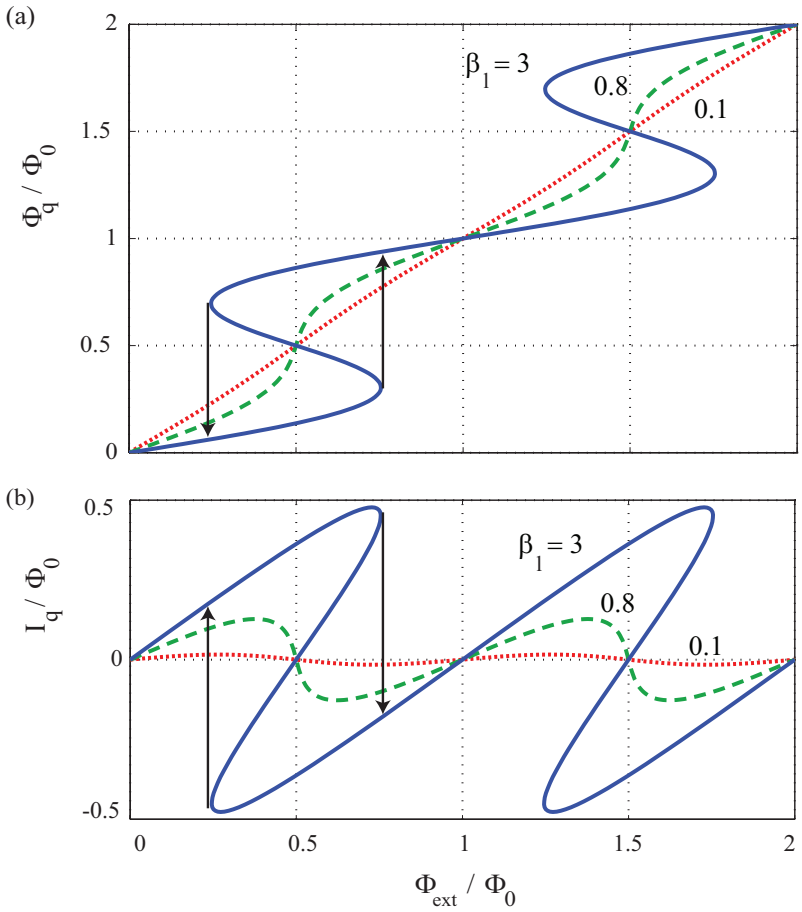

Figure 3.2: (a) Total magnetic flux in the qubit loop Φ_q/Φ_0 versus the externally applied flux Φ_{ext}/Φ_0 for different values of the parameter β_L. The switching between flux states is indicated by arrows. (b) Dependence of the current I_q/I_c circulating in the loop on the externally applied flux Φ_{ext}/Φ_0 for different values of the parameter β_L.

Aiming at operating the rf-SQUID as a phase qubit, for a given junction critical current the loop inductance is designed such that $1 < \beta_L < 4.6$. This results in a potential that has not more than two minima for all values of externally applied flux and one single minimum for $\Phi_{\text{ext}} \approx 0$. If β_L is larger than 4.6, it is still possible to operate the rf-SQUID as a phase qubit, but in this case more than one minima exist in the potential at all values of external flux, and therefore it becomes more difficult to initialize the flux state of the qubit in a certain well.

By changing the external magnetic flux Φ_{ext}, the double well potential appears to be tilted as plotted in Fig. 3.4 (a). This allows to adjust the depth of the potential wells *in situ*. Analogously to the critical current I_c of a biased Josephson junction, for the rf-SQUID there exists a critical flux Φ_c where the potential barrier between the shallow and the deep well vanishes. Its value can be found from the condition that the inflection point of the potential coincides with the position of the minimum of the

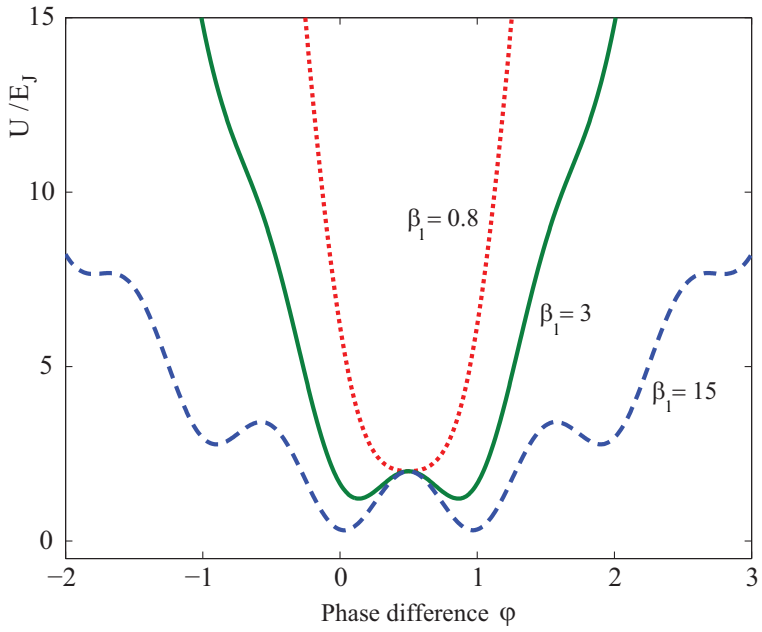

Figure 3.3: Potential of the rf-SQUID for several values of the β_L-parameter at an external magnetic flux of $\Phi_{\rm ext} = \Phi_0/2$.

shallow well [67]. While the extrema of the potential Eq. (3.12) are located at φ given by

$$\varphi - \frac{2\pi\Phi_{\rm ext}/\Phi_0}{\beta_L} = -\sin\varphi, \tag{3.13}$$

the inflection point which satisfies $U''(\varphi) = 0$ is located at φ_c, for which

$$\cos\varphi_c = -1/\beta_L \tag{3.14}$$

independently of the external flux $\Phi_{\rm ext}$. Inserting the solution for φ_c into Eq. (3.13) results in the critical flux for a two-well potential [67]:

$$\Phi_c = \pi/2 + \sqrt{\beta_L^2 - 1} + \arcsin(1/\beta_L). \tag{3.15}$$

Cubic approximation

For phase qubit operation, one potential well is made very shallow by adjusting the flux bias close to the critical flux such that $0 < \Phi_c - \Phi_{\rm ext} \ll \Phi_c$. In this case, a cubic approximation of the potential can be used [67] to obtain analytic expressions for the potential parameters. For a parameter $\epsilon = 2(\Phi_c - \Phi_{\rm ext})/\sqrt{\beta_L^2 - 1} \ll 1$, the barrier height is

$$\Delta U = \frac{2}{3} E_J \, \epsilon^{3/2} \sqrt{1 - \beta_L^{-2}}. \tag{3.16}$$

The small oscillation frequency ω_0 in the shallow potential well, obtained according to Eq. (2.19) from the curvature of the approximated potential and the effective mass

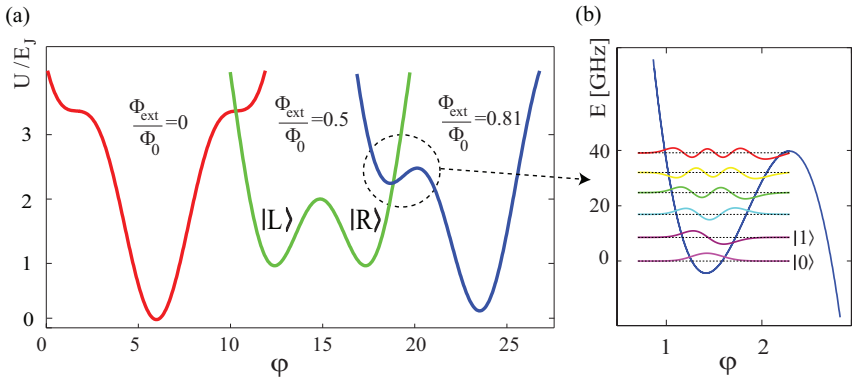

Figure 3.4: (a) Potential for different external magnetic fluxes (each curve is offset by φ=6 for better visibility). (b) Zoom into the shallow well showing the discrete energy levels and the wave functions of the corresponding quantum states.

given by Eq. (2.15), is

$$\omega_0 = \epsilon^{1/4}(1-\beta_L^{-2})^{1/4}\sqrt{E_J/m}. \tag{3.17}$$

Fig. 3.5 (a) shows the external flux dependence of the small oscillation frequency as calculated by the approximation Eq. (3.17) as well as an exact solution obtained from the curvature of the potential at the minimum according to Eq. (2.18).

Using these formulas, a good estimate of the number of levels in a shallow well is

$$N \approx \frac{\Delta U}{\hbar\omega_0} = \frac{2}{3\hbar}\epsilon^{5/4}(1-\beta_L^{-2})^{1/4}\sqrt{mE_J}, \tag{3.18}$$

which is plotted in Fig. 3.5 (c). Depending on the junction parameters, the deep right potential well contains several hundred states.

3.2.2 Energy levels

The positions of the energy levels E_n inside the shallow well are calculated from a solution to the stationary Schrödinger equation

$$H\,|\Psi\rangle = E\,|\Psi\rangle \tag{3.19}$$

with the Hamiltonian

$$H = \frac{\hat{p}^2}{2m} + U(\varphi), \tag{3.20}$$

where $\hat{p} = -i\hbar(\delta/\delta\varphi)$ is the momentum operator. By dividing the parameter space φ into K steps, equally separated by a distance d, the wavefunction $\Psi(x_j)$ is discretized to the positions $x_j = jd$ with $j = 0...K-1$. Tunneling to the deep well is neglected by employing the boundary conditions $\Psi(x_0) = \Psi(x_{K-1}) = 0$ and restricting the parameter space to the shallow potential well. The upper interval limit is therefore chosen to be at the maximum of the potential barrier, which gives equal results as the frequently used truncated modified potential [68].

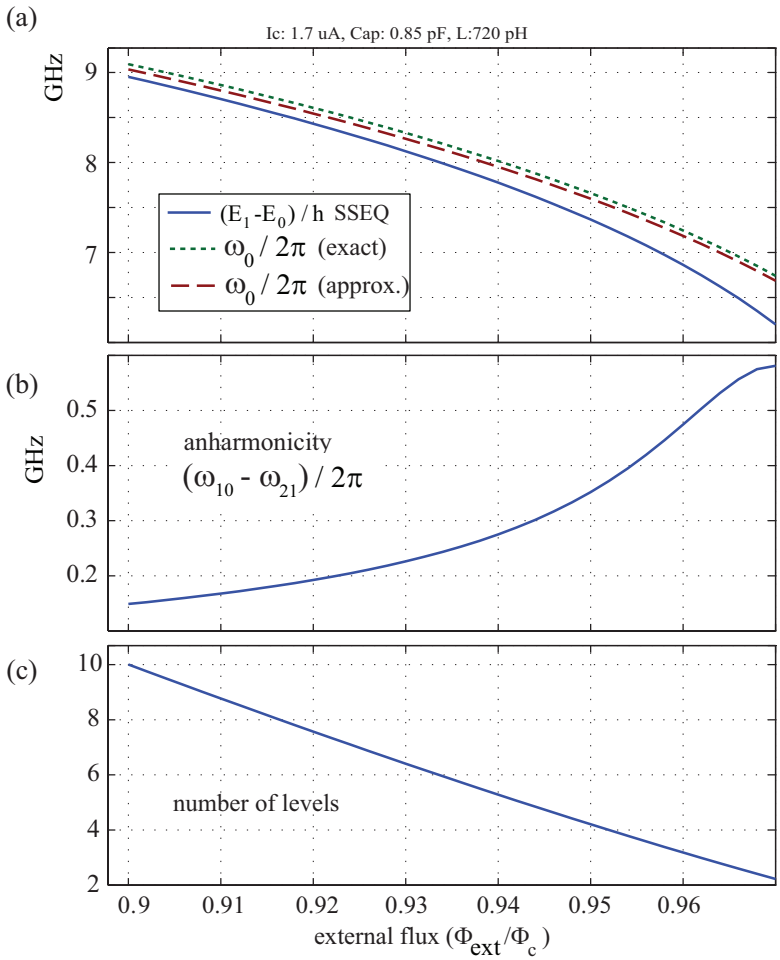

Figure 3.5: (a) Solid line: Transition frequency between the ground and first excited states, calculated numerically from the stationary Schrödinger equation. Dashed line: Approximation to the small oscillation frequency as given in Eq. (3.17). Dotted line: small oscillation frequency calculated from the curvature of the exact potential. (b) Difference in transition frequencies ω_{10} and ω_{21}. (c) Approximated number of levels in the shallow potential well, Eq. (3.18). Parameters of sample `UCSB-SiN`.

By approximating the second derivative $\delta^2\Psi/\delta\varphi^2$ as

$$\frac{\delta^2\Psi}{\delta\varphi^2} \approx \frac{1}{d^2}\left(\Psi(x_{j-1} - 2\Psi(x_j + \Psi(x_{j+1})\right), \tag{3.21}$$

Eq. (3.19) is evaluated at each point x_j. This results in a set of $K-1$ linear equations which are written as a matrix equation. Applying standard numerical algorithms, the position of the nth energy levels E_n as well as the corresponding wavefunction Ψ_n result as the nth eigenvalue and eigenfunction, respectively, of the matrix. In Fig. 3.4 (b), the resulting wavefunctions of such a calculation are shown, for comparison using qubit parameters as stated in Ref. [68] of $C = 0.85$ pF, $L = 720$ pH, $I_c = 1.7\mu$A and an external flux of $\Phi_{\rm ext} = 0.845\Phi_0$. For the same parameters, Fig. 3.5 (a) shows the

dependence of the transition frequency $\omega_{10} = (E_1) - (E_0)/\hbar$ between the ground and first excited states. As it is expected, the transition frequencies between the computed eigenstates are smaller than the oscillation frequencies of the harmonic approximation to the potential well.

In Fig. 3.5 (b), the difference between the transition frequencies ω_{10} and ω_{21} is plotted, showing that the anharmonicity of the potential well increases as the external flux approaches the critical flux Φ_c.

3.2.3 Escape rates

Inter-well transitions occur from a shallow well to a neighboring deeper well by similar mechanisms as discussed for the current-biased Josephson junction, namely quantum tunneling and thermal activation. In contrast to the biased junction, beyond the potential barrier there exists not a continuum but a large number of discrete states. If two states confined in the left and right potential well have the same energy such that the levels align, tunneling occurs at an enhanced rate. This process is called resonant tunneling and has been firstly observed experimentally by Lukens *et. al.* [69]. Neglecting resonant tunneling, the quantum tunnel rate Γ_n from energy level n can be calculated using the semiclassical Wentzel-Kramers-Brillouin (WKB) approximation,

$$\Gamma_n \approx \frac{\omega_0}{2\pi} f_n \exp(-iS_n/\hbar). \tag{3.22}$$

Here,

$$S_n = \int_{\varphi 1}^{\varphi 2} \sqrt{2m[U(\varphi) - E_n]}\, d\varphi \tag{3.23}$$

is the effective action evaluated between the classical turning points φ_1 and φ_2 at the energy $E_n = (n + 1/2)\hbar\omega_0$ of state $n = \{0, 1, ...\}$. The numerical factor f_n is given by [70]

$$f_n = \frac{\sqrt{2\pi}}{n!} \left(\frac{n + 1/2}{e} \right)^{n+1/2} \tag{3.24}$$

and provides a very small correction to the reduced attempt frequency in an anharmonic potential well. The total tunneling rate follows from the sum over all levels weighted by their population probability p_n according to Boltzmann's distribution

$$\Gamma = \sum_{n=0}^{\infty} p_n \Gamma_n, \quad p_n = \frac{\exp(-E_n/k_B T)}{\sum_{n=0}^{\infty} \exp(-E_n/k_B T)}, \tag{3.25}$$

where T is temperature.

In Fig. 3.6 (a), the result of a numerical calculation of the tunnel rate Eq. (3.22) is presented for the ground $n = 0, p_0 = 1$ and the excited state $n = 1, p_1 = 1$. Additionally shown is a calculation using the analytical approximation of the WKB tunnel rate for low damping Eq. (2.31) and the cubic approximation to the small oscillation frequency and barrier height, Eqs. (3.17) and (3.16). While in the logarithmic plot the numerical and approximated results are hardly distinguishable, Fig. 3.6 (b) reveals that they may differ by up to about 100 kHz. Figure 3.6 (c) contains a plot of the ratio Γ_1/Γ_0. The more exact numerical result shows a stronger dependence of this ratio on the external flux but differs not more than a factor of about 2 from the result obtained using the cubic approximation even at low external flux. Closer to the critical flux above $\Phi_{\mathrm{ext}}/\Phi_c \approx 0.975$, the tunnel rates from ground and excited states differ by a factor of less than 1000.

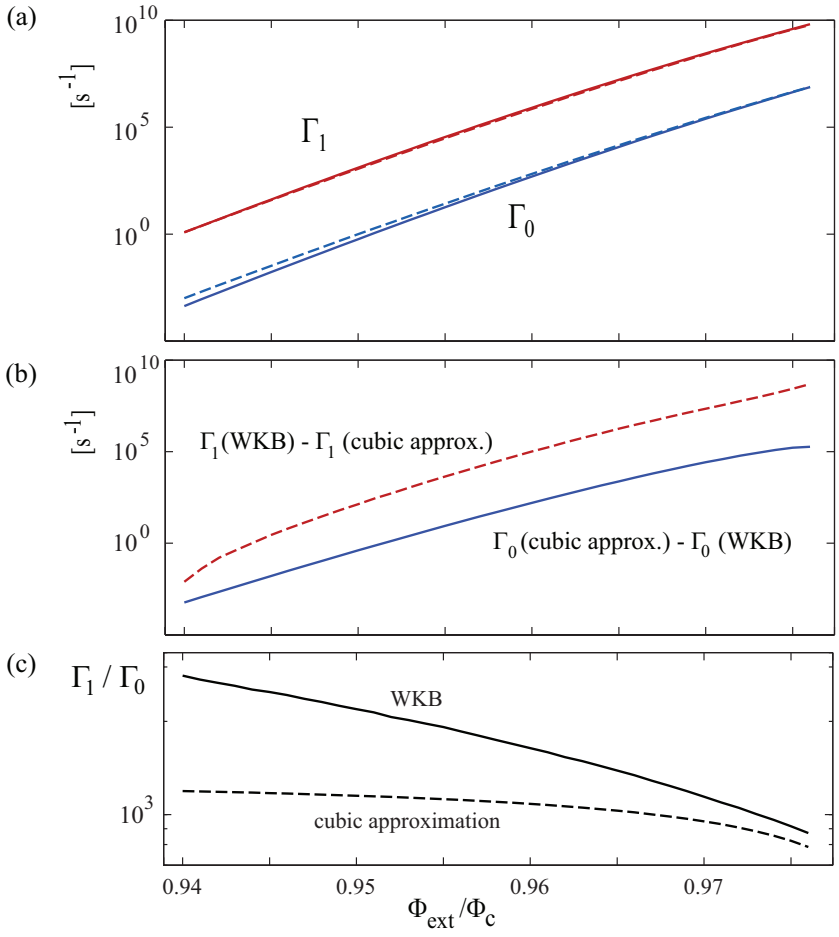

Figure 3.6: (a) Rates of quantum tunneling from the ground state and the first excited state in an rf-SQUID. Solid lines are computed numerically and dashed lines are obtained using the cubic approximation. (b) Difference between numerical and approximated results for the ground state rate Γ_0 (solid line) and the excited state Γ_1 (dashed line). (c) Ratio of the tunnel rates Γ_1/Γ_0, calculated numerically (solid line) and using the cubic approximation (dashed line). Sample parameters were I_c = 1.7 μA, L = 0.72 nH and C = 0.7 pF for comparability to [68] and are similar to sample `UCSB-SiN`.

3.3 Qubit operation

The operation of the single junction interferometer as a phase qubit is accomplished by applying a flux bias sequence composed of dc- and microwave frequency signals as illustrated in Fig. 3.7. In this section, an overview of the necessary steps is given, while qubit measurement and flux state readout are discussed in more detail in Sec. 4.3 and Sec. 3.4, respectively.

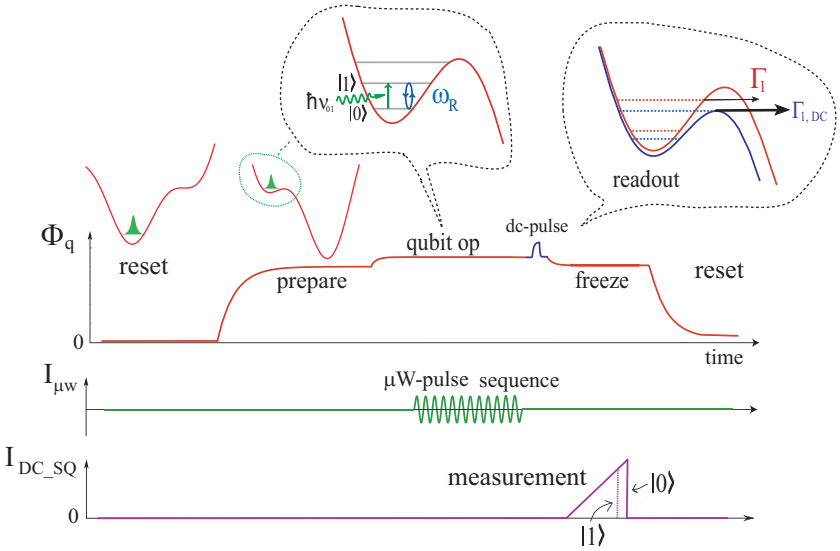

Figure 3.7: Top: Timing profile of the magnetic flux bias Φ_q applied to the qubit. Bottom: Bias current sent to the readout SQUID.

I) Initialization. To initialize the qubit, its flux state is reset to a defined value and its phase state to the one of lowest energy in the corresponding potential well. Given that the parameter $\beta_L < 4.6$, it suffices to switch the applied magnetic flux to zero such that only a single potential well remains. Keeping this flux level for a time much larger than the energy relaxation time T_1 ensures that the qubit is initialized in the ground state $|0\rangle$. For larger values of $\beta_L > 4.6$ there exist always more than one potential minima. Initialization in a certain well in this case is still possible by using the so-called 'shaker' technique [71], in which an oscillating external flux is applied to induce escape from all potential wells of higher energy towards the global minimum.

II) Preparation. The external flux Φ_q is adjusted adiabatically to a value near the critical flux Φ_c to make the potential well in which the phase is confined very shallow. While the exact value of Φ_q can be chosen to result in the desired energy difference between the two qubit states, it underlies two limitations. On the one hand, it must not be too large such that the first excited state does not escape from the shallow well during the qubit operation. On the other hand, a smaller value of Φ_c results in a deeper potential well which is more harmonic, *i.e.* the transition frequencies between neighboring states are less distinct from each other. The external flux must hence be large enough to result in a potential well

of sufficient anharmonicity, ensuring that higher excited states are not populated by a microwave tuned to the $|0\rangle$ to $|1\rangle$ transition frequency.

III) Qubit operation. After the external flux has reached the working point, logical qubit operations are performed by a sequence of dc-currents and resonant microwave pulses. Since microwave pulses of frequency $\omega_{\mu w} = E_1 - E_0/\hbar$ change the individual state population undergoing Rabi oscillation, they can be used to realize the Haddamard transformation and the logical NOT gate. A dc-pulse can be used to implement the phase gate by introducing a small detuning which changes the Larmor frequency and hence the precession velocity of the Bloch vector.

IV) Qubit measurement. After sending the microwave pulse, a short but still adiabatic dc-flux pulse is applied which raises the excited state close to the top of the potential barrier. It is possible to adjust the amplitude and duration of this measurement pulse such that only the excited state tunnels to the deep right well, whereas the ground state remains in the shallow left well. Thereby, the phase eigenstates $|0\rangle$ and $|1\rangle$ are mapped to macroscopically distinct flux states in the shallow and deep wells, respectively. This technique [34] allows to distinguish the phase eigenstates with a fidelity [68] close to 100 %.

IV) State readout. After application of the measurement dc-pulse, the applied magnetic flux is reduced, hereby increasing the barrier height separating the two wells in order to avoid further inter-well transitions. Whether the qubit is now in the left or right well is determined by measuring the corresponding magnetic field in the qubit loop by means of an inductively coupled dc-SQUID.

3.4 Readout

Several methods can be used to measure the flux state of the phase qubit. One of them [72] directly determines the circulation direction of the loop current by a measurement of the critical current of an additional junction incorporated in the loop. Less invasive techniques are based on a measurement of the flux generated from the loop current by using an inductively coupled dc-SQUID. In this section, the circuit design requirements for the widely used method of flux detection by a switching-current measurement of the dc-SQUID are discussed. Beyond that, the principles of a dispersive readout based on a measurement of the dc-SQUID inductance are presented as an outlook.

3.4.1 Principles of the dc-SQUID

A dc-SQUID consists of two Josephson junctions embedded in a superconducting loop [8, 9] as shown in Fig. (3.8).

From the flux quantization condition, the relation between the phase differences across the two junctions φ_1 and φ_2 is found as

$$\varphi_1 - \varphi_2 = \frac{2\pi}{\Phi_0}\Phi_{\mathrm{sq}} = \frac{2\pi}{\Phi_0}(\Phi_{\mathrm{a}} + LJ), \tag{3.26}$$

where the flux in the dc-SQUID loop Φ_{sq} has contributions from the externally applied flux Φ_{a} and the flux generated from the current J circulating in the loop of inductance $L_{\mathrm{sq}}= L_1 + L_2$. An applied bias current I_b distributes among junctions 1 and 2 equally,

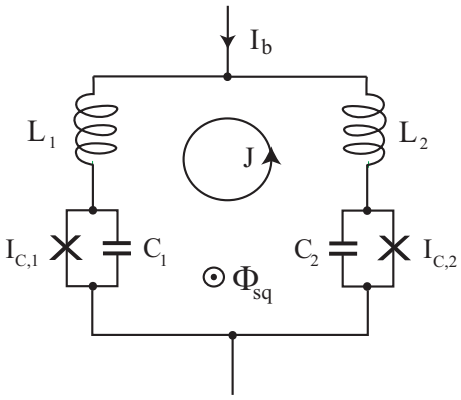

Figure 3.8: Schematic of the dc-SQUID.

such that $I_1 = I_b/2 + J$ and $I_2 = I_b/2 - J$. Using Kirchhoff's law and the first Josephson equation (2.6) as in the RCSJ model, we obtain two equations

$$\begin{aligned} I_1 &= I_{c,1} \sin\varphi_1 + \frac{\Phi_0}{2\pi} C_1 \ddot{\varphi}_1 \\ I_2 &= I_{c,2} \sin\varphi_2 + \frac{\Phi_0}{2\pi} C_2 \ddot{\varphi}_2 \end{aligned} \tag{3.27}$$

which are linked by Eq. (3.26). Here, $I_{c,1}$ and $I_{c,2}$ are the junction critical currents, C_1 and C_2 are their capacitances and an infinite junction resistance (which corresponds to zero damping) has been assumed. These equations can be solved graphically [73] or numerically for the flux dependence of the maximum supercurrent $I_{\mathrm{c,sq}}$ through the dc-SQUID. In the simplified case of identical junctions $I_{c,1} = I_{c,0} = I_0$, equal inductances $L_1 = L_2$ and small loop inductance $\beta_{\mathrm{L,SQ}} = 2\pi\ L_{\mathrm{sq}} I_0/\Phi_0 \ll 1$, the critical current depends on the applied flux as

$$I_{\mathrm{c,sq}} = 2I_0 \cdot \left| \cos\left(\pi \frac{\Phi_{\mathrm{sq}}}{\Phi_0}\right) \right|. \tag{3.28}$$

The modulation depth of the critical current is reduced for nonzero values of $\beta_{\mathrm{L,SQ}}$. At $\beta_{\mathrm{L,SQ}} = \pi$ the minimal critical current is 50 % of $I_{\mathrm{c,sq}}$, for larger $\beta_{\mathrm{L,SQ}} \gg \pi$ the modulation depth decreases as $\pi/\beta_{\mathrm{L,SQ}}$ [9].

The equations of motion (3.27) define the dc-SQUID potential, which is two-dimensional in the two degrees of freedom φ_1 and φ_2. Assuming identical junctions $I_{c,1} = I_{c,0} = I_0$, equal inductances $L_1 = L_2$ and transforming to new coordinates $x = (\varphi_1 + \varphi_2)/2$ and $y = (\varphi_1 - \varphi_2)/2$, the potential for the symmetric dc-SQUID is

$$U_{\mathrm{dc}}(x,y) = \frac{\Phi_0 I_0}{\pi} \left[-\frac{I_b}{2I_0} x - \cos x \cos y + \beta_{\mathrm{L,SQ}}^{-1} \left(y - \frac{\pi \Phi_a}{\Phi_0} \right)^2 \right] \tag{3.29}$$

For small loop inductance $\beta_{\mathrm{L,SQ}} << 1$, the parabolic modulation in the y direction is very steep, restricting the motion of the virtual particle to an one-dimensional washboard potential. For large $\beta_{\mathrm{L,SQ}} > 1$, the potential has a series of wells of different depths in which the SQUID can be trapped, giving rise to degeneration of the zero-voltage state. Increasing the bias current I_b tilts the potential in the direction of x, and the phase escape from a well to the running state occurs along a trajectory that

connects the minimum of the well with the lowest saddle point in the vicinity. For a certain zero-voltage state, the critical current $I_{\mathrm{c,sq}}$ can be found from a potential analysis by imposing the constraint that at $I_b = I_{\mathrm{c,sq}}$ the minimum of one well coincides with a neighboring saddle point [74]. Any asymmetry in either the critical current of the two junctions or the inductances between the two branches results in a shift of the flux value where the critical current of the SQUID is maximum [75]. Experimental data of the mean switching current dependence on external flux, obtained from an asymmetric dc-SQUID of $\beta_{\mathrm{L,SQ}} \approx 25$ and critical current $I_{\mathrm{c,sq}} \approx 21.8\mu A$, is shown in Fig. 3.9.

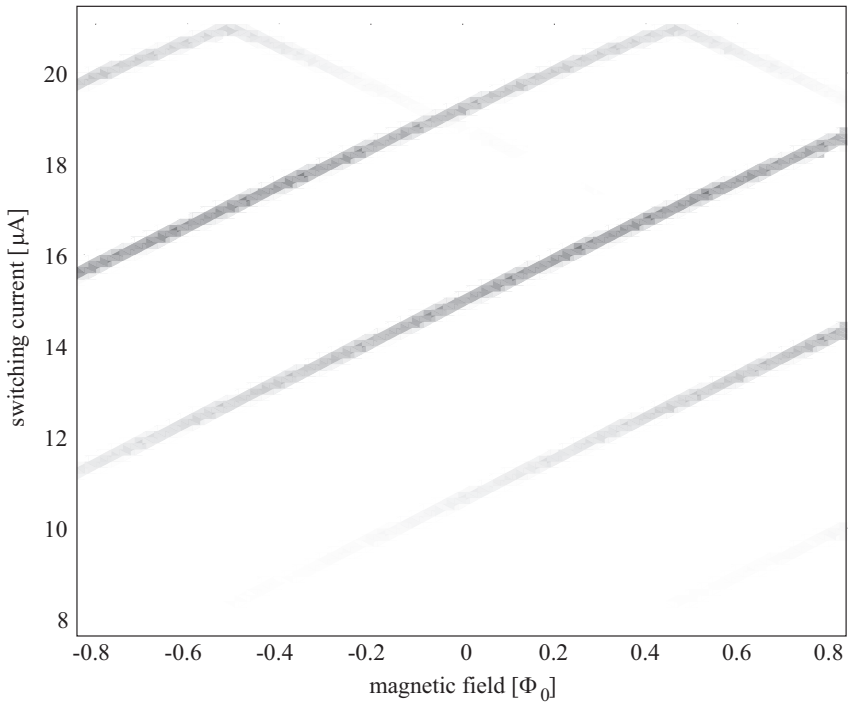

Figure 3.9: Switching currents vs. magnetic bias flux for an asymmetric and large inductance dc-SQUID. The grey scale reflects the switching probability, increasing from white to black. At a given bias flux, several peaks in the switching-current distribution reflect the degeneracy of the zero-voltage state in the two dimensional washboard potential. Sample: `Hyp100`.

During operation of the phase qubit, the bias current of the dc-SQUID is set to a value that minimizes the coupling between the dc-SQUID's degree of freedom and the flux that it receives from the qubit [76]. For example, a symmetric dc-SQUID of low inductance $\beta_{\mathrm{L,SQ}} < 1$ can be described by a single degree of freedom φ_{sq}, which is related to its bias current by the Josephson relation

$$I_{\mathrm{sq}} = I_{\mathrm{c,sq}} \sin\varphi_{\mathrm{sq}} = 2I_0 \cdot \left|\cos\left(\pi\frac{\Phi_{\mathrm{sq}}}{\Phi_0}\right)\right| \sin\varphi_{\mathrm{sq}}, \tag{3.30}$$

where Eq. 3.28 is used. Solving this equation for φ_{sq} results in

$$\varphi_{\mathrm{sq}} = \sin^{-1}\left[\frac{I_{\mathrm{sq}}}{2I_0}\left|\cos\left(\pi\frac{\Phi_{\mathrm{sq}}}{\Phi_0}\right)\right|^{-1}\right], \tag{3.31}$$

which shows that for zero bias current $I_{\rm sq} = 0$ the dc-SQUID phase $\varphi_{\rm sq}$ is not correlated to the external flux $\Phi_{\rm sq}$ and hence the dc SQUID remains isolated from the qubit.

3.4.2 Switching-current readout

As it was described before, after the logical qubit operations its phase eigenstates are projected into separate wells of the qubit potential which differ by one flux quantum in the qubit loop. In this section, I describe design requirements and methods of data evaluation which allow to detect this flux signal by switching-current measurements on a readout dc-SQUID.

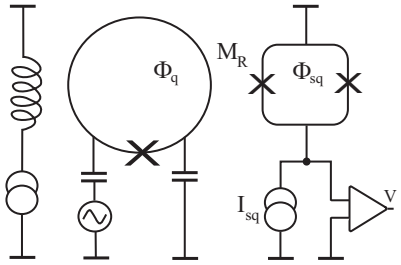

Figure 3.10: Schematic of the phase qubit system. The coil in the left part of the figure provides bias magnetic flux Φ_q to the qubit. The junction in the qubit loop is capacitively coupled to a microwave source for resonant qubit control. The dc-SQUID is coupled to the qubit loop by the mutual inductance M_R to read out the qubit flux state by a switching-current measurement.

Fig. 3.10 shows that the readout dc-SQUID is coupled by the mutual inductance M_R to the qubit loop. The flux signal that must be detectable is

$$\Delta\Phi_{\rm sq} = M_R \Delta I_q \approx \frac{M_R}{L}\Phi_0, \tag{3.32}$$

where $\Delta I_q \approx I_c$ (see Fig. 3.2) is the change of the circulating current associated to a change of the qubit potential well. For the reasons discussed in section 3.1.4, sufficient qubit isolation requires the ratio M_R/L to be $\approx 10^{-2}$, which limits the flux signal $\Delta\Phi_{\rm sq}$ to the order of 10 mΦ_0. The method to detect this small flux change is based on the magnetic field dependence of the dc-SQUID critical current $I_{\rm c,sq}$, which is periodic in Φ_0 as discussed in the preceding section.

The most direct way to determine $I_{\rm c,sq}$ is to record the statistical probability distribution $P(I_b)$ of bias currents $I_{\rm sw}$ at which the SQUID switches to the non-zero voltage state. In a widely used method [77], a linear current ramp dI_b/dt is used, in which case the switching-current histogram takes the form

$$P(I_b) = \Gamma(I_b, \Phi_a)\left(\frac{dI_b}{dt}\right)^{-1}\left(1 - \int_0^I P(I')\,dI'\right). \tag{3.33}$$

Here, $\Gamma(I_b, \Phi_a)$ is the escape rate from the superconducting state which depends exponentially on the critical current $I_{\rm c,sq}$ and thus on the flux in the dc-SQUID Φ_a. The result of a numerical calculation of the histogram Eq. (3.33), using the quantum tunnel rate Eq. (2.31), is shown in Fig. 3.11 (a).

In order to detect flux changes, a practically useful observable is the mean switching current $\langle I_{\rm sw}\rangle$, which directly relates to the SQUID critical current. The statistical

spread σ (the standard deviation which is also the width of the probability distribution histogram $P(I_b)$) originates in the probabilistic nature of the switching process, and has contributions from quantum, thermal and bias current fluctuations [78].

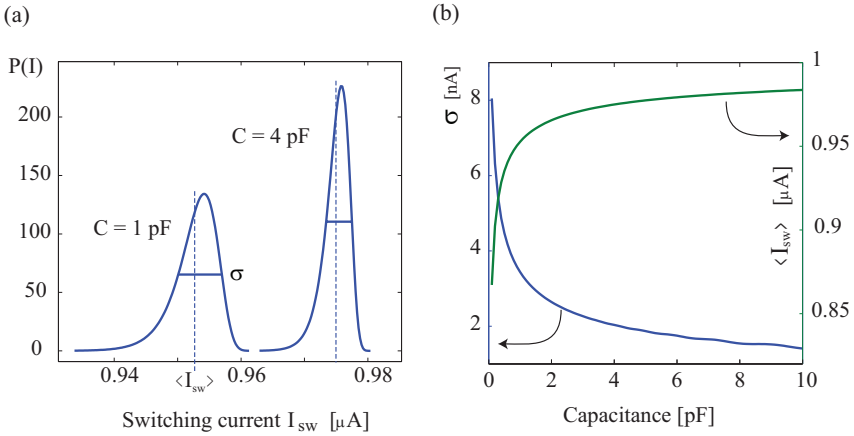

Figure 3.11: (a) Switching current distributions $P(I_{\rm sw})$ for a single small Josephson junction of 1 μA critical current with capacitances of C=1 pF (left histogram) and C=4 pF (right histogram). The corresponding mean switching currents are indicated by vertical dashed lines, and the standard deviations σ by horizontal lines at half the histogram height. (b) Dependence of the histogram width σ (left axis) and mean switching current (right axis). Both plots are calculated from the quantum tunnel rate Eq. (2.31) and a ramp rate of 1 mA/s.

Single-shot readout

In order to distinguish the two qubit flux states $|L\rangle$ and $|R\rangle$ at maximum contrast, the histograms $P(I_b)$ corresponding to these states must not overlap. If this criterium is fulfilled, it becomes possible to determine by a single switching current measurement whether the qubit was in the left or right well. This so-called *single shot* readout requires the flux difference $\Delta\Phi_{\rm sq}$ to result in a shift of the mean switching current $\Delta I_{\rm sw}$ which is at least about four times larger than the standard deviation (see Fig. 3.12).

Using Eq. (3.32), the *single-shot* criterium can be written as

$$\Delta I_{\rm sw} = \frac{M_R}{L}\frac{\partial I_{\rm sw}}{\partial \Phi_a} \gtrsim 4\sigma, \tag{3.34}$$

In this formula, $\partial I_{\rm sw}/\partial\Phi_a$ is the change of the mean switching current with flux in the dc-SQUID, which depends on the working point and is zero at the maximum of the $I_{\rm c,sq}(\Phi_a)$ relation. Large values of $\beta_{\rm L,SQ}$, which may be necessary to achieve the required mutual inductance M_R, reduce the modulation of the mean switching current as discussed in the previous section.

The mutual inductance mediates dissipation in the dc-SQUID and generates back-action to the qubit. While the back-action scales as $M_R^2/LL_{\rm sq}$, dissipation in the qubit is proportional to the inverse effective dc-SQUID damping impedance $Z_{\rm sq}^{-1}$, which is transformed to the qubit via $Z^{-1} = Z_{\rm sq}^{-1}(M_R/L)^2$. A detailed discussion of decoherence effects due to coupling to the readout SQUID is given in Ref. [76].

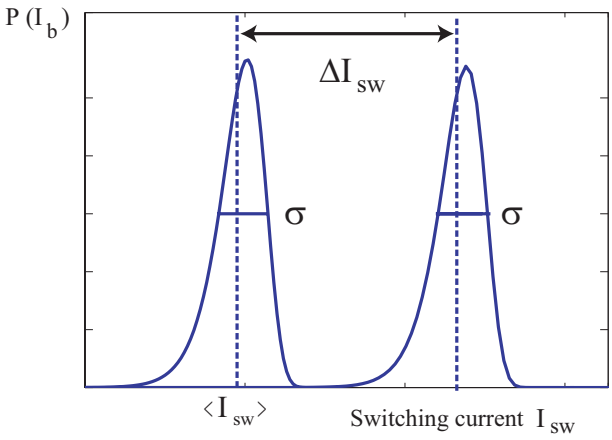

Figure 3.12: Two simulated switching current histograms, corresponding to the states $|L\rangle$ and $|R\rangle$, respectively. In this example, the shift of the mean switching current $\Delta I_{\rm sw}$ is much larger than the standard deviation σ, which allows for single-shot readout.

To fulfil the criterium Eq. (3.34) also at lower M_R, one possibility is to reduce the histogram width σ by means of additional shunt capacitors to the dc-SQUID junctions, which is a frequently used method in experiments on flux qubits [79]. In Fig. 3.11 (b), it is shown how standard deviation and mean value of the switching current distribution change with additional shunt capacitances, calculated for a small junction in the quantum tunneling regime. In contrast, if the escape process is dominated by thermal escape over the barrier, higher capacitances result in a small increase of σ. The reason for this behavior is that in the thermal activation rate Eq. (2.29) the capacitance (which is contained in the small oscillation frequency ω_0) appears only in the preexponential factor.

An other option towards obtaining higher readout contrast is to increase $\partial I_{\rm sw}/\partial\Phi_a$ by using an asymmetric dc-SQUID and setting the working point on the steeper slope of the $I_{\rm c,sq}(\Phi_a)$ dependence [9]. An asymmetric dc-SQUID has furthermore the advantage that the maximum of its critical current is shifted from zero flux, and therefore no SQUID bias flux is required to move the working point away from the maximum.

A minor improvement in the qubit flux signal is obtainable by designing the qubit with a larger β_L-parameter, which as mentioned may bring qubit initialization difficulties along. The difference in flux between two qubit states corresponding to neighboring potential wells approaches one flux quantum only for larger β_L parameters. This can be seen for example by comparing the distance between two minima in the plot of the qubit potential vs. external flux, Fig. 3.3. For smaller β_L, the minima move closer together due to the stronger quadratic modulation of the potential, reducing the qubit signal. For the quoted practical value of $\beta_L = 4.6$, this flux difference is about 0.9 Φ_0, and increases by 4% at $\beta_L = 7$.

Data evaluation

The standard method to calculate the probability that the qubit is in a flux state corresponding to the right potential well is to introduce a threshold value $I_{\rm tresh}$ of switching current, as indicated in Fig. 3.13, and relating $N(I_{\rm sw} > I_{\rm tresh})$, the number of counts above this threshold, to the total number of events N:

$$P(|R\rangle) = \frac{N(I_{\rm sw} > I_{\rm tresh})}{N}. \tag{3.35}$$

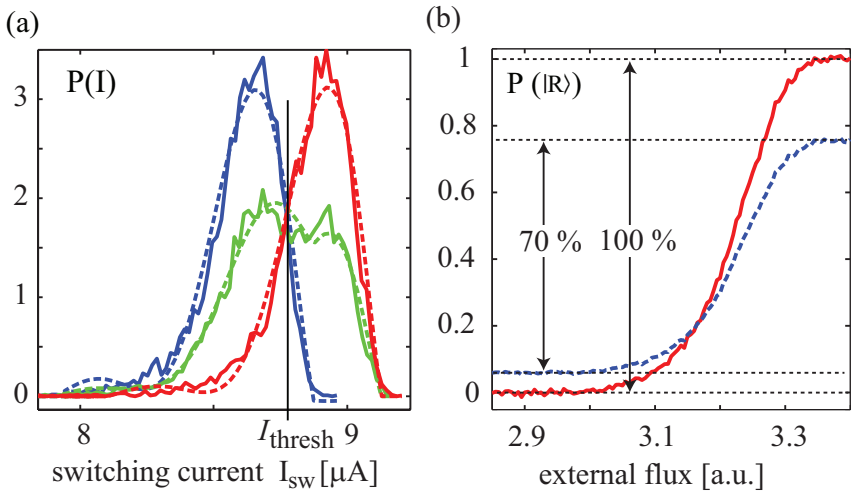

Figure 3.13: (a) Switching current distributions which are broadened due to thermal activation. Left and right histograms correspond to the qubit being in state $|R\rangle$ and $|L\rangle$, respectively. The smaller histogram corresponds to equal probability of the two states. Dashed lines are polynomial fits. (b) The probability to measure the state $|R\rangle$ versus externally applied flux. The blue dotted curve is calculated using the standard method, resulting in a maximum contrast of 70%. The red solid curve has been obtained from weighted fits to the histograms, and reconstructs the two states with 100% contrast.

If the two histograms are not completely separated, switching current events in the region of histogram overlap can not be attributed to one or the other state, and loss of contrast occurs. This is shown in Fig. 3.13 (b) as the dashed curve calculated according to Eq. (3.35).

In practical qubit measurements, statistics about the state population are always acquired because of the probabilistic nature of quantum mechanics. A single shot measurement is therefore not necessary as long as it is still possible to reconstruct the individual state contribution from the statistical data set.

Our method to reconstruct the qubit state population from overlapping histograms beyond the single shot limit is the following. The qubit is first prepared in state $|L\rangle$, recording the switching current probability histogram $P(I)$ generated by only this state. This histogram is fitted to an arbitrary function $f_L(I)$. For simplicity, we are using a 10 degree polynomial truncated between minimal and maximal measured switching currents as the fitting function. Fitting to a physically correct distribution, which is an integral function of the exponential escape rate, would require more computing time and an adaption of the model depending on the sample. The same procedure is repeated on a histogram obtained from measurements of a qubit prepared purely in the state $|R\rangle$, obtaining the fitting function $f_R(I)$. All further histograms are then fitted to the function

$$P(I) = P(|1\rangle)\, f_R(I) + [1 - P(|1\rangle)]\, f_L(I), \tag{3.36}$$

hereby obtaining $P(|1\rangle)$, the population of the excited qubit state $|1\rangle$, as the only fitting paramter.

In Fig. 3.13 (a), histograms of the qubit prepared in state $|L\rangle$, $|R\rangle$ and in a superposition state are shown together with the fitting functions drawn as dashed lines. Figure

3.13 (b) demonstrates that the excited qubit state population $P(|1\rangle)$ calculated by this procedure recovers full contrast.

An advanced application of this data evaluation method considers multi-qubit circuits. After completion of a quantum algorithm, each qubit state must be read out. The number of necessary readout SQUIDs can be reduced by coupling more than one qubit inductively to one single dc-SQUID and employing the fitting procedure to reconstruct the individual qubit flux states. The qubit signals generate a flux in the dc-SQUID of

$$\Phi_{\mathrm{sq}} = \sum_i M_i I_{\mathrm{c,i}} (-1)^{si}, \tag{3.37}$$

where $si \in \{0, 1\}$ is the state of qubit i and M_i is the mutual inductance between qubit i and the dc-SQUID. A simple calculation shows that for two qubits the relative difference between M_2 and M_1 must be a factor of two to be able to distinguish the four possible states. Since our method allows to reduce the coupling strength to the dc-SQUID for all qubits by a factor of about 1/2, no further decoherence is expected. The possibility to use the bias-current dependent Josephson inductance of a dc-SQUID to control the coupling strength between two flux qubits has already been shown experimentally [80]. Using the same dc-SQUID both as a controllable coupler and readout device is appealing to simplify scaling up of Josephson qubit circuits towards a multi-qubit quantum processor.

3.5 Sample design

Experiments were carried out using samples of different origins and materials. Our own sample designs were submitted for fabrication to VTT Research Facility [81] and the commercial foundry Hypres Inc. [14]. Although the circuit specifications for the offered standard niobium-based optical lithography were limited to relatively large Josephson junction sizes and silicon-oxide as a dielectric, we successfully managed to operate these samples in the quantum coherent regime.

3.5.1 Niobium - SiO_x - based standard fabrication processes

The layout of a phase qubit circuit compatible with the Hypres foundry fabrication process of 30 A/cm^2 current density is shown in Fig. 3.14. It is very similar to a design originally suggested by Simmonds et al. [27]. The qubit Josephson junction is embedded in a rectangular two-turn loop of size $\approx$ 70x70 μm^2 to form the rf-SQUID. The size of the loop was chosen to result in a suitable β_L-parameter determined by the critical current of the smallest manufacturable junction. Loop and mutual inductances were calculated using FastHenry [82].

The microwave transmission line is patterned in coplanar configuration as a 6 μm wide central conductor separated from the ground planes by 4 μm, resulting for a Si substrate with ϵ = 11.9 in an impedance of $\approx$ 50 Ω. Ground and inner conductors are connected via a dc-break capacitively to top and bottom electrodes of the qubit junction. According to computer simulations, the size of the dc-break capacitors were designed to result in an attenuation of 20 dB at 10 GHz. Small pads of non-superconducting metal (Ti/Pd/Au) are connected to the junctions of both qubit and readout SQUID, working as traps for quasiparticles [65].

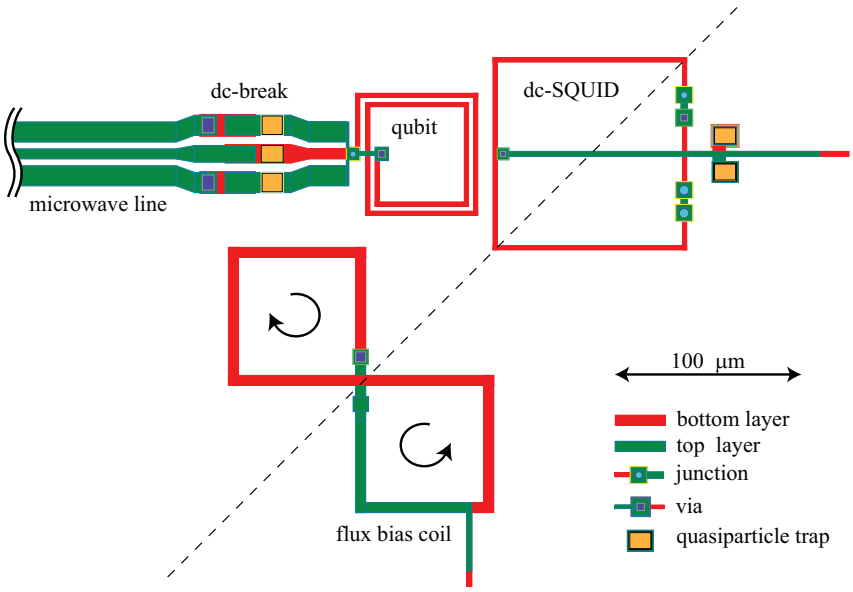

Figure 3.14: Design of sample `Hyp30` for the 30 A/cm^2 Hypres process.

The size and position of the readout dc-SQUID loop were chosen to result in a sufficiently large mutual inductance, typically about 10 pH, to allow detection of the qubit flux state in a single-shot measurement, as discussed in Sec. 3.4.2. The bias and voltage lines are connected symmetrically to the dc-SQUID loop such that an applied bias current would divide equally between the two branches if their inductances were equal. In this case, no net magnetic flux is generated in the qubit loop and the qubit remains protected from fluctuations in the dc-SQUID bias current. To keep this advantage for an asymmetric dc-SQUID, in one branch of the dc-SQUID a single junction is placed, while the other branch contains a series combination of two junctions of twice the critical current each [27]. Since the Josephson inductance Eq. (2.11) is inversely proportional to the critical current, a series combination of two junctions has the same inductance as a single smaller junction of half the critical current. Thus, as long as no bias current is applied, the SQUID remains symmetric.

The coil to apply bias flux to the qubit is designed gradiometrically in the form of an '8', so that the current will flow as indicated by the arrows in Fig. 3.14. The readout dc-SQUID is placed symmetrically with respect to this biasing coil such that the flux received from each half of the '8'-shaped coil is of same magnitude but opposite direction. This cancels changes of the dc-SQUID operation point when the qubit flux is varied.

The mutual inductance M_{qb} between qubit and flux bias coil was chosen to be $M_{\mathrm{qb}} \approx 2$ pH, such that a coil current of 1 mA results in an induced qubit flux of about one Φ_0. Although a smaller mutual inductance would increase qubit isolation, it is impractical to apply larger currents to on-chip coils due to the risk of heating the sample. While the risk of exceeding the critical current of thin superconducting films is limited by designing the flux line with a larger width, heating in the non-superconducting wire sections which are thermally anchored to the mixing chamber may be strong enough to increase the reachable base temperature by tens of milikelvin.

The dissipated power grows quadratically with the applied current. Furthermore, if contact resistances were present in the Aluminum bonds, heating would occur directly on the sample chip [60].

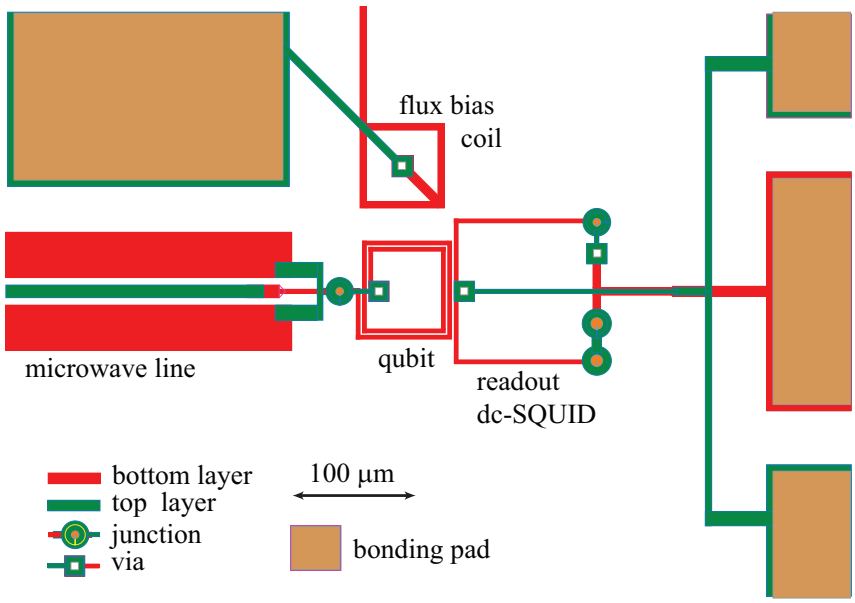

Figure 3.15: Design of sample VTT30 for the 30 A/cm^2 VTT process.

Gradiometric design

Fluctuations of the magnetic field experienced by the qubit may constitute a relevant source of decoherence. They give rise to a low-frequency fluctuation of the energy level separation, resulting in dephasing. Since the qubit loop must be made large enough to obtain the required inductance, this device is more sensitive to field fluctuations than flux qubits, in which the geometric inductance is replaced by the Josephson inductance of additional junctions [59, 11, 83]. The fluctuations can be due to vibrational motion of the sample in the background (earth) magnetic field, or can be generated by ac power lines and vacuum pumps in the vicinity of the sample.

A geometric solution to this problem is to redesign the phase qubit system with gradiometric coils. Figure 3.16 shows an improved layout, in which the rf-SQUID inductance is drawn in the shape of an '8', which can be seen as a single coil whose opposite halves are twisted by 180^o. A homogenous external field will not induce any screening currents in such a coil since the current driving force is opposite in each of its two halves which will hence cancel each other. To be able to read out the flux inside this twisted loop, the dc-SQUID (seen as the smaller '8'-shaped structure to the right of the qubit) was also designed in a gradiometric configuration. This has the additional advantage of immunity to background field fluctuations also for the readout SQUID. The wires to current-bias the dc-SQUID are connected in the middle of the '8'-shape, where bottom and top metalization layers overlap. By visualizing the direction of the bias current flow in the dc-SQUID, one can see that current fluctuations of equal amplitude in both branches will not affect the qubit. In contrast to the non-gradiometric

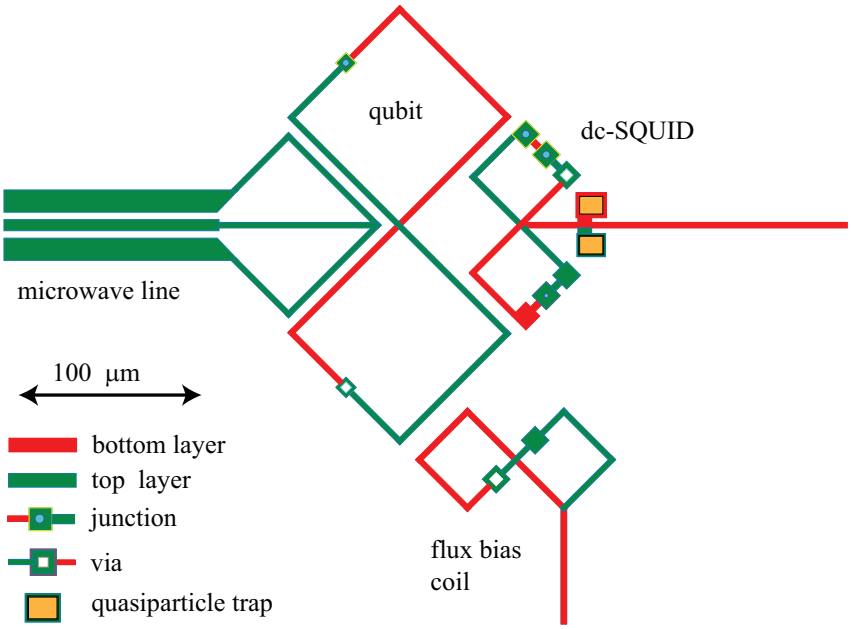

Figure 3.16: Design of sample `Hyp30Grad` for the 30 A/cm^2 Hypres process.

design, to keep the layout symmetric, the microwave line is here coupled inductively rather than capacitively to the qubit loop, while the coupling strength is reduced by about 10 dB to ≈ -30 dB (as estimated by computer simulation) to increase isolation of the qubit.

3.5.2 Sample parameters and nomenclature

Most of the experiments presented in this thesis were performed using samples fabricated at Hypres foundry in standard Nb/Al/AlO$_x$/Nb trilayer processes using silicion dioxide as a dielectric. Those are referred to as

- `Hyp100` Sample fabricated at Hypres Inc. using a current density $j_c = 100A/cm^2$. The phase qubit is designed with a single non-gradiometric loop.
- `Hyp30S` Sample fabricated at Hypres Inc. using a current density of $j_c = 30A/cm^2$ and a small qubit junction of area 11.1 μm^2. The qubit inductance is a two-turn loop in non-gradiometric configuration as shown in Fig. 3.14.
- `Hyp30L` Sample fabricated at Hypres Inc. using a current density of $j_c = 30A/cm^2$ and a larger qubit junction of area 35.5 μm^2. This sample design is otherwise equal to sample `Hyp100`.
- `Hyp30Grad` Sample fabricated at Hypres Inc. using a current density of $j_c = 30A/cm^2$, a small qubit junction of area 11.1 μm^2, and gradiometric coils as shown in Fig. 3.16.

A single measurement run was done using a sample fabricated at the VTT Research Facility using their standard Nb/Al/AlO$_x$/Nb trilayer process using silicion dioxide as a dielectric. It is referred to as

- `VTT30` Sample fabricated at VTT Research Facility using a current density $j_c = 30A/cm^2$. The design is shown in Fig. 3.15.

The loop and mutual inductances of above samples were calculated using the superconducting version of FastHenry [82] and are summarized in Table 3.1.

Sample	L (Qubit)	L_{Sq}	M_{qb}	M_{qSq}	M_{bSq}
`Hyp30S`	594 pH	420 pH	2.5 pH	24 pH	0.3 pH
`Hyp100`	190 pH	420 pH	1.5 pH	10 pH	0.2 pH
`Hyp30L`	190 pH	420 pH	1.5 pH	10 pH	0.2 pH
`Hyp30Grad`	574 pH	200 pH	1.9 pH	9 pH	0.4 pH
`VTT30`	646 pH	400 pH	5.8 pH	33 pH	0.5 pH

Table 3.1: Inductances calculated by FastHenry. Here, L is the inductance of the rf-SQUID (qubit) loop, L_{Sq} the inductance of the readout dc-SQUID, M_{qb} the mutual inductance between qubit loop on-chip biasing coil, M_{qSq} the mutual inductance between qubit and readout dc-SQUID, and M_{bSq} is the mutual inductance between on-chip biasing coil and readout dc-SQUID.

Table 3.2 summarizes the parameters of the phase qubit junctions and the calculated β_L parameters.

Sample	j_c	area	I_c	C	β_L
`Hyp30S`	30 A/cm^2	10.2 μm^2	3.1 μ A	0.42 pF	5.6
`Hyp30L`	30 A/cm^2	35.5 μm^2	10.7 μ A	1.49 pF	6.2
`Hyp100`	100 A/cm^2	10.2 μm^2	10.2 μ A	0.59 pF	5.9
`Hyp30Grad`	30 A/cm^2	10.2 μm^2	3.1 μ A	0.42 pF	5.4
`VTT30`	30 A/cm^2	7.1 μm^2	2.12 μ A	0.45 pF	4.2

Table 3.2: Parameters of the phase qubits. Here, j_c denotes critical current density and the columns area, critical current I_c and capacitance C refer to the Josephson junction in the qubit loop.

3.5.3 Al - SiN - based samples from UCSB

Reference samples of high quality were provided by Prof. John Martinis. Those have been fabricated at the University of Santa Barbara (UCSB) in a custom-developed process, using aluminum as the superconductor and silicon-nitride as a low-loss dielectric in the shunting capacitance of a small area qubit junction. The qubit design is described in detail in Ref. [84].

The qubit junction has a critical current $I_c = 1.7\ \mu A$, an area of $1\ \mu m^2$, a self-capacitance of $C = 50$ fF and is shunted by a large capacitor of C_s = 800 fF. The qubit loop is specified to have an inductance of L = 720 pH. The energy relaxation time was quoted by the UCSB group to be $T_1 \approx 110$ ns, the dephasing time measured by a Ramsey experiment was $T_2^* \approx 90$ ns and the intrinsic dephasing time as measured by a spin echo sequence is specified as $T_2 \approx 160$ ns.

This sample is referred to as `UCSB-SiN` in this thesis.

3.6 Experimental technique

3.6.1 Wiring and filtering

A prominent feature of superconducting qubits is the opportunity to control them conveniently through directly attached wires. However, strong coupling to environmental degrees of freedom via these wires and fluctuations in the biasing signals present sources of decoherence. As a particular challenge, the control circuitry must be designed to protect the qubit from noise sources and on the other hand provide the channels to control and monitor the qubit state.

A single phase qubit requires three signal channels. Two of them serve to control the qubit by transmitting magnetic flux bias and microwave currents. The third is the readout channel, which is connected to the dc-SQUID. To reduce the noise level, a standard technique is to narrow the bandwidth of the signal cables. However, this is not an option for the flux line, because it serves to both control the level of constant magnetic bias flux and to transmit dc-pulses as short as one nanosecond to allow for fast control of the Larmour frequency and state readout. The microwave line must be transparent in a wide frequency range up to the qubit resonance frequency of up to 20 GHz, but can be equipped with a dc-break acting as a high-pass filter. Therefore, for qubit control we use standard coaxial cables of a certified bandwidth of 18 GHz, but reduce the noise by coupling them very weakly to the qubit. Moreover, to increase the signal-to-noise ratio, both these lines are equipped with SMA-type attenuators [85] of 10 dB at the 1.4 K temperature stage, while the microwave line uses an additional 10 dB attenuator at the sample temperature. In earlier experiments, we noticed that a strong parasitic resonance occurring in the microwave line was due to attenuators [86] which became superconducting at temperatures below about 0.8 K.

The bias line of the readout dc-SQUID is designed to have a bandwidth limited to about 5 KHz. As shown in Fig. 3.17, several filters are used at different temperature stages. Both bias current and voltage sensing lines are equipped with commercial feedthrough filters at room temperature, followed by RC-filters at 1.4 K temperature. At a short distance to the sample chip, these lines pass through custom-made capacitively shunted copper powder filters which are designed to have an attenuation of more than 80 dB above a frequency of 1 GHz [87]. To measure the dc-SQUID voltage differentially, we connect it by a twisted pair to the room temperature amplifier. The dc-SQUID bias is sent through a single copper wire and the cryostat ground serves as the current return path. A current-divider of factor ≈ 50 is inserted in the current line at the 1.4 K temperature stage to improve the signal-to-noise ratio. Our experience showed that this configuration reduces greatly the sensitivity of the dc-SQUID measurement to noise currents flowing in ground loops which exist in the room temperature electronics as well as interference from equipment powered from the mains supply when connected to the cryostat, like oscilloscope or temperature controller.

The current-divider is realized from standard SMD resistors, which can dramatically change their resistances at low temperature. As a consequence, it is not known exactly how much current is flowing through the readout dc-SQUID during the experiment. For qubit measurements, however, this knowledge is not required, but it always remains possible to measure the current-dividing ratio by using the differential voltage lines for current-biasing and the current line for the voltage measurement.

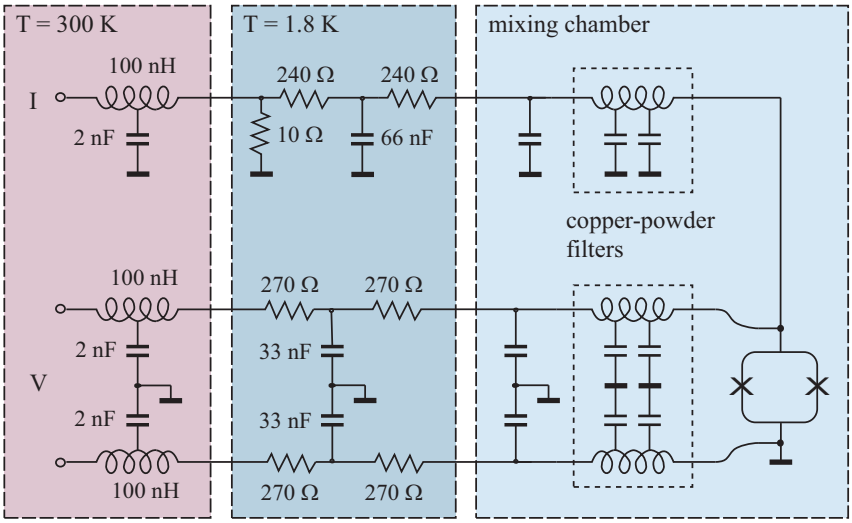

Figure 3.17: Schematic of the dc-SQUID wiring, consisting of EMI filters at room temperature, custom-made RC-filters at 1.8 K temperature, and capacitively shunted copper-powder filters at mixing chamber temperature.

3.6.2 Sample holder

Our sample housing is a copper cell of dimensions about 20 mm x 20 mm x 5 mm, in which up to four sample chips of 5x5 mm size can be glued at the same time. Measurements show that cavity resonance in the sample cell occurs around 8 GHz. Thin copper wires as well as six coaxial cables enter the cell from the bottom and are soldered to copper bonding pads surrounding the sample cell. We are using Al bonding wires of lengths up to about 5 mm to realize the connection to on-chip bonding pads, whereas those for the microwave currents are kept as short as possible and realized by three parallel wires in a coplanar configuration. To protect the qubits from magnetic field fluctuations, the inside of the sample housing is covered by a thin layer of aluminum and a cylindrical lead shield surrounds the sample cell. To avoid trapping of vortices in the superconducting shields or on-chip niobium films during the cooldown, the sample holder is surrounded by two cylinders made of cryoperm [88]. The sample holder is then thermally anchored to the mixing chamber of an Oxford Instruments Kelvinox He^3/He^4 dilution refrigerator which has a base temperature of about 15 mK. The cryostat is placed in a commercial shielded room, which is grounded but galvanically isolated from the gas handling system.

3.6.3 Electronics

The custom-made analog electronics generate the low frequency part of the qubit flux bias, serve for dc-SQUID readout and provide an isolating interface to the external computer for data acquisition. A careful grounding scheme allows to power the electronics from a transformer connected to a filtered mains supply inside the shielded room. We found no difference in the qubit performance when the electronics was driven from batteries. A mains transformer greatly extends the long-term stability of the experiment up to several weeks. Figure 3.18 provides a schematic of the experi-

mental setup, which is explained in the following.

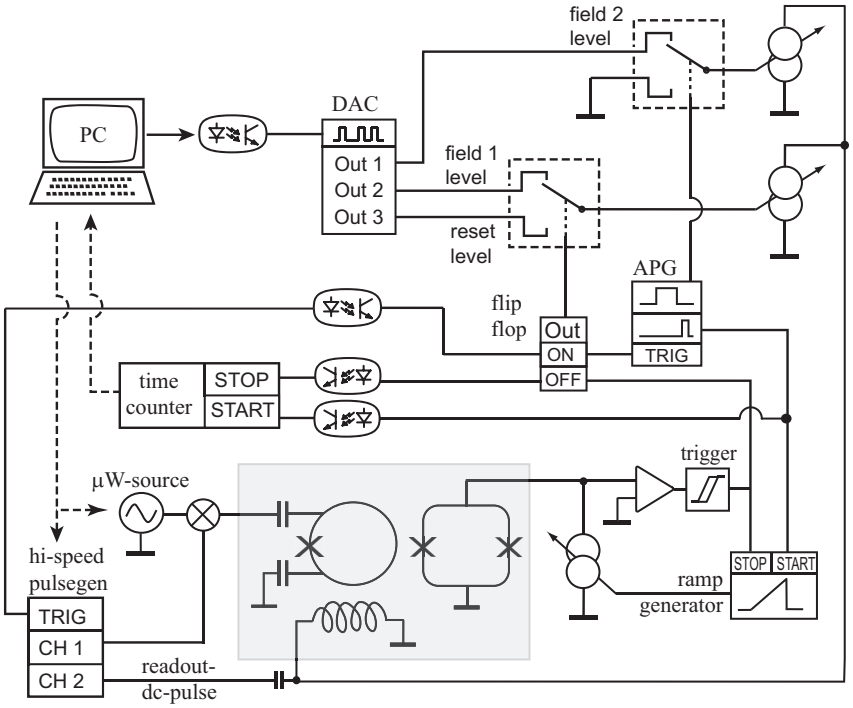

Figure 3.18: Schematic of the experimental setup. The measurement sequence is started by a trigger pulse generated by the high-speed pulse generator shown in the lower left corner.

Qubit flux bias

To operate the phase qubit, its magnetic bias flux is switched between three levels as shown in Fig. (3.7). These are a reset level, at which the qubit potential has a single minimum, the working point, at which a shallow potential well allows to operate in the two-level limit, and a freeze level at which the barrier between the two wells is large. To generate the required flux sequence, we connect two current sources in parallel to the on-chip coil. These sources are controlled by a voltage in the range of $\pm$ 10 V and generate currents in a switchable range of 10^{-2} to 10^{-7} A/V. The dc-voltages corresponding to the flux levels are delivered by a set of 16-bit precision digital-to-analog converters [89]. These are equipped with a serial interface that allows cascading of multiple converters in a daisy-chain, such that only one signal input is necessary. To avoid the presence of digital noise in the electronics during qubit operation, the DAC clock signal is generated by a custom-built logic circuit only throughout reprogramming the voltage levels. The digital data are encoded in a pulse-width modulated signal, which is created by a National Instruments output interface card in the controlling computer and sent to the DAC module via an optical fiber line featuring galvanic isolation.

As it is shown in Fig. 3.18, the desired flux level is selected by the state of two switches which connect the current source control input to different DAC voltage outputs. These are realized by an integrated circuit of analog switches [90] which are

controlled by TTL-level signals.

The measurement sequence is started when a trigger pulse changes the state of the flip-flop, switching the first current source from the reset level to the field 1 ('freeze') level. This trigger pulse is simultaneously sent to an analog pulse generator which has two independent output channels of adjustable delay and duration. Its first output channel switches the second current source from zero to the field 2 level, bringing the qubit to the working point for a time of about 200 μs, during which the microwave and dc-readout pulses are applied to the qubit. Its second output pulse triggers the dc-SQUID readout after the bias flux returned to the 'freeze' level. Once the dc-SQUID is read out, the voltage trigger resets the flip-flop, switching the current source 1 back to the reset level. Figure 3.19 shows an oscilloscope trace of the resulting qubit flux line current.

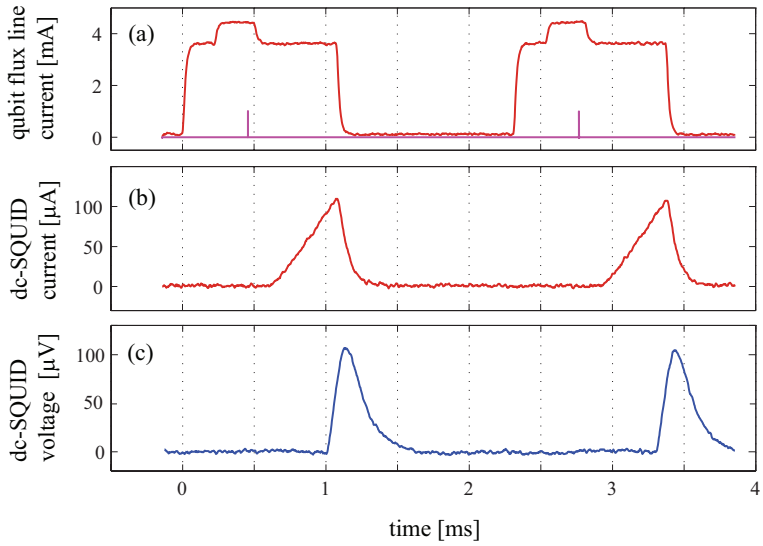

Figure 3.19: Biasing sequence. (a) Current applied to the qubit flux bias line, switching between the reset level, freeze level and working point. Additionally shown is the flux pulse for qubit readout, which is scaled by a factor of order 50 in amplitude and a factor of about 10^4 in duration to make it visible. (b) Current ramp applied to the readout dc-SQUID. (c) Voltage across the dc-SQUID.

DC-SQUID readout

The current source for biasing the readout dc-SQUID is controlled by a sawtooth generator, which produces a linearly increasing voltage once a trigger signal is sent to its start input. The voltage across the dc-SQUID is amplified by a factor of 1000 using a FET instrumentation amplifier at room temperature, whose output is fed into a trigger calibrated to generate a TTL pulse whenever the SQUID switched to its voltage state. This pulse is applied to the stop input of the ramp generator to switch the SQUID within approximately 200 μs back to the superconducting state, thus avoiding excess heating of the sample chip. Synchronously, the stop pulse is applied to the flip-flop to switch the qubit flux to the reset level. The time Δt between the pulses starting the current ramp and the voltage trigger (see Fig. 3.19) is measured by a precision time interval

counter [91], which is placed outside the shielded room and galvanically isolated from the analog electronics by means of optical fibers. With the knowledge of the current ramp rate dI/dt, the switching current $I_{\rm sw} = \frac{dI}{dt}\Delta t$ is obtained with high resolution. A detailed description of this part of the experimental setup is given in [78].

The whole pulse sequence comprising qubit operation and SQUID readout is repeated at typical rates of 200 to 400 times per second, which are limited by the time necessary to do the current-ramp measurement and subsequent idle time for cool-down, in total of about 2 ms. Higher repetition rates would be possible if the readout dc-SQUID is connected using cables of larger bandwidth, or by using a dispersive readout scheme [92, 93]. One data point for a given parameter set is usually averaged over 1000 to 5000 repetitions.

Data acquisition and evaluation

The measurement computer controls microwave and pulse generators and receives the data from the time counter via a GPIB interface. An extensive software package has been developed in Matlab [94] to program arbitrary parameter sweeps and allow for fast on-line data evaluation. It also features one-click data fitting, automatic readout pulse calibration routines and a large variety of plotting possibilities.

3.6.4 Microwave pulse modulation

To permit the observation of the state evolution of a driven qubit, the controlling microwave pulse must be shorter than the coherence time, which can be limited to just a few nanoseconds. Since commercial microwave pulse modulators have minimum pulse durations of typically about 20 ns, a prevalent method utilizes microwave mixers for modulation of a continuous wave.

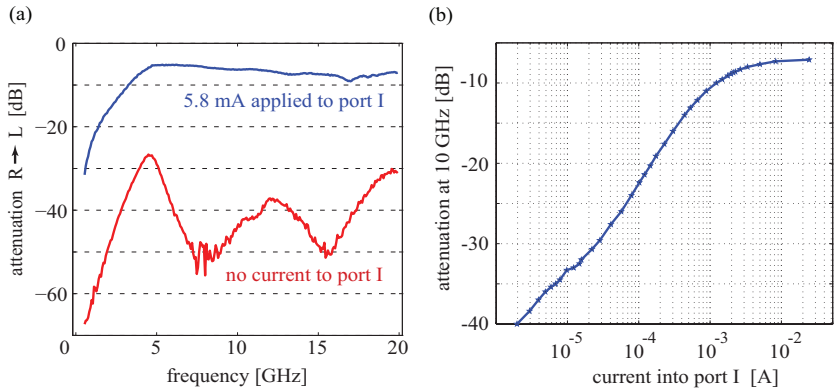

Figure 3.20: (a) Signal attenuation from port R to port L vs. microwave frequency, for applied currents to port I of zero (bottom curve) and 5.8 mA (top curve). (b) Measured attenuation at a signal frequency of 10 GHz vs. current applied to the I port. Minimal attenuation is obtained at a current of about 20 mA.

A microwave mixer is a three port device in which the two ports named L and R are coupled by Schottky diodes which are connected to the third port named I. The level of signal attenuation between the L and R ports is controllable by a dc-current applied to the I-port, which switches the diodes. Immediate response and fast signal rise times of

the order of 1 ns are advantages of this approach of pulse modulation. Fig. 3.20 shows the transmission from the L- to the R- port, both with and without applied constant DC current at the I-port, for the type of mixer [95] which we use in our experiments.

To increase the isolation, we connect two mixers of the same type in series and use a 2-way power divider [96] to split the dc-pulse between the I-ports of both mixers. As shown in the schematic by Fig. 3.21, additional low-pass filters and attenuators prevent leakage of the high frequency signal through the power divider to the output and the dc-pulse generator. The resulting isolation of this system with zero currenct applied to the I-port is larger than 60 dB.

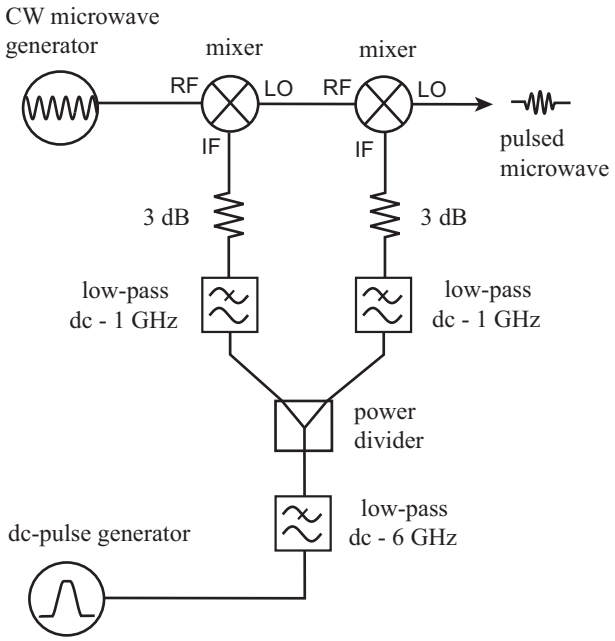

Figure 3.21: Schematic of the circuit used for microwave pulse modulation. The continuous wave (CW) signal passes through two identical mixers. The modulating dc pulse is split by a power divider (ARRA PD 0200-2) and guided through low-pass filters (Minicircuits VLF) and attenuators to the I-ports of the mixers.

Chapter 4

Experimental results

4.1 Sample characterization

Once the sample has been cooled to milikelvin temperature, the dependence $I_{\mathrm{sw}}(\Phi_{\mathrm{ext}})$ of the dc-SQUID switching current on external flux is acquired in a wide range to characterize the sample. Such a data set allows to estimate the critical currents and mutual inductances in the phase qubit system. Fig. 4.1 shows the result of an $I_{\mathrm{sw}}(\Phi_{\mathrm{ext}})$ measurement for sample `Hyp100`, displaying the positions of histogram peaks in the switching-current distribution. The horizontal scale on top of this figure has been recalculated to display the flux Φ_{sq} in the dc-SQUID loop in units of Φ_0, which is given by the periodicity of the dc-SQUID critical current modulation.

The discrete steps appearing on the $I_{\mathrm{sw}}(\Phi_{\mathrm{ext}})$ - pattern are the signature of the qubit undergoing transitions between wells at certain values of external flux. To make the hysteresis between inter-well transitions visible, the external flux was swept in two directions. As indicated in the figure, the periodicity at which these steps occur corresponds to one flux quantum in the qubit loop. Renormalizing the horizontal axis to the flux in the qubit loop Φ_{q}, as indicated by the bottom scale of Fig. 4.1, the parameter β_L can be obtained from the measured hysteresis. As shown in Fig. 4.2, the hysteresis is linear for $\beta_L > 1$ and exceeds one flux quantum above $\beta_L = 4.6$. For the shown data, the hysteresis is estimated to be $\approx (1.39 \pm 0.02)\,\Phi_0$, resulting in $\beta_L \approx 5.85 \pm 0.09$ which is in accordance to the designed values as presented in Tab. 3.2.

The measurement of the β_L value allows for a good estimation of the critical current of the qubit junction, because the inductance L of the qubit loop depends only on its geometry. Loop inductances can therefore be precisely calculated with the aid of the FastHenry program up to an estimated uncertainty of 2.5 %. Likewise, the critical current of the dc-SQUID is measured from the modulation depth $\Delta I'_{\mathrm{sq}}$ as shown in Fig. 4.1, which depends on the $\beta_{\mathrm{L,SQ}}$ - parameter [9]. From the shown data of sample `Hyp100`, we obtain $\beta_{\mathrm{L,SQ}} \approx 25 \pm 1$, which corresponds to a dc-SQUID critical current $I_{\mathrm{c,sq}} \approx (19.6 \pm 0.8)\,\mu A$.

The mutual inductance M_{qSq} between qubit and dc-SQUID is estimated near a qubit step on a linear branch of the $I_{\mathrm{sw}}(\Phi_{\mathrm{ext}})$ pattern as shown in the inset to Fig. 4.1. When the qubit switches between potential wells, the dc-SQUID switching current changes by a certain amount $\Delta I_{\mathrm{c,sq}}$. By comparing the value of external flux $\Delta\Phi'_{\mathrm{sq}}$ required to result in an equal change of $\Delta I_{\mathrm{c,sq}}$, the mutual inductance is calculated as $M_{\mathrm{qSq}} = \Delta\Phi'_{\mathrm{sq}}/\Delta I_q$. The change in circulating current ΔI_q can be calculated

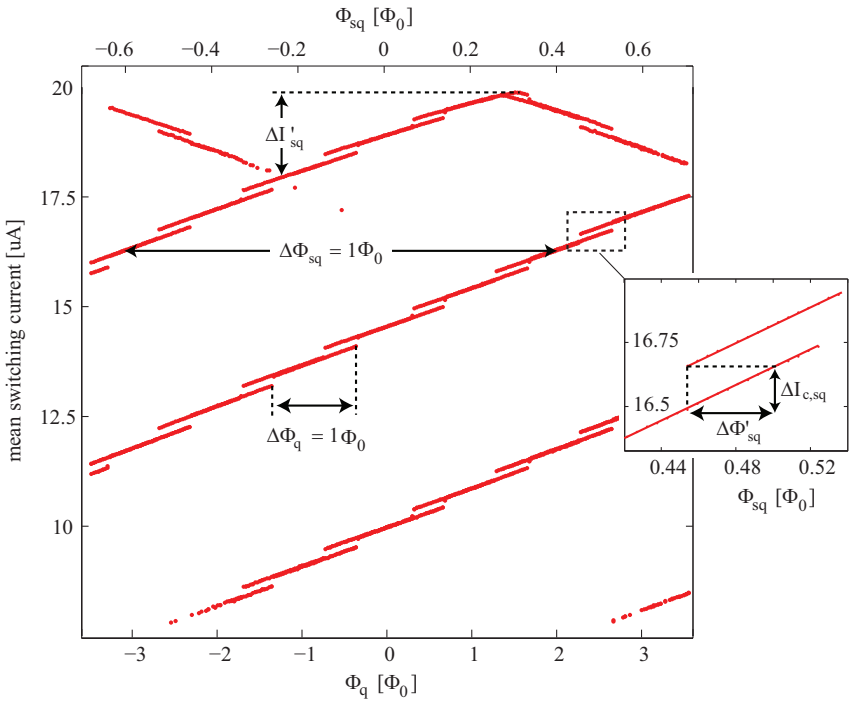

Figure 4.1: Positions of histogram peaks in the switching current distribution in dependence of the external magnetic flux for an asymmetric dc-SQUID coupled to a qubit. Sample: `Hyp100`

as discussed in Sec. 3.2 for known β_L and qubit junction critical current I_c. For the presented data of sample `Hyp100` and using $I_c = (10.1 \pm 0.4)\ \mu A$ obtained from the measured β_L parameter, $\Delta I_q = 0.77 \cdot I_c \approx (7.8 \pm 0.3)\ \mu A$. From the data in Fig. 4.1, $\Delta\Phi'_{sq} \approx (46 \pm 2)\ \mathrm{m}\Phi_0$, resulting in a mutual inductance $M_{qSq} \approx (12 \pm 0.9)$ pH which is in reasonable agreement to the calculated value of 10 pH.

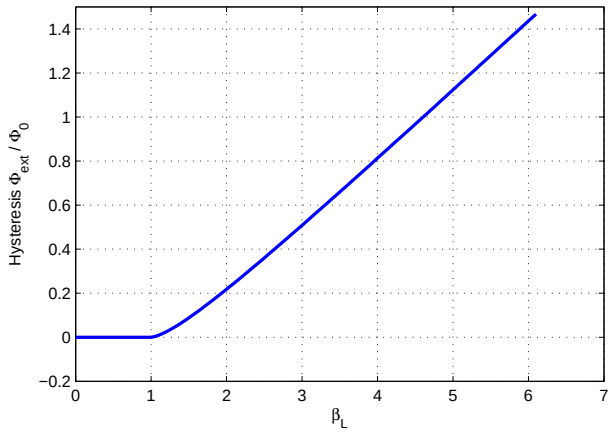

Figure 4.2: Hysteresis of the external flux at which transitions between wells occur in the rf-SQUID.

Hyp100	I_c	β_L	M_{qSq}	M_{qb}	M_{bSq}
designed	10.2 μA	5.9	10 pH	1.5 pH	0.2 pH
measured	(10.1 ± 0.4) μA	5.9 ± 0.09	(12 ± 0.9) pH	3.63 pH	0.7 pH
Hyp30S	I_c	β_L	M_{qSq}	M_{qb}	M_{bSq}
designed	3.1 μ A	5.6	24 pH	2.5 pH	0.3 pH
measured	(3.4 ± 0.1) μA	6.1 ± 0.09	(39 $\pm$ 3.1) pH	2.2 pH	1 pH

Table 4.1: Design values of sample parameters and results of measurements at a sample temperature of T = 20 mK. I_c denotes the critical current of the qubit junction, M_{qSq} the mutual inductance between qubit and readout dc-SQUID, and M_{bSq} the mutual inductance between on-chip biasing coil and readout dc-SQUID.

In Tab. 4.1, design and measured values of the parameters of samples `Hyp100` and `Hyp30S` are summarized. The higher critical current and therefore larger β_L-parameter of sample `Hyp30S` is due to a larger critical current density. In our measurements with custom-designed qubit circuits, we often found that the mutual inductances between the flux biasing coil and the qubit (M_{qb}) as well as between the coil and dc SQUID (M_{bSq}) were larger than the values reported by the FastHenry program. This is explained by a breaking of symmetry by bonding wires, which are usually located close to the qubit circuit because of densely packed chips.

4.2 Escape probability

In order to find an external flux bias suitable for qubit operation, we measured the flux dependence of the rate at which the qubit prepared in a shallow well switches towards the neighboring deeper well. For this, the current through the on-chip biasing coil is varied in time as described in Sec. 3.6.3 and shown in the inset to Fig. 4.3 (b). The coarse field component, denoted as $\Phi_{\mathrm{ext},1}$, is adjusted to switch the external qubit flux from the reset level to an intermediate ("freeze") level. The second field component of amplitude $\Phi_{\mathrm{ext},2}$ is then added to bring the qubit for a duration of typically $\Delta t = 200\,\mu$s close to the critical flux Φ_c at which the shallow potential well vanishes. During all subsequent measurements, the coarse field amplitude is kept fixed and the biasing point is changed solely by varying $\Phi_{\mathrm{ext},2}$. This has the advantage that the readout dc-SQUID is operated always at the same flux bias since the measurement of the qubit flux state is triggered after the field is switched back to the "freeze" level.

4.2.1 Theory

The probability P_{esc}that the phase escapes from the shallow to the deep well depends on the duration Δt and the escape rate Γ,

$$P_{\mathrm{esc}} = 1 - \exp\left(-\Gamma \Delta t\right). \tag{4.1}$$

Since the escape rate Γ depends exponentially on the external flux, values for P_{esc}in the range $0 < P_{\mathrm{esc}} < 1$ can only be observed in a narrow flux range at which the lifetime Γ^{-1} of the metastable state is comparable to the duration Δt of the applied flux pulse. For P_{esc}= 0.5, Eq. (4.1) gives $\Gamma \Delta t = -\log(0.5) \approx 0.7$, which corresponds to a escape rate of $\Gamma = 3.5$ kHz at a pulse duration of $\Delta t = 200\,\mu$s. Figure 4.3 (b)

shows exemplarily the dependence of the escape rate Γ on the amplitude of the field component $\Phi_{\mathrm{ext},2}$ as extracted using Eq. (4.1) from the measurement of the escape probability shown in Fig. 4.3 (a). The deviation from the exponential dependence of Γ on the amplitude of the external flux pulse, indicated by the dashed line, is due to saturation of the escape probabilty at 0 and 1, respectively.

The general form of the flux dependence of the escape probability as shown in Fig. 4.3 (a) is of letter "s" - shape which results from the double-exponential dependence of P_{esc} on the external flux Φ_{ext},

$$P_{\mathrm{esc}} \propto 1 - \exp\left[-\exp\left(-\frac{(1-\Phi_{\mathrm{ext}})^{(3/2)}}{T}\right)\Delta t\right]. \tag{4.2}$$

In this equation, the general dependence of the escape rate on the potential barrier height $\Gamma \propto \exp(-U_0/T)$ has been expressed in the cubic approximation where $U_0 \propto (1-\Phi_{\mathrm{ext}})^{(3/2)}$ (see Sec. 3.2.1).

The solid line shown in Fig. 4.3 (a) represents a fit of the data points to Eq. (4.2). This fit is used to extract two quantities which contain the most relevant information about the escape rate, namely the value of flux $\langle\Phi_{\mathrm{sw}}\rangle$at which P_{esc}= 0.5 and the width of the curve σ which is defined as the difference in external flux between P_{esc}=0.1 and P_{esc}= 0.9. In the next section, the dependence of these quantities on temperature is discussed.

4.2.2 Temperature dependence

When probing the escape probability from the metastable potential well by using a flux pulse of duration Δt, data are always taken for essentially the same range of escape rates $\Gamma \approx 1/\Delta t$. The width σ of the s-curve is determined mainly [97] by the external flux dependence of the exponential factor in Γ,

$$\sigma^{-1} \propto \frac{\partial \log \Gamma}{\partial \Phi_{\mathrm{ext}}}, \tag{4.3}$$

which is illustrated by Fig. 4.4.

The upper panel of the figure contains a plot of the quantum tunnel rate $\Gamma_Q(\Phi_{\mathrm{ext}})$ according to Eq. (2.31) and the thermal activation rate $\Gamma_{\mathrm{th}}(\Phi_{\mathrm{ext}})$ as given by Eq. (2.29), exemplarily using parameters of sample `VTT30` as stated in Tab. (3.2). The two horizontal lines indicate the rates which correspond to an escape probabilty of 0.1 and 0.9 for a field pulse duration of $\Delta t = 200\mu$s. These rates are used to calculate the escape probability curves shown in the lower panel of the figure. Evidently, at higher temperatures, the larger escape rate reduces the external flux $\langle\Phi_{\mathrm{sw}}\rangle$ at which 50 % switching probability is reached. In the thermal regime, $\Gamma_{\mathrm{th}} \propto \exp\left(-U_0/k_BT\right)$, and according to Eq. (4.3) a larger temperature T results in an increase of the s-curve's width σ. Analysis [98, 99] as well as measurements [97, 99] showed that in the thermal regime the width σ scales with temperature as $\sigma \propto T^{2/3}$.

To verify that our escape rate measurements are not influenced by noise in the experimental setup, we recorded the escape rate dependence $P_{\mathrm{esc}}(\Phi_{\mathrm{ext}})$ in a large temperature range. A plot of both width σ and $\langle\Phi_{\mathrm{sw}}\rangle$ vs. $T^{2/3}$ is shown exemplarily for sample `VTT30` in Fig. 4.5. For this sample, we observe a saturation of the step width σ below a temperature of 150 mK at a level of $\sigma \approx 8$ mΦ_0, whereas σ increases with

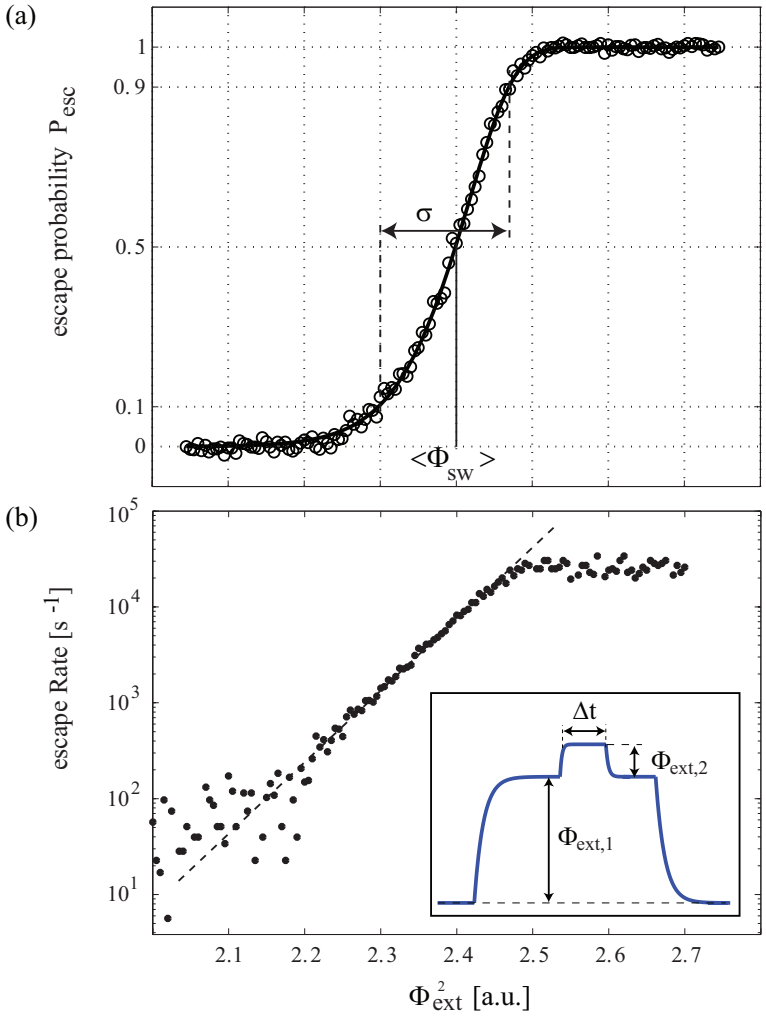

Figure 4.3: (a) Escape probability vs. the amplitude of an external flux pulse $\Phi_{\mathrm{ext},2}$ of $\Delta t = 200\mu$s duration, measured on sample VTT30. (b) Escape rate calculated from the data shown in (a). Inset: timing profile of the external flux, which is composed from two pulses of amplitudes $\Phi_{\mathrm{ext},1}$ and $\Phi_{\mathrm{ext},2}$, respectively. Both field components have a rise time of $\approx 20\mu s$.

temperature as expected proportionally to $T^{2/3}$ up to $\approx$ 22 mΦ_0 at T = 800 mK. The solid lines drawn in Fig. 4.5 are extracted from numerically calculated s-curves using the sum of thermal and quantum escape rates $\Gamma_{\mathrm{th}}(T) + \Gamma_Q$. Calculation of these lines was done by using the design values of sample VTT30 as stated in Tab. (3.2) and fitting the junction capacitance, resulting in $C = 0.2$ pF. In Fig. 4.5 (b), the data points were shifted (but not scaled) along the vertical flux axis to make them coincide with the calculated external flux at the lowest temperature. This is justified because the critical flux Φ_c is *per se* not a measurable quantity [100].

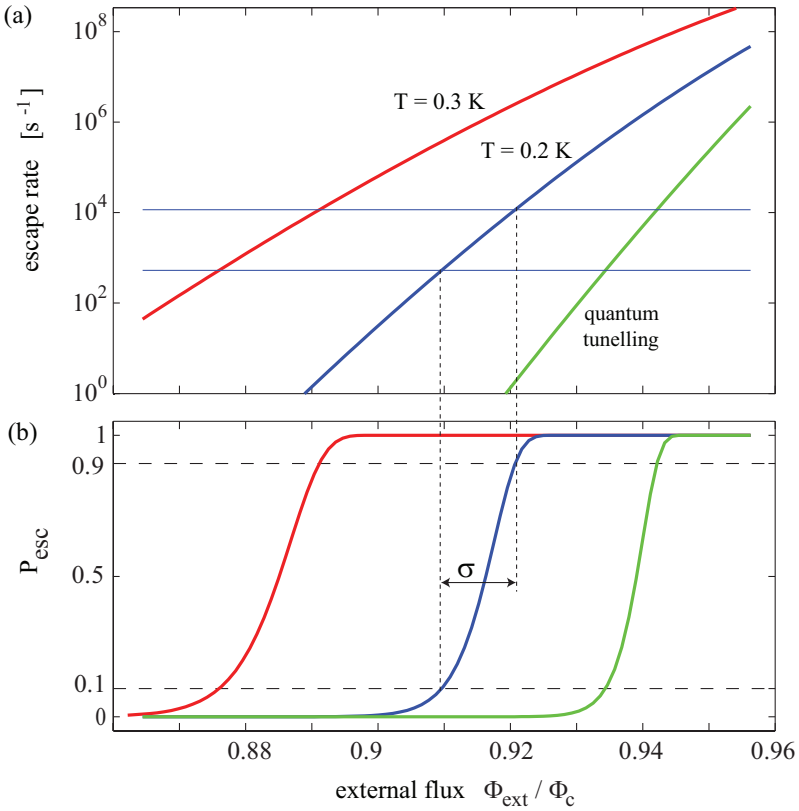

Figure 4.4: (a) Escape rates vs. external flux in the quantum regime and the thermal regime for the indicated temperatures. The horizontal lines correspond to an escape probability of 0.1 and 0.9, respectively, for a flux pulse duration of $\Delta t = 200\mu$s. (b) Escape probability vs. the amplitude of an applied flux pulse of $\Delta t = 200\mu$s duration, calculated from the rates shown in (a). Parameters correspond to sample `VTT30` as stated in Tab. (3.2).

4.2.3 Conclusions

Escape measurements from the metastable qubit potential well were used to characterize the samples. By varying the external magnetic field, the most important sample parameters could be determined. A study of the escape dynamics in dependence of the sample temperature shows the cross-over to the quantum regime and rules out the existence of extensive noise sources in our setup.

4.3 Fast qubit readout

The ability to measure the state of a quantum bit is one of the elementary requirements of quantum information processing [21]. The measurement must be conducted after logical qubit operations have been completed, and its outcome has to distinguish the logical qubit states $|0\rangle$ and $|1\rangle$ at a contrast which is very close to 1 [24]. It is therefore necessary that the readout process is accomplished faster than the coherence time T_1 at

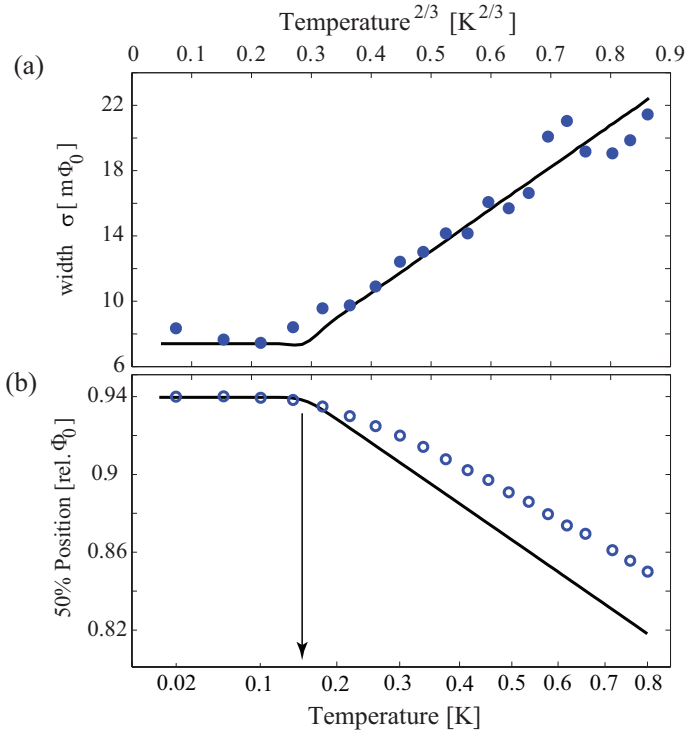

Figure 4.5: Temperature dependence of the inter-well transition, measured on sample VTT30. (a) width of the qubit step in units of the flux quantum Φ_0. (b) external flux at which the escape probability is equal to 50 %. Data points in (b) were shifted to meet the calculated position at the lowest temperature. Solid lines in both panels were calculated numerically leaving the junction capacitance as the only free fitting parameter. Indicated by the arrow is the temperature $\approx$ 150 mK above which thermal escape occurs.

which depolarization of the qubit states occurs.

4.3.1 Theory

For superconducting phase qubits, a measurement technique has been implemented which complies with above requirements [34, 35, 36]. Its principle is to shortly reduce the potential barrier of the well which contains the qubit states to allow the excited state of higher energy to tunnel into a macroscopically distinguishable state. The ground state remains in the initial well in this readout procedure.

In flux-biased phase qubits, this is accomplished by applying a dc-pulse of flux which increases the total flux in the qubit loop. Its effect is to provide an additional tilt in the qubit potential as shown in Fig. 4.6 (a), increasing the escape rate towards the neighboring potential well for all states which are contained in the shallow potential well. However, since the escape rate of the excited state is typically a factor of 10^2 - 10^3 higher than the one of the ground state, it is possible to adjust the duration and amplitude of the flux pulse such that during its application only the excited state escapes at large probability.

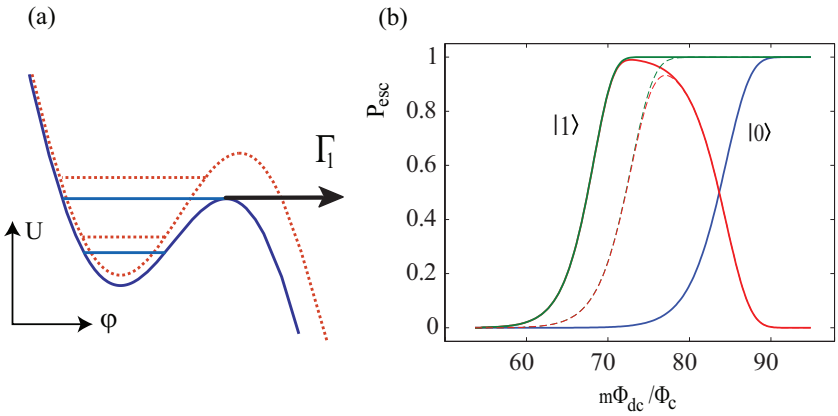

Figure 4.6: (a) Illustration of the effect of the readout dc-pulse on the qubit potential. Dashed lines show the potential well before the dc-pulse was applied, solid lines the potential during the readout pulse. (b) The calculated escape probability for a qubit prepared in states $|0\rangle$ and $|1\rangle$, read out by a gaussian readout pulse of duration W_{dc} = 2 ns and amplitude Φ_{dc}. Also shown by the red solid line is the readout contrast as the difference between the two curves. The dashed lines are calculated by taking into account energy relaxation during the readout at a T_1 - time of 1 ns, resulting in a maximum readout contrast of 0.93. Calculations were done using parameters of sample `VTT30`.

Figure 4.6 (b) illustrates the increase of the escape probability $P_{\mathrm{esc}}$with the amplitude Φ_{dc} of a readout flux pulse for the two cases when the qubit was prepared in either the ground or excited state. For these calculations, a gaussian-shaped readout dc-pulse creates the time-dependent external flux

$$\Phi_{\mathrm{ext}}(t) = \Phi_s + \Phi_{\mathrm{dc}} \cdot \exp\left[-\frac{(t-w)^2}{2\,w^2}\right]. \tag{4.4}$$

Here, Φ_s is the starting value of bias flux (at which qubit operations are done), Φ_{dc} is the amplitude of the gaussian flux pulse and w is its width which is related to the full width at half maximum W_{dc} by $w = W_{\mathrm{dc}}/(2\sqrt{2\log 2})$. The escape probability was then obtained by numerical integration of the equation

$$P_{\mathrm{esc}} = 1 - \exp\left(-\int \Gamma(t)\mathrm{d}t\right), \tag{4.5}$$

where $\Gamma(t) = p_0\Gamma_0(t) + p_1\Gamma_1(t)$ is the sum of the escape rates of the two states whose population probabilities are $p_0 = 1 - p_1$ and p_1, respectively. This rate is calculated from the WKB-result for quantum tunneling Eq. (2.31) and depends on time according to the time-varying external flux Eq. (4.4).

We define the fidelity of the readout as the difference between the obtained escape probabilities of the excited state and the ground state. Figure 4.6 (b), which was calculated using parameters of sample `VTT30` and a readout pulse duration W_{dc} = 2 ns, shows that the maximal contrast of 0.99 is very close to 100 % since the curves for the two states are well separated. The decay of the excited state due to energy relaxation

during the readout pulse was taken into account by correcting the excited state population by the factor $\exp(-t/T_1)$, where T_1 is the lifetime of state $|1\rangle$. The result of such a calculation, using $T_1 = 1$ ns, is shown by the dashed lines in Fig. 4.6 (b), reaching a maximal readout fidelity of 93%.

4.3.2 Sources of readout errors

In a real experiment, several mechanisms contribute to a reduction of the attainable readout fidelity, of which the most prominent are those related to a change of the level population during the readout process. This can be due to energy relaxation, which is avoidable by using very short and fast rising readout pulses. However, when a short pulse is to be used, its amplitude must be made large enough to reach flux values at which the excited state tunnels in a time which is comparable to the readout pulse duration. The readout hence occurs close to the critical flux where the ratio Γ_1/Γ_0 decreases as it is shown in Fig. 3.6, and therefore also the measurement fidelity decreases.

A short readout pulse may furthermore act non-adiabatically and alter the state populations when its fourier components are resonant to transitions to upper levels. Analysis [68] has shown that for typical phase qubits (having transition frequencies $\omega_{10}/2\pi \approx 10$ GHz) the probability of nonadiabatic excitation is of order 10^{-2} for linear readout pulses of 500 ps rise times but is further reduced to below 10^{-4} for gaussian-shaped pulses.

During application of the readout pulse, the qubit resonance frequency is continuously reduced and may be changed by a factor of up to 1/2. If there exists a parasitic resonator [27] below the qubit working frequency, the readout pulse may sweep the qubit through their common resonance. Given that it is coupled sufficiently strong, the coherent oscillations in the resulting four-state system may be fast enough to change the qubit state [34]. Lastly, for flux-biased phase qubits, a measurement error due to resonant tunneling, which occurs when the states in the left well and the deep right well align, has been considered [68]. While this mechanism may in principle give rise to a repopulation of the shallow well once tunneling to the deep well occurred, the strongly increased energy relaxation rate from highly excited states in the deep well renders this possibility unlikely.

4.3.3 Experimental results

Similar to above described calculations, the readout fidelity has been probed experimentally by recording the escape probability curves versus the amplitude of an applied dc-flux pulse. The result, obtained from sample `VTT30`, is shown in Fig. 4.7 for three different readout pulse widths. The excited state was populated by a resonant microwave π-pulse whose duration was 1.2 ns as found by observing coherent oscillations at the same bias parameters. The largest readout fidelity of 78.3 % was obtained for the shortest dc-pulse of 1 ns width, while for the longest pulse of duration 5 ns the fidelity decreased to 19.6 % due to significant energy relaxation during the readout. Since for this sample the time T_d, which is the half-lifetime during which the amplitude of driven coherent oscillation decays to $1/e$, is about 4 ns, decoherence occurs already during the populating microwave pulse. This can explain the significantly reduced maximum readout contrast. During a microwave pulse of duration $T_{\mu w}$, both states approach 50% population due to decoherence resulting in a finally equal rate of

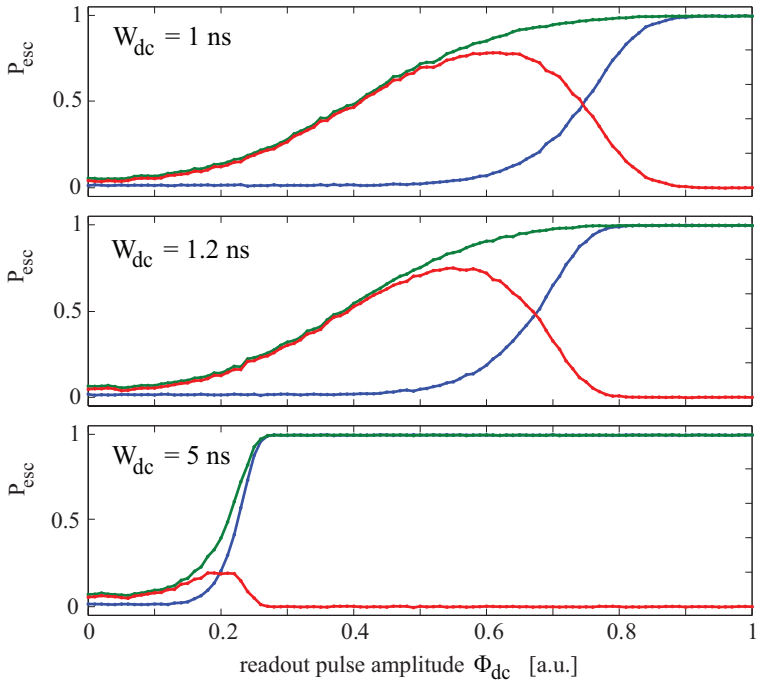

Figure 4.7: Escape probability vs. amplitude of a readout pulse, each panel corresponding to the indicated readout pulse duration. In each panel, right- and leftmost s-curves correspond to the qubit prepared in the ground and excited state, respectively. The difference between these two curves is shown additionally.

stimulated emission and absorption. This leads to a remaining probability of the qubit being in the excited state of

$$p_1 = \left[\frac{1}{2}\exp\left(-T_{\mu W}/T_d\right) + \frac{1}{2}\right]\exp[-(W_{\rm dc} + T_r)/T_1]. \tag{4.6}$$

Here, the second exponential accounts both for decay during the readout pulse of width $W_{\rm dc}$ as well as decay during the rise time T_r of the readout pulse. This equation results in an expected maximum readout contrast of 74 % assuming T_r = 500 ps, $W_{\rm dc}$ = 1 ns and T_1 = 3 ns. The slightly larger value found experimentally can be explained by the fact that even without a readout pulse corresponding to $\Phi_{\rm dc} = 0$, Fig. 4.7 shows an escape probability of about 5% which results from the microwave pulse alone. This is probably due to excitation of higher levels because of the large amplitude of the microwave pulse, which was chosen here in order to result in a short duration of the π-pulse.

For the longer readout pulse of $W_{\rm dc}$ =5 ns, Eq. 4.6 results in an expected contrast of 19 % which is also consistent with the data. We therefore conclude that energy relaxation both during qubit operation and readout can explain the reduced contrast which we observe in samples having short (<4 ns) T_1 times.

4.3.4 Thermal regime

As the ability to distinguish the phase eigenstates relies on the difference of their escape rates, it is expected that the readout contrast changes in the thermal regime where escape is dominated by activation over the potential barrier. From Kramer's rate of thermal activation,

$$\Gamma_n = \frac{\omega_0}{2\pi} \cdot \exp\left(-\frac{U_0 - n\hbar\omega_0}{k_{\mathrm{B}}T}\right), \tag{4.7}$$

where $n = 0, 1$ is the qubit state, it can be seen that the ratio Γ_1/Γ_0 scales with temperature according to

$$\frac{\Gamma_1}{\Gamma_0} = \exp\left(\frac{\hbar\omega_0}{k_{\mathrm{B}}T}\right). \tag{4.8}$$

A fast reduction of the readout contrast is therefore expected at higher temperatures. This is verified by repeating the calculation described in Sec. 4.3.1, taking into account both quantum tunneling and thermal activation. Figure 4.8 (a) shows the resulting escape probability curves in the quantum regime (T = 20 mK) and the thermal regime (T = 200 mK). The reduction of the ratio Γ_1/Γ_0 at high temperature gives rise to a reduced separation between the s-curves, while their widths are increased due to a weaker dependence of the thermal activation rate on external flux as described in Sec. 4.2.2.

The expected temperature dependence of the maximal readout contrast is plotted in Fig. 4.8 (b). Above a cross-over temperature T_R^*, at which escape during the readout pulse occurs through thermal activation rather than quantum tunneling, the readout contrast decreases steeply. For sample `UCSB-SiN`, the figure indicates $T_R^* \approx 80$ mK, while for sample `VTT30` $T_R^* \approx 150$ mK. A change of the readout pulse duration has only a small effect on the temperature dependence of the contrast, as it is shown by the dotted line in Fig. 4.8 (b), which has been calculated for parameters of sample `VTT30` using a dc-pulse duration W_{dc} = 20 ns. The readout contrast reduction at high temperatures is less for higher excited states $|n\rangle$, $n > 1$, because of the larger ratio Γ_n/Γ_0 between the escape rates from these states and that of the ground state. This is shown in Fig. 4.8 (b) for parameters of sample `VTT30` assuming that only the state $|2\rangle$, $|3\rangle$ or $|4\rangle$ is populated. It is seen that at larger n the cross-over temperature T_R^* increases, while the slope of the readout contrast dependence versus T is reduced.

We stress that this kind of loss of readout contrast can be compensated up to a certain temperature by using the procedure of fitting the escape probability histograms which was discussed in Sec. 3.4.2.

4.3.5 Automated readout calibration

In many experiments, such as *e.g.* spectroscopy, the qubit response is to be observed in dependence on the external flux. It is therefore necessary to adjust the readout pulse amplitude at each value of bias flux in order to maximize the measurement contrast. Since it is not known *a priori* which parameters of microwave pulse duration and power are necessary to bring the qubit to the excited state, a practical method [101] can be used in which it suffices to monitor the effect of the readout pulse on the qubit prepared in the ground state. The amplitude of the readout pulse is hereby varied until it leads to a small probability of escape from the ground state, typically about 5%. This assures that the same pulse would make excited states escape at a probability which is very close to 1. It can be seen in the experimental data of Fig. 4.6 that the maximum of the

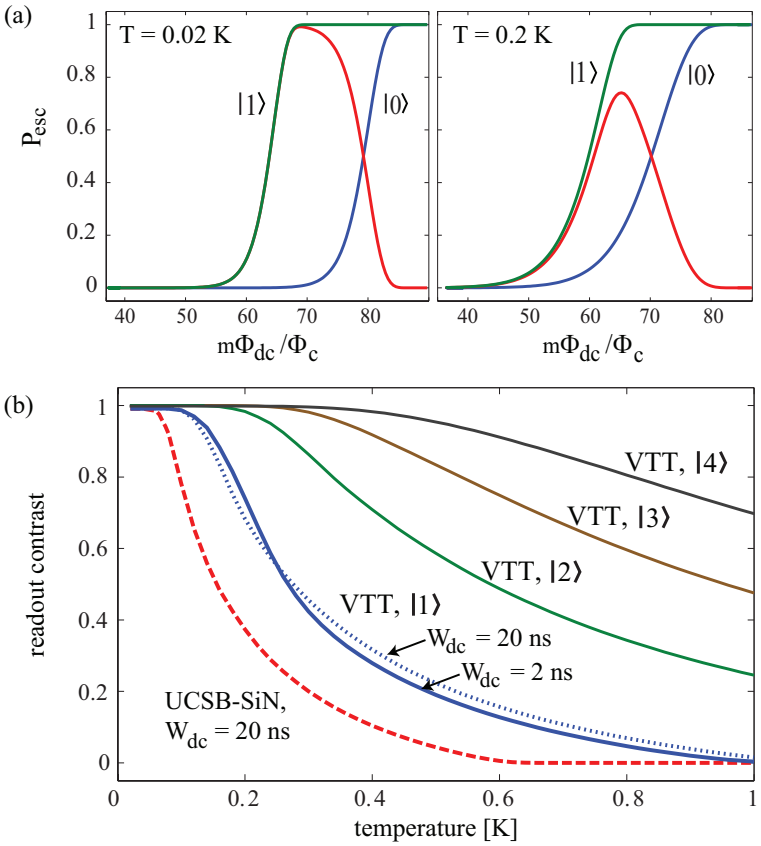

Figure 4.8: (a) Escape probability $P_{\rm esc}$ vs. readout pulse amplitude $\Phi_{\rm dc}$ at T = 20 mK (left panel) and T = 200 mK (right panel), for the qubit prepared in state $|0\rangle$ and $|1\rangle$. The readout contrast is given by the maximal difference between the two curves. (b) Maximum of the readout contrast vs. temperature. Dashed line: sample `UCSB-SiN`, readout pulse duration $W_{\rm dc}$ = 20 ns. Other lines: sample `VTT30`, readout pulse duration $W_{\rm dc}$ = 2 ns, except dotted line: $W_{\rm dc}$ = 20 ns. The Ket-vector indicates which excited state is populated by 100%.

readout contrast is indeed found at readout pulse amplitudes which result in a small escape probability from the ground state.

For automated readout calibration we implemented a function in the measurement software which finds a suitable amplitude using the binary search algorithm. It begins by measuring the reference escape probability $P_{\rm ref}$ when the readout pulse is switched off. The pulse amplitude is then varied, after each change recording the escape probability from a set of 500 samples. The algorithm stops when the guessed readout pulse amplitude results in an escape probability which is in the range of 4 to 8 % larger than $P_{\rm ref}$, which usually requires less than 10 iterations. Calibration values are then stored in a table which is used for subsequent experiments.

Figure 4.9 shows that the automatically calibrated readout pulse amplitude depends linearly on the external flux, as expected. It is therefore sufficient to run the calibration procedure at a few flux values within the range of the experiment and use the results of

a linear fit. This feature is supported by the measurement software as well.

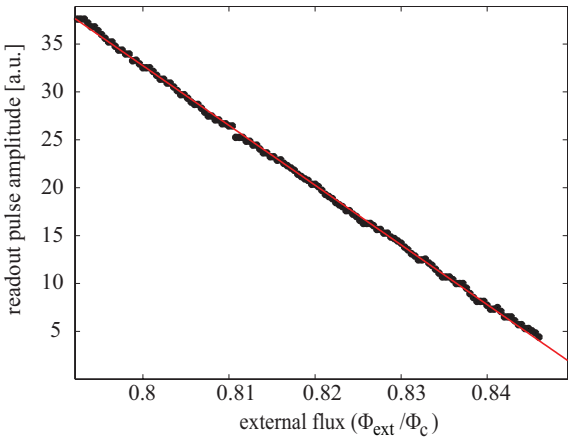

Figure 4.9: Amplitude of the readout pulse vs. external flux bias as determined by the automated calibration procedure.

4.3.6 Conclusions

Our qubit readout method is based on application of a short dc pulse of magnetic flux. A numerical and experimental study of the readout fidelity indicates that at low temperatures it is limited only by the short qubit coherence time. In contrast, at temperatures above the cross-over from quantum tunneling to thermal activation, we find that the readout fidelity is reduced due to the weaker flux dependence of the thermal escape rate. The automated calibration procedure of the readout pulse amplitude described in this section proved to be very useful for experiments in which the magnetic flux bias was varied.

4.4 Microwave spectroscopy

Microwave spectroscopy is used to find the energy difference ΔE between the ground and excited qubit states. The corresponding transition frequency $\omega_{10} = \Delta E/\hbar$ is close to the bias-dependent small oscillation frequency $\omega_0(\Phi_{\rm ext})$ shown in Fig. 3.5, and for typical phase qubit samples $\omega_0(\Phi_{\rm ext})/2\pi$ lies in the range between 6 to 20 GHz at a working flux bias of $\Phi_{\rm ext} \approx 0.95\ \Phi_c$. Application of a microwave signal of frequency $\omega_{\mu w}$ which induces a sinusoidal change of the flux in the qubit loop, or analogously an oscillating current through the qubit junction, gives rise to a population of excited qubit states when the resonance condition

$$\omega_{\mu w} \approx n\,\omega_{10} \tag{4.9}$$

is fulfilled. Here, $n \geq 1$ is an integer which accounts for the possibility that the energy difference ΔE is available to the qubit by simultaneous absorption [46] of n microwave photons, such that $\Delta E = n\hbar\omega_{\mu w}$.

4.4.1 The resonantly driven spin-$\frac{1}{2}$ system

The dynamics of the resonantly driven spin-$\frac{1}{2}$ system are described by the Bloch equations [102]

$$\frac{\mathrm{d}\langle\hat{\sigma}_x(t)\rangle}{\mathrm{d}t} = \left[\gamma\langle\hat{\sigma}(t)\rangle \times \vec{B}(t)\right]_x - \frac{\langle\hat{\sigma}_y(t)\rangle}{T_2} \tag{4.10}$$

$$\frac{\mathrm{d}\langle\hat{\sigma}_y(t)\rangle}{\mathrm{d}t} = \left[\gamma\langle\hat{\sigma}(t)\rangle \times \vec{B}(t)\right]_y - \frac{\langle\hat{\sigma}_y(t)\rangle}{T_2} \tag{4.11}$$

$$\frac{\mathrm{d}\langle\hat{\sigma}_z(t)\rangle}{\mathrm{d}t} = \left[\gamma\langle\hat{\sigma}(t)\rangle \times \vec{B}(t)\right]_z - \frac{\langle\hat{\sigma}_z(t)\rangle - \sigma_0}{T_1}, \tag{4.12}$$

which characterize the time evolution of the spin $\hat{\sigma}$ with gyromagnetic ratio γ in the time-dependent magnetic field

$$\vec{B}(t) = \{B_x(t), B_y(t), B_z\}. \tag{4.13}$$

These equations contain the energy relaxation time T_1 and the phase coherence time T_2 as well as the thermally-induced population of the excited state $\sigma_0 = \tanh(\Delta E/k_B T)$. The static longitudinal field component B_z is related to the Larmor frequency

$$\omega_{10} = \Delta E/\hbar = \gamma B_z, \tag{4.14}$$

at which the spin precesses around the z-axis. For phase qubits, the Larmor frequency is determined by the energy difference between the qubit states ΔE. The Bloch equations can be solved analytically when the time-dependent transversal field rotates at the Larmor frequency around the z-axis, so that it follows the precessing spin:

$$B_x(t) = B_t \cos(\omega_{10} t); \quad B_y(t) = B_t \sin(\omega_{10} t). \tag{4.15}$$

In a frame rotating at the Larmor frequency, this results in an effective constant transversal field. Since the phase qubit is merely a pseudo-spin, it is not possible to apply a rotating transversal field, but only a sinusoidal drive which has transversal as well as longitudinal components. However, the longitudinal component, which modulates the Larmor frequency, can be neglected in practical experiments where the Rabi frequency at which the spin rotates around the x-axis is much smaller than the precession frequency [103].

Experimentally, spectroscopy is done by using a microwave pulse of duration $\tau_{\mu w} > T_1$ to ensure that eventual coherent oscillation in the state population decay towards a constant probability of remaining in the excited state. This corresponds to a steady state $\mathrm{d}\hat{\sigma}/\mathrm{d}t = 0$. Immediately after the microwave pulse, the readout dc-pulse is applied to probe the qubit state, hereby realizing a measurement of the z-component $\langle\hat{\sigma}_z\rangle$. A measurement of the escape probability in dependence of microwave frequency or external flux bias then displays a resonance curve which has the form of a Lorentzian given by [104]

$$\langle\hat{\sigma}_z\rangle = \left[1 - \frac{\omega_R^2\, T_1 T_2}{1 + \left(\frac{\omega_{10} - \omega_{\mu w}}{T_2}\right)^2 + \omega_R^2\, T_1 T_2}\right] \sigma_0. \tag{4.16}$$

Here, $\omega_R \propto J_n(\alpha)$ is the Rabi frequency, which is for a n-photon process proportional to the nth order Bessel function of the first kind $J_n(\alpha)$ of the normalized amplitude of

the driving field $\alpha \propto B_x$ for $B_y = 0$. [105]. For the one-photon process, ω_R scales linearly with α as long as $\omega_R \ll \omega_{10}$.

From Eq. (4.16) it follows that the full width at half maximum of the resonance curve is

$$\sigma = \frac{2}{T_2}\sqrt{1 + \omega_R^2 T_1 T_2} \tag{4.17}$$

and the amplitude of the resonance is

$$A = \frac{\omega_R^2 T_1 T_2}{1 + \omega_R^2 T_1 T_2}\sigma_0. \tag{4.18}$$

4.4.2 Spectroscopy at small drive amplitude

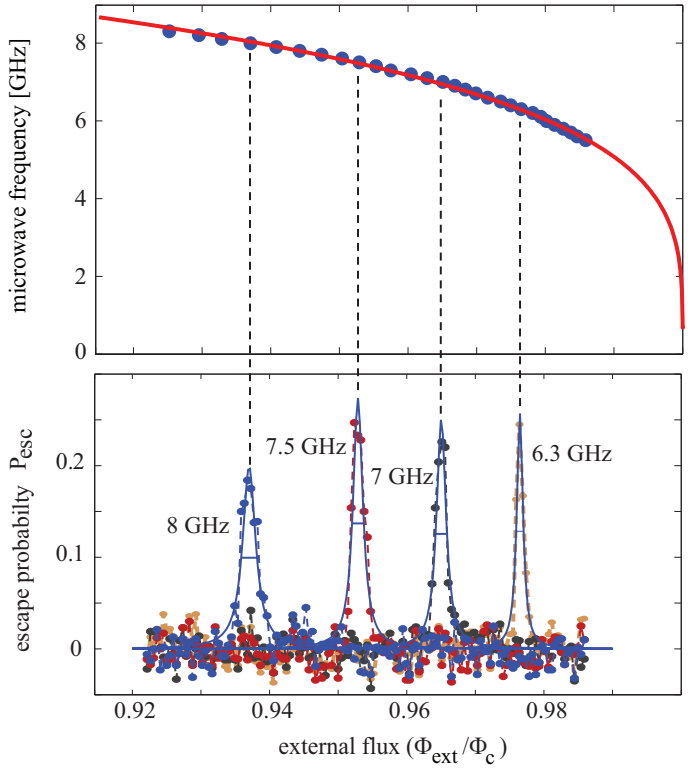

Figure 4.10: Top panel: The applied microwave frequency plotted vs. the value of external flux at which the resonance peak is found. Solid line is a fit to the small oscillation frequency $\omega_0/2\pi$, resulting in $I_c = 1.65\mu A$ and $C = 832$ fF for a fixed inductance L = 720 pH. Bottom panel: Resonance peaks in the escape probability, obtained by varying the external flux. Solid lines are fits to Lorentz curves. The shown resonance curves have Q-factors of ≈ 100, which are limited by the drive amplitude. Data has been taken using sample `UCSB-SiN`.

Resonance curves obtained from sample `UCSB-SiN` are plotted in the bottom panel of Fig. 4.10, using a microwave pulse of 200 ns duration at the frequencies indicated in the figure. The value of external flux at which these resonances are located

depends on the chosen microwave frequency as shown in the top panel of Fig. 4.10. Here, the solid line is obtained from a fit of the resonance positions to a numerical calculation of the small oscillation frequency ω_0, using the junction critical current and capacitance as free parameters. However, this data does not allow to determine the sample parameters exactly, since the externally applied flux is known only up to an additive constant. This third fitting parameter is therefore required which is not independent of the qubit parameters.

4.4.3 Parasitic resonances the setup

Our attainable resolution of microwave spectroscopy is limited by the parasitic resonances in our experimental setup. These give rise to a frequency modulation of the microwave power that couples to the qubit, hereby changing the amplitude and width of the resonance peak. Figure 4.11 shows exemplarily the result of spectroscopy performed on sample `HYP100` using a fixed microwave power. The strong oscillation in the width of the trace is due to harmonics of a parasitic resonance of about 300 MHz. At frequencies where much power couples to the qubit, we observe a second peak which is due to a higher-order transition as described in the next section. In principle, it is possible to avoid this effect by adjusting the microwave power at each frequency to the frequency-dependent coupling coefficient between source and qubit, which can be evaluated from the amplitude of the resonance peak using Eq. (4.18).

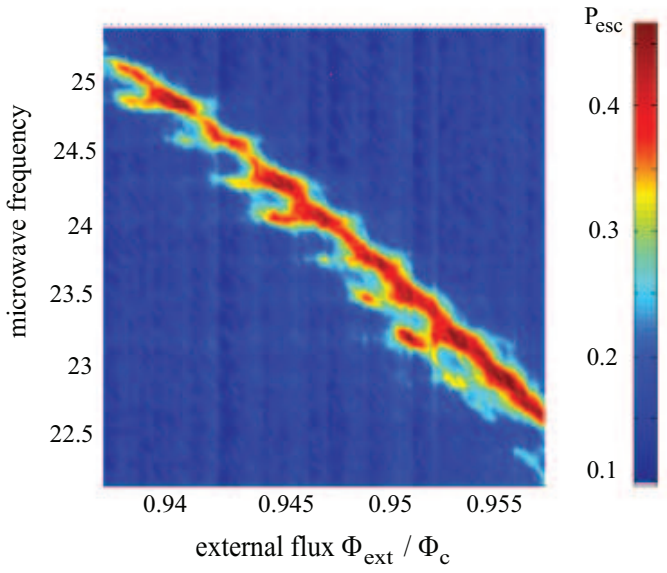

Figure 4.11: Spectroscopy on sample `Hyp100`.

Parasitic resonances can also be visualized *in situ* by measuring the frequency dependence of the power that is required to induce an off-resonant escape from a very shallow potential well as shown in Fig. 4.12. This data was acquired without using a readout pulse by biasing the qubit close the critical flux where the escape probability from the ground state was about 20%. An automated program varied the microwave

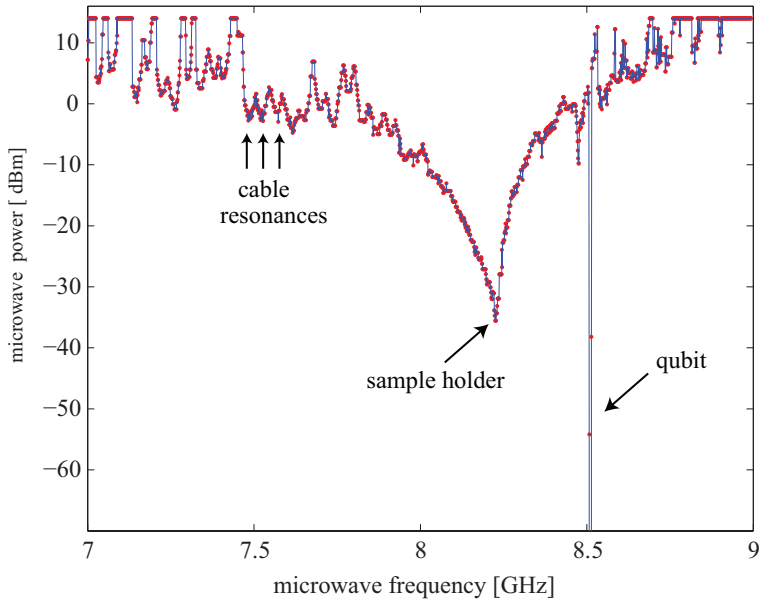

Figure 4.12: Microwave power necessary to increase the escape probability by 10%, plotted vs. microwave frequency. The used sample was `UCSB-SiN`.

power until P_{esc} increased by 10 - 15%. The cavity resonance of the sample housing is clearly seen as a broad resonance located at about 8.2 GHz. The sharp peak at 8.5 GHz frequency is the qubit resonance of sample `UCSB-SiN`. The frequency of the dominating parasitic resonance is about 300 MHz, similar to the spectroscopic data shown in Fig. 4.11 which was measured on a different sample and using a different microwave line. Therefore it is likely that in our experimental setup the parasitic resonances originated in reflections from the attenuators installed at the 1K-pot, which probably change their impedances at low temperatures.

4.4.4 Higher-order transitions

For large microwave powers, multi-photon transitions to higher energy levels can be observed in phase qubits of low anharmonicity or when they are operated in deep potential wells. These transitions occur as additional resonance peaks located at lower microwave frequencies, or, analogously, at lower flux bias values for a fixed microwave frequency, because the energy difference between two neighboring levels decreases with increasing energy.

Figure 4.13 shows the result of spectroscopy performed on sample `Hyp100`, using a relatively large microwave power. Due to a parasitic resonance in the setup, the power coupling to the qubit increased at higher frequencies. The plot of the escape probability vs. external flux reveals two resonance peaks at 22.20 GHz (at which less microwave power is coupled to the qubit), and up to 5 peaks at 22.92 GHz (accordingly, larger power coupled to the qubit). Resonance curves for these two cases are shown in the lower panel of Fig. 4.13. For the displayed range of external flux bias, the qubit potential well contained 8 to 5 energy levels. The positions of all appearing resonance

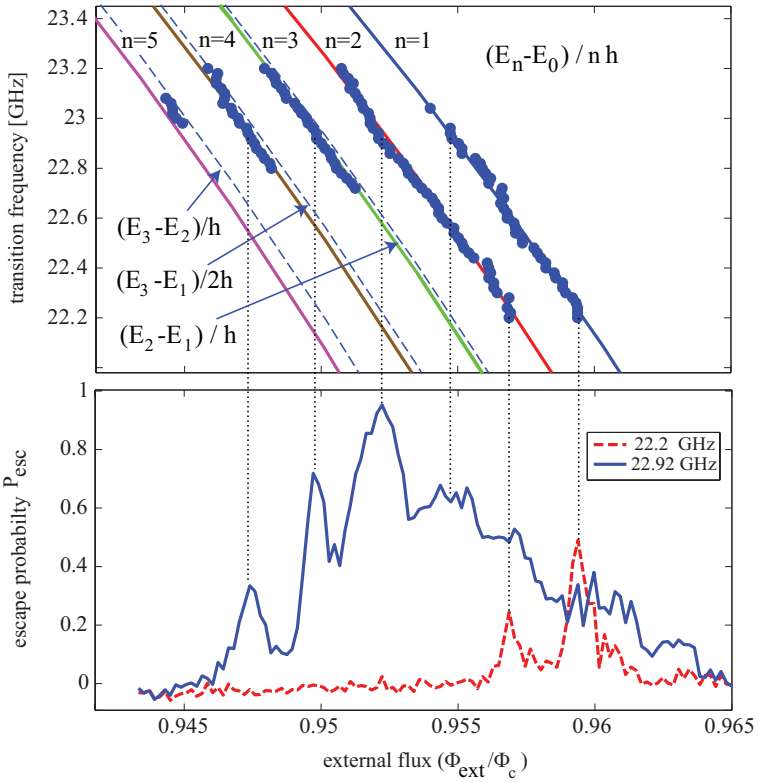

Figure 4.13: High-power spectroscopy using sample `HYP100`. Top panel: Position of resonance peaks vs. external flux and chosen microwave frequency. Solid lines: Numerically calculated resonance frequencies corresponding to the n-photon $|0\rangle \rightarrow |n\rangle$ transition as indicated in the top of the figure. Dashed lines: calculated resonance frequencies of the higher order transition as indicated by the arrows. Bottom panel: Escape probability vs. external flux showing the resonance curves obtained at 22.2 GHz and 22.92 GHz, respectively. Vertical dotted lines connect the peaks to the corresponding points in the upper panel.

peaks are plotted vs. the applied microwave frequency in the upper panel of Fig. 4.13. Solid lines were calculated from a numerical solution of the stationary Schrödinger equation and indicate the transition frequencies between the nth excited level and the ground state, $(E_n - E_0)/(n\,h)$, where the factor n takes into account the multi-photon process. For example, the resonance closest to the one-photon $|0\rangle \rightarrow |1\rangle$ transition for n = 1 is the two-photon transition from the ground state to the second excited state $|0\rangle \rightarrow |2\rangle$ for n = 2. We fitted only the data points corresponding to the $|0\rangle \rightarrow |1\rangle$ transition and find that all other resonances lie closely on the expected higher order transition frequencies. Fitted sample parameters were $I_c = 10.0\mu$ A and capacitance $C = 47.2$pF.

Alternatively, the additional resonance peaks may originate in transitions between state $|1\rangle$ and higher states. This is possible because at high microwave power the broadened $|0\rangle \rightarrow |1\rangle$ resonance peak overlaps with the resonance of the $|1\rangle \rightarrow |2\rangle$ transi-

tion. The resonance frequencies of this kind of transitions are plotted in Fig. 4.13 by dashed lines, showing that they are practically indistinguishable from the multi-photon transitions discussed above. A numerical solution of the time-dependent Schrödinger equation for the resonantly driven rf-SQUID [106] results in resonance curves which are very similar to the experimental data shown in Fig. 4.13. These calculations show cascaded transitions $|0\rangle \rightarrow |1\rangle \rightarrow |2\rangle$ in qubits of comparable damping strength.

In principle, it is possible to measure the individual population probability of higher levels by varying the amplitude of the readout pulse [36]. For a given readout pulse amplitude, escape occurs from all levels higher than a certain energy threshold. If each level has some probability of being populated, an increasing readout pulse amplitude should hence result in an escape probability which increases in steps due to subsequent emptying of individual energy levels.

4.4.5 Resonance peak amplitude

The number of photons n which are absorbed in a transition can be determined by a measurement of the resonance peak amplitude in dependence of applied microwave power [104]. The resonance amplitude is proportional to microwave power and, according to Eq. (4.18), increases quadratically with the Rabi frequency $\omega_R \propto J_n(c\, I_{\mu w})$, where $I_{\mu w}$ is the microwave amplitude as generated by the source and c is the coupling factor between source and qubit. By fitting the extracted resonance amplitudes to Eq. (4.18) using Bessel functions of the first kind $J_n(c\, I_{\mu w})$ for the Rabi frequency, it is possible to determine the number of photons n as well as the coupling strength c.

The result of such a procedure is shown in Fig. 4.14 (a), which displays the amplitude of the first two resonance peaks observed at a frequency of 22.7 GHz in dependence of microwave power. Data points are obtained by fitting the measured escape probability to the sum of two Lorentz curves as shown in Fig. 4.14 (b). The solid lines are fits to Eq. (4.18), using the Bessel functions $J_n(c\, I_{\mu w})$ for n = 1 and 2, respectively, with the coupling factor c and the coherence time T_1 as free parameters. An excellent agreement between the experimental data and the expected peak amplitudes is found which confirms the expected two-photon transition creating the second resonance peak. The energy relaxation time T_1 resulting from the fits was a factor of about 3 larger for the two-photon process than for the one-photon process, which is in agreement with more detailed calculations [104] and can be explained by the smaller probability of emitting two photons simultaneously.

The microwave amplitude $I_{\mu w}$ was calculated from the microwave power $P_{\mu w}$ [dBm] provided by the generator according to $I_{\mu w} \equiv 10^{P_{\mu w}/20}$. The coupling factor c resulting from the fits was $c = 0.002$ for both n = 1 and 2. This corresponds to a total attenuation between the microwave generator and the qubit of -54 dB, which is in agreement with the expected losses in the coaxial cables (-15 dB), the installed attenuators (-20 dB) and the on-chip dc-break (-20 dB). The horizontal axes of Fig. 4.14 have been scaled by the factor c to display the microwave power and amplitude received by qubit.

4.4.6 Inhomogeneous broadening

The probabilistic nature of quantum mechanics demands that measurements on qubits must be averaged over an ensemble of identical experiments to obtain statistical in-

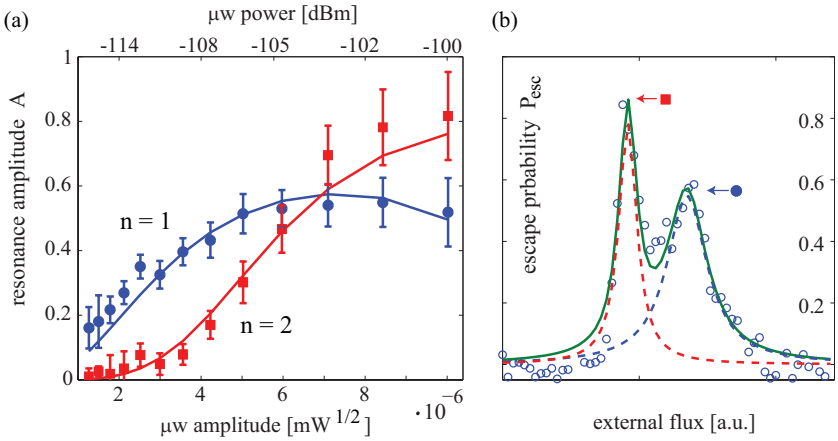

Figure 4.14: (a) Amplitudes of the one-photon (points) and two-photon (squares) resonance peaks in dependence of the microwave power (top axes) and microwave amplitude (bottom axes) as received by the qubit. Solid lines are fits to Bessel functions of the first kind J_n. (b) Microwave resonance showing two peaks. Solid line is a fit to the sum of the two Lorentz curves shown by dashed lines.

formation. Fluctuations in the experimental parameters which occur during the time required to complete the repetitions give rise to dephasing. This effect can be distinguished from other decoherence mechanisms by spectroscopic measurements. For example, slow changes in the external flux lead to variations in the energy separation of the qubit states and therefore change the Larmor frequency. The resulting shift of the resonance peak gives rise to an increase of the measured peak width, an effect which is called *inhomogeneous broadening*. This term originates in NMR experiments, where an inhomogeneous transversal magnetic field leads to different Larmor frequencies in spatially separated nuclei, which constitute the individual qubits.

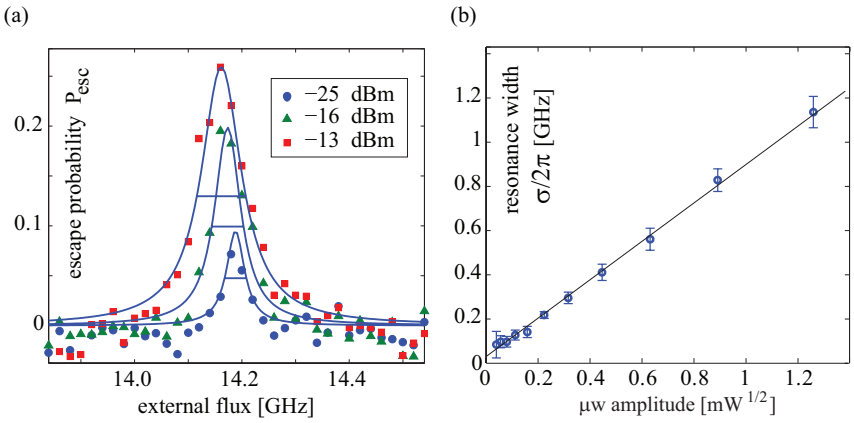

Figure 4.15: (a) Resonance curves and fit to Lorentzians for an applied microwave power as indicated in the legend. (b) Full width at half maximum $\sigma/2\pi$ vs. microwave amplitude. The line is a linear fit which intersects the vertical scale at 30 MHz. Sample `Hyp30S`.

The rate of dephasing due to inhomogeneous broadening is captured by introducing the coherence time T_2', which adds with the intrinsic dephasing rate $1/T_2$ to the effective dephasing rate

$$\frac{1}{T_2^*} = \frac{1}{T_2'} + \frac{1}{T_2}. \tag{4.19}$$

When the field inhomogeneity has a Lorentzian distribution[1], the resonance peak width given in Eq. (4.17) is corrected for inhomogeneous broadening by a constant factor and reads [108]

$$\sigma = \frac{2}{T_2'} + \frac{2}{T_2}\sqrt{1 + \omega_R^2\, T_1\, T_2}, \tag{4.20}$$

In the strong driving limit where $\omega_R^2 T_1 T_2 \gg 1$, the resonance width increases via the Rabi frequency ω_R linearly with the amplitude of the microwave field. When the resonance width is plotted versus microwave amplitude, the value $2/T_2'$ can be extracted from a linear extrapolation to zero microwave amplitude.

Figure 4.15 shows the result of such an experiment obtained using sample `Hyp30S`. The extrapolated zero-power resonance width of $\Delta f = \sigma/2\pi = 30$ MHz corresponds to a T_2'-time of

$$T_2' = \frac{2}{2\pi\, \Delta f} = \frac{1}{30\,\mathrm{MHz}} = 10.6\,\mathrm{ns}.$$

The experimental results obtained using the other investigated samples are summarized in Tab. 4.2. However, the given data suffers from a large uncertainty because at larger drive amplitudes the resonance width increases beyond the linear behavior due to appearing transitions to higher levels. Furthermore, we observe that the measured T_2' varies with the external flux bias, as it is shown in Tab. 4.2 for sample `VTT30`.

Sample	T_2'	Δf	$\omega_{\mu w}/2\pi$
`Hyp30S`	10.6 ns	30 MHz	14.2 GHz
`Hyp30L`	2.7 ns	120 MHz	11.65 GHz
`Hyp100`	3.2 ns	100 MHz	22.6 GHz
`VTT30`	16 ns	20 MHz	13.2 GHz
`VTT30`	25 ns	13 MHz	13.1 GHz

Table 4.2: Decoherence times by inhomogeneous broadening T_2', calculated from the measured resonance width Δf extrapolated to zero microwave amplitude. The rightmost column states the used resonant microwave frequency.

4.4.7 Resonance peak position

For large amplitudes of the driving field, the position of the resonance peak deviates from the result obtained using the Bloch equations. In a spin-$\frac{1}{2}$-system without dissipation, it is expected that the one-photon resonance occurs at the drive frequency $\omega_{\mu w} = \omega_{10} - \Delta\omega$, where $\Delta\omega$ is the so-called Bloch-Siegert shift given by [109]

$$\Delta\omega = \frac{1}{16}\left(\frac{\omega_R}{\omega_{10}}\right)^2 \omega_{10}. \tag{4.21}$$

[1] Whether the field inhomogeneity has a Gaussian or Lorentzian shape depends on the cause of the fluctuation [103, 107]. Coupling to a bath of non-saturated two-level fluctuators is expected to result in a Gaussian line shape, while $1/f$ noise originating from saturated two-level systems shows a Lorentzian distribution.

For not too strong driving $\omega_R < \omega_{10}$, *i.e.* $\omega_R \propto I_{\mu w}$, this equation predicts a small correction to the peak position which scales quadratically in the drive amplitude $I_{\mu w}$. In practical experiments where typically $\omega_R/\omega_{10} < 0.1$ and $\omega_{10}/2\pi \approx 10$ GHz, the Bloch-Siegert shift is about 6 MHz and thus is expected to be negligible.

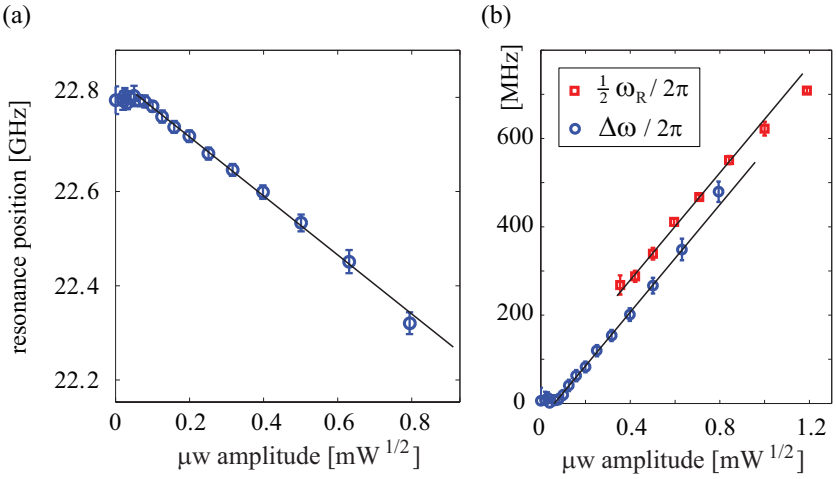

Figure 4.16: (a) Position of resonance, normalized to the applied microwave frequency which was 22.8 GHz. (b) Drive amplitude dependence of resonance shift $\Delta\omega$ (circles) and half the Rabi frequency ω_R (squares), both observed at the same microwave frequency. The two lines have equal slope. Sample `Hyp100`.

Experimentally, we observe a much stronger influence of the drive amplitude on the peak position as it is shown in Fig. 4.16 (a). The resonance peak is shifted linearly with the drive amplitude towards lower frequencies. This is expected for dissipative systems [103], for which the shift of the resonance frequency can be estimated as

$$\Delta\omega = \frac{\omega_R}{2}. \tag{4.22}$$

This equation is verified by Fig. 4.16 (b), showing the microwave amplitude dependence of both the resonance shift $\Delta\omega$ and half the Rabi frequency $\omega_R/2$. The Rabi frequency was obtained by fitting a damped sinusoidal to the coherent oscillations observed in the time domain as described in Sec. 4.6. Both kind of data points were obtained at a microwave frequency of 22.8 GHz in the same measurement run. The resonance shift shows the same dependence on drive amplitude as half the Rabi frequency, and moreover differs absolutely by only a small amount (about 70 MHz for the shown data), hereby clearly confirming Eq. (4.22).

4.4.8 Conclusions

Extensive measurements were done using microwave spectroscopy. In the strong driving regime, we observed transitions to higher levels in the qubit potential well, which are characterized by additional resonance peaks. A detailed analysis of the resonance peak amplitudes allowed us to identify the transition mechanism underlying a certain peak as a two-photon process. We observed a shift of the resonance peak position in the strong driving limit toward lower frequencies. The magnitude of this shift, which

depends linearly on microwave amplitude, was found to follow closely the frequency of coherent oscillation observed at identical bias parameters. By observing the drive amplitude dependence of the resonance peak width, we measured the qubit coherence time T_2' due to low frequency fluctuations. These experiments indicate that low frequency noise which gives rise to inhomogeneous resonance broadening is not a limiting factor in our measurements.

4.5 Excited state life time T_1

4.5.1 Experimental method

The standard way to measure the life time of the excited state is to first bring the qubit from the ground to the excited state by using a so-called π-pulse, which is a resonant microwave pulse of duration on half of the Rabi period. Measuring the qubit state with increasing time delay after the end of the microwave pulse results in an exponentially decreasing excited state, whose decay constant is the sought-after T_1 time.

Determination of the π-pulse duration requires prior observation of Rabi oscillation. It should be noted that it is also possible to perform this experiment by an incoherent microwave pulse of long duration which results in about 50% probability of excited state population. In our experiments, we did not find any difference in the measured T_1 times obtained by either a coherent or incoherent excitation.

4.5.2 Experimental results

Figure 4.17 (a) shows the result of a measurement using a resonant π-pulse, obtained on sample `Hyp30L`. The solid line is an exponential fit, resulting in a T_1 time of 5.8 ns. This is a typical value for all our phase qubit designs that were fabricated by Hypres Inc. In contrast, by using the custom-made sample `UCSB-SiN`, we measured excited state life times of $T_1 \approx 115$ ns, as it is shown in Fig. 4.17 (b). A summary of our measurements for all discussed samples in given in table 4.3. We estimate an uncertainty of about $\pm$ 1 - 2 ns in the measured T_1 times for the samples based on SiO_x due to the strong dependence of coherence properties on the biasing point and the limited number of performed experiments. The stated numbers are largest reproducible values.

Sample	T_1	$\omega_{\mu w}/2\pi$
`Hyp30S`	5.5 ns	14.1 GHz
`Hyp30L`	5.8 ns	11.65 GHz
`Hyp100`	3.2 ns	22.7 GHz
`VTT30`	2.4 ns	16.5 GHz
`HypGradio`	6.5 ns	13.1 GHz
`UCSB-SiN`	115 ns	7.4 GHz

Table 4.3: Measured excited state life times T_1. The rightmost column states the used resonant microwave frequency.

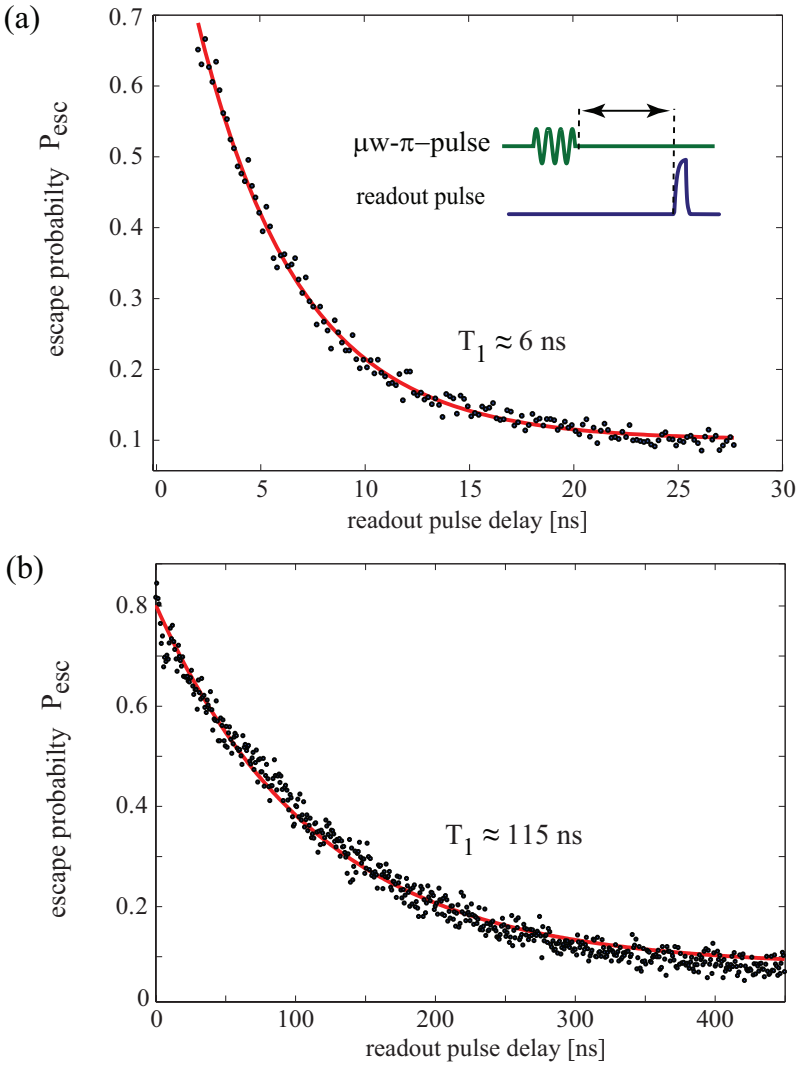

Figure 4.17: Escape probability vs. the delay between populating microwave pulse and readout pulse as indicated in the inset. Solid lines are fits to an exponential function. (a) Sample `Hyp30L`, 2000 counts per data point. (b) Sample `UCSB-SiN`, 1000 counts per data point.

4.5.3 Conclusions

The qubit coherence time T_1 due to energy relaxation was measured by directly observing the exponentially decaying population of the excited state in the time domain. The samples fabricated in standard technology using SiO_2 as a dielectric for insulation between metallic layers showed rather short T_1 times of below 8 ns. In a sample which was fabricated in a custom process featuring a smaller qubit junction and SiN_x as dielectric, we measured T_1 times of about 100 ns. This confirms that the fidelity of conventionally fabricated phase qubits is limited by a large density of two-level fluctuators, which reside in oxide dielectrics and couple to the qubit.

4.6 Rabi oscillation

Application of a transverse resonant field induces Rabi oscillations between the two qubit states as long as the system remains coherent. These oscillations are essential to quantum computation because by this mechanism single qubit operations are realized. The first experimental observations of Rabi oscillation in superconducting qubits were therefore important milestones in the study of macroscopic quantum coherence and opened the door to the implementation of a solid-state quantum computer.

4.6.1 Theory

Solving the Bloch equations (4.12) for the expectation value of the spin's z-component $\langle\vec{\sigma}_z\rangle$ when driven by the rotating transversal field $\vec{B}_t(t)$ results in [108, 103]

$$\langle\vec{\sigma}_z\rangle = e^{-t/\tau_1}\left(\frac{\sin(\omega_R\, t)}{\omega_R\,\tau_2} + \cos(\omega_R\, t)\right). \tag{4.23}$$

This describes an oscillation which is damped with a time constant τ_1 given by the mean of the coherence times T_1 and T_2,

$$\frac{2}{\tau_1} = \frac{1}{T_1} + \frac{1}{T_2}. \tag{4.24}$$

The life time of Rabi oscillation is therefore expected to be a combination of the coherence times T_1 and T_2. The oscillation frequency ω_R, corrected for damping, reads

$$\omega_R = \sqrt{\gamma^2 B_t^2 - 1/(\tau_2^2)}, \tag{4.25}$$

where

$$\frac{2}{\tau_2} = \frac{1}{T_2} - \frac{1}{T_1}. \tag{4.26}$$

For the phase qubit, the transversal driving field is realized by adding a microwave component $I_{\mu w}\,\sin(\omega_{\mu w}t + \varphi)$ to the current flowing through the junction. In terms of the microwave amplitude $I_{\mu w}$ and neglecting damping, the Rabi frequency translates into [110]

$$\omega_R = \gamma B_t = \frac{I_{\mu w}}{2}\sqrt{\frac{1}{2\hbar\,\omega_{10} C}}, \tag{4.27}$$

where C is the junction capacitance and ω_{10} the qubit's Larmor frequency. An actual implementation of a phase qubit is expected to differ in many aspects from a spin as described by the Bloch equations. Superseding the limitation to non-rotating driving fields is the existence of higher excited states, which at stronger driving can take part in coherent oscillations. On the other hand, nonlinear and eventually even coherent coupling to parts of the environment can lead to distinctive features in qubit state evolution.

Excitation to higher energy levels

The phase qubit must be operated in a potential well which is made deep enough to avoid escape of the excited state by tunneling. This has the consequence that the potential well always contains more than one excited state. Population of the second excited state by a microwave which is tuned in resonance to the $|0\rangle \rightarrow |1\rangle$ transition

frequency ω_{10} is expected [111, 112] when the Rabi frequency ω_R is comparable to the anharmonicity $\Delta\omega = \omega_{10} - \omega_{21}$. As it was shown in Fig. 3.5, the anharmonicity of the potential well for typical phase qubits depends on the flux bias and is a few hundred MHz. Short coherence times in turn dictate observation of Rabi oscillation on a time scale of 10 ns which requires Rabi frequencies of order 100 MHz. For low-quality phase qubits, this leaves only a small parameter range in which transitions to higher excited states can be avoided. However, theory [113] has shown that a small off-resonant transition probability to higher states can be corrected by suitably shaped pulse sequences for sufficiently long coherence times.

Taking into account the possibility of leakage to the second excited qubit state, the population of state $|1\rangle$ up to terms quadratical in ω_R reads [112]

$$p_1(t) = \left[1 - \frac{3}{2}\left(\frac{\omega_R}{2\,\Delta\omega}\right)^2\right]^2 \cdot \sin^2\left\{\omega_R\left[1 - \left(\frac{\omega_R}{2\,\Delta\omega}\right)^2\right]\,t\right\}. \tag{4.28}$$

This equation shows that the oscillation frequency Ω_R scales with the amplitude of the microwave field as

$$\Omega_R \propto I_{\mu w}\left(1 - \kappa\, I_{\mu w}^2\right), \tag{4.29}$$

describing a quadratic bend-off of the observed frequency Ω_R from the linear dependence on drive amplitude. Equation (4.28) predicts a reduced amplitude of the first excited state population due to leakage into higher states. However, this leakage does not necessarily reduce the amplitude of observed oscillations, as higher excited states may take part in coherent oscillations. Modelling a strongly driven phase qubit operated in the multi-level limit [36] predicted coherent oscillations of nearly 100% amplitude between the ground and mostly the 4th and 5th excited states. Since the state readout via a dc-flux pulse is usually calibrated to merely distinguish the ground state from higher states, the amplitude reduction predicted by Eq. (4.28) may not observed in our experiments.

Coupling to parasitic fluctuators

The observation of anti-crossings in the microwave spectrum [27] has demonstrated that contemporary phase qubits suffer from coherent coupling to parasitic two-level fluctuators (TLF) which exist in the dielectrics used in junction fabrication. A TLF has the two eigenstates $|g\rangle$ and $|e\rangle$ and is characterized by its resonance frequency ω_{TLF} and the coupling strength to the qubit J. In resonance at $\delta = \omega_{\mathrm{TLF}} - \omega_{10} = 0$, the eigenstates of the coupled system are linear combinations of the states $|1g\rangle$ and $|0e\rangle$ [34]. This gives rise to an oscillatory redistribution of the energy between qubit and parasitic resonator, where the frequency of this oscillation is given by the coupling strength J which also determines the size of the anti-crossing given by J/h .
In a continuously driven qubit-fluctuator system at $\delta = 0$, the probability to measure the first excited qubit state is calculated [112] as

$$p_1(t) \approxeq \frac{1}{2}\left[1 - \cos\left(\frac{J\,t}{2\hbar}\right)\cos\left(\frac{B_t t}{\hbar}\right)\right], \tag{4.30}$$

where fluctuator damping is neglected and the typical experimental case $|B_t|/J \gg 1$ is assumed. This equation describes an oscillation at the Rabi frequency $\omega_R = B_t/\hbar$

which is modulated by the beating frequency $J/2\hbar$.
It has been shown experimentally [34] that the damping rate γ of a TLF can be comparable to the qubit decoherence rates. If, in contrast, the parasitic resonators are highly damped and $\gamma \gg J$, the excited state population will show damped oscillations at a single frequency,

$$p_1(t) \approxeq \frac{1}{2}\left[1 - e^{-J^2 t/4\hbar\gamma}\cos\left(\frac{B_t t}{\hbar}\right)\right]. \tag{4.31}$$

4.6.2 Measurement of Rabi oscillation

To observe Rabi oscillation at a chosen microwave frequency, the value of external flux bias at which the qubit resonance peak is located is first determined by microwave spectroscopy. The duration $\tau_{\mu w}$ of the resonant microwave pulse is then varied, hereby adjusting the delay of the calibrated readout pulse such that it always occurs at the end of the microwave pulse. The probability to measure the qubit in the excited state then displays the damped oscillations $p_1(t)$ described by Eq. (4.28), where the time scale t is given by the microwave pulse duration.

To assure that the readout pulse occurs at the end of the microwave pulse, it may be necessary to compensate a difference in the signal propagation delay between the coaxial cables used to send microwave and readout pulses. This is done by sending a nanosecond-long resonant microwave pulse of large amplitude and recording the escape probability in dependence of the readout pulse delay relative to the microwave pulse. A rapid increase in $P_{\rm esc}$ then indicates the readout delay at which both pulses arrive at the qubit simultaneously.

4.6.3 Results of SiO_x - based samples

In our experiments on commercially fabricated phase qubits made of niobium as the superconductor and SiO_x as dielectric, we measured the longest coherence times with samples of low current density and small qubit junctions. Figure 4.18 shows the best Rabi oscillations which we obtained from such kind of chip using sample `Hyp30S` at a driving frequency of $\omega_{\mu w}/2\pi$ = 13.3 GHz[2]. Changing the microwave power, we observe the expected increase of the oscillation frequency.

To extract the oscillation frequency ω_R, full amplitude A_R and decay time T_d, we fit the data to the function

$$P_{\rm esc} = P_0 + (A_R/2)\,{\rm e}^{-t/T_d}\left[\sin(\omega_R\, t + \varphi_R) + A_b\right], \tag{4.32}$$

as it is shown by the solid line in Fig. 4.18. Here, P_0 is a constant offset, φ_R an oscillation phase, and A_b is an offset which depends on the current oscillation amplitude. This last fitting parameter is required because at large microwave power we observe that $P_{\rm esc}$ tends to saturate exponentially after a mean time which is about T_d at a high value, as it can be seen in the top panel of Fig. 4.18. We may explain this behavior by incoherent population of higher excited states.

[2]The indicated microwave power or amplitude always corresponds to the signal level at the generator output. If not mentioned explicitly, data has been taken at a temperature of about 20 mK.

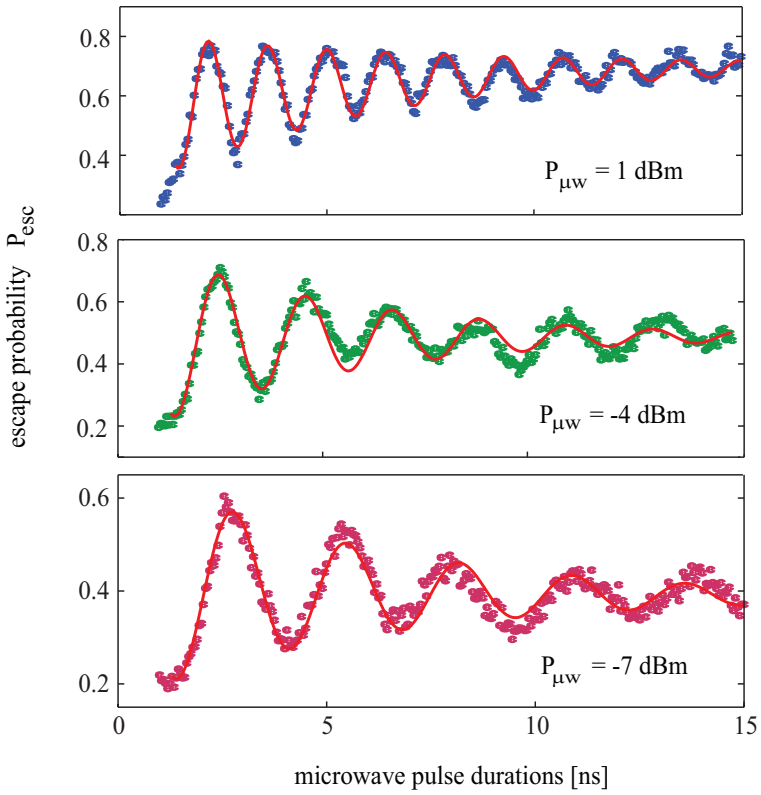

Figure 4.18: Coherent oscillations measured on sample `Hyp30S` using a drive frequency of $\omega_{\mu w}/2\pi$ = 13.3 GHz and indicated power. The solid line is a fit to Eq. (4.32). Note the different vertical scale of each panel.

Driving strength dependence

In Fig. 4.19, we plot the oscillation amplitude A_R and decay time T_d vs. microwave amplitude exemplarily for sample `Hyp30S` driven at $\omega_{\mu w}/2\pi$ = 13.3 GHz. For all measured samples, these parameters showed a similar driving amplitude dependence. At weak driving, we observe a small oscillation amplitude, which may be explained by relaxation occurring at a rate comparable to the Rabi frequency. For stronger driving, the oscillation amplitude increases quickly and reaches a maximum which is probably characterized by the condition that the Rabi frequency is larger than the energy relaxation rate but not so large that transitions to higher excited states are dominant. Further increasing the driving strength then leads to decrescent amplitude due to the mentioned population of higher excited states. The largest obtained oscillation amplitude is about 0.6, which is comparable to that of the other samples of this type as it is summarized in Table 4.4.

The decay time of the observed oscillations shows a similar dependence on microwave amplitude, approaching smoothly a maximal value of $T_d \approx 6$ ns at intermediate driving strength.

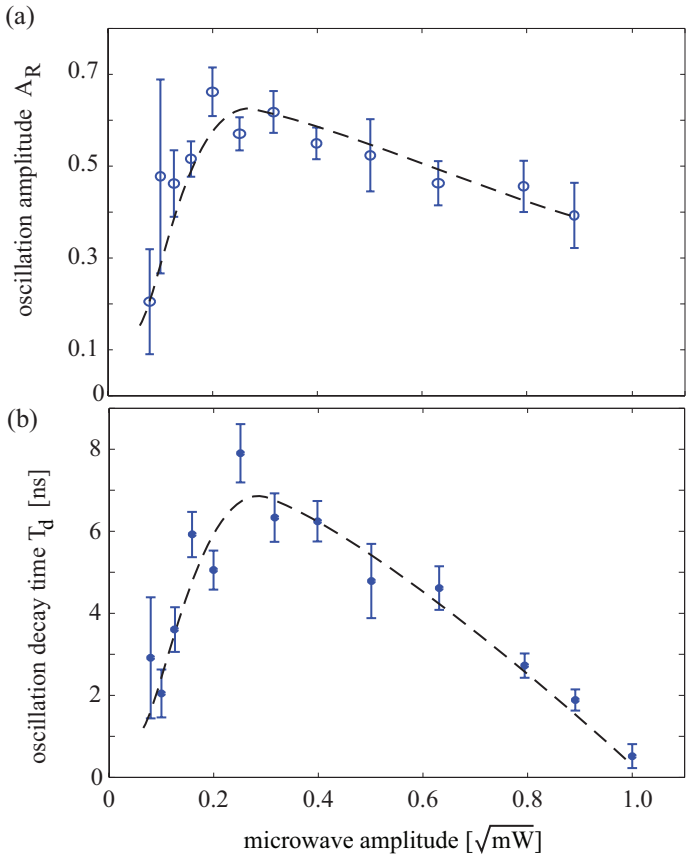

Figure 4.19: Dependence of the coherent oscillation amplitude (top panel) and decay time (bottom panel) on microwave amplitude, measured on sample `Hyp30S` using a drive frequency of $\omega_{\mu w}/2\pi$ = 13.3 GHz. Error bars indicate the confidence interval resulting from the fitting procedure as described in the text. Dashed lines are guides to the eye.

Sample	T_d	A_R	$\omega_{\mu w}/2\pi$	$\omega_R/2\pi$
`Hyp30S`	6.0 ns	0.6	12.7 - 14.2 GHz	50 - 900 MHz
`Hyp30L`	2.8 ns	0.5	11.65	400 - 1300 MHz
`Hyp100`	2.5 ns	0.65	22.6	180 - 550 MHz
`VTT30`	4.0 ns	0.65	12.8 - 17.3	200 - 1800 MHz

Table 4.4: Results of coherent oscillation measurements in SiO_x - based samples. Oscillation decay time T_d and amplitude A_R are largest obtainable values, averaged over measurements using resonant microwaves in the indicated frequency range $\omega_{\mu w}$ and oscillation frequencies ω_R. The stated oscillation amplitude A_R is not scaled by the measurement contrast.

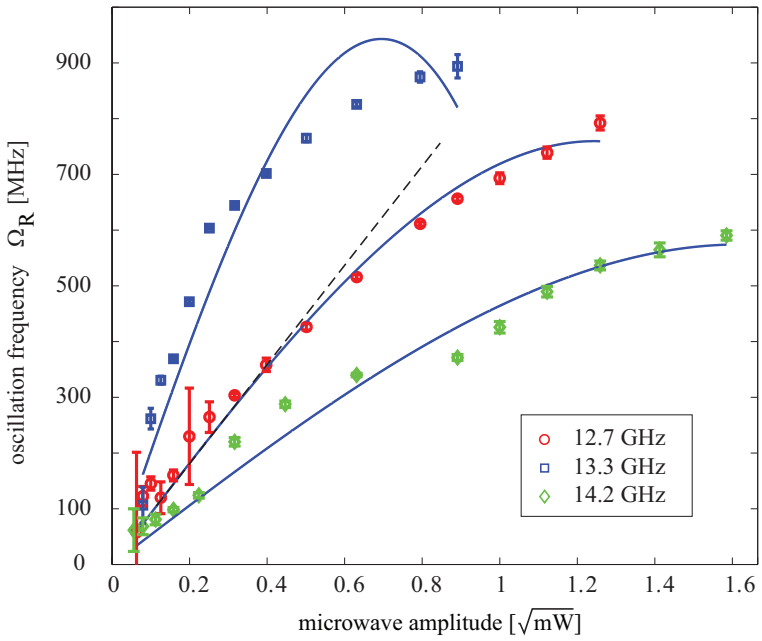

Figure 4.20: Oscillation frequency vs. microwave amplitude, measured using sample `Hyp30S`. For each curve, the external flux bias has been adjusted to result in resonance at the applied microwave frequency indicated in the legend. Solid lines are fits to theory for a three-level system.

The dependence of the oscillation frequency vs. the amplitude of the microwave drive, measured on sample `Hyp30S`, is shown in Fig. 4.20. The three different curves were obtained using the indicated microwave frequencies, whereas the external flux bias has been adjusted to maximize the oscillation visibility at each frequency. We observe a linear dependence of the oscillation frequency only for small microwave amplitudes. The differing slope of the curves at low microwave amplitude can be attributed to the different power coupling to the qubit when the microwave frequency is changed. We observe a deviation from the linear dependence at larger drive amplitudes as it is expected when higher excited states get involved. The solid lines in the figure are best fits to the equation

$$\Omega_R = c\, I_{\mu w} \left(1 - \kappa \left(c\, I_{\mu w}\right)^2\right), \tag{4.33}$$

which is the theoretically expected dependence for a three-level system as given by Eq. (4.29) modified by adding the free coupling parameter c. We were not able to obtain a systematic and close correlation between the three-level theory and the data sets at all studied flux biases. Beneath the existence of more than three levels in the potential well, the qubit dynamics are expected to be severely influenced by coupling to parasitic two-level fluctuators. A change of the external flux bias may therefore result in a strongly modified qubit environment.

External flux dependence

In section 2.3.1 it was discussed how a detuning between the qubit Larmor frequency and the driving microwave affects Rabi oscillaion. Equation (2.58) predicts that with

increasing detuning $\Delta = |\omega_{10} - \omega_{\mu w}|$ the oscillation frequency is increased, $\Omega_R = \sqrt{{\omega_R}^2 + \Delta^2}$, while its amplitude is reduced by a factor ${\omega_R}^2/({\omega_R}^2\Delta^2)$. Plotting the escape probability color coded vs. microwave pulse duration and detuning should therefore result in the so-called *chevron*-pattern.

In our current experimental setup, due to the frequency-dependent coupling to the qubit caused by transmission line resonances, it is more convenient to create a detuning by changing the external flux bias rather than the microwave frequency .

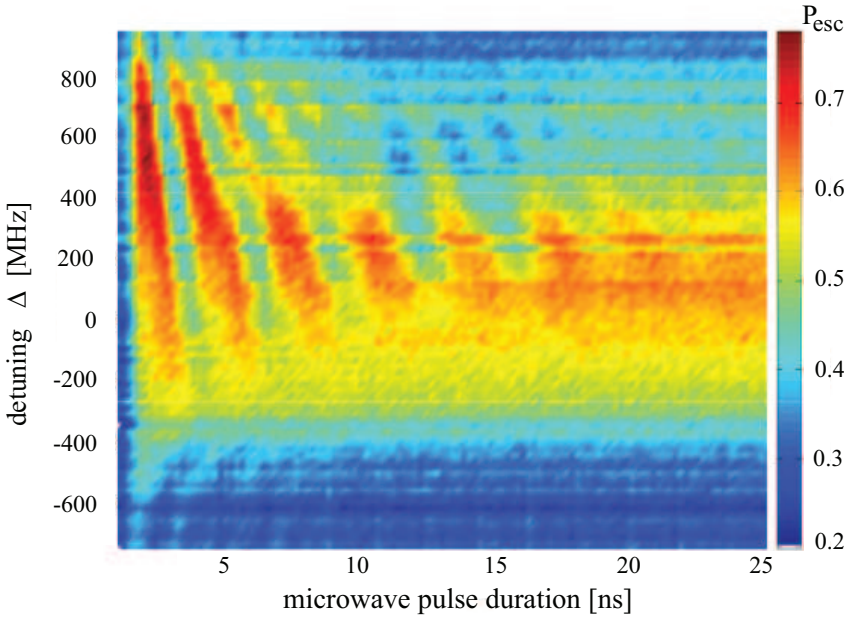

Figure 4.21: Escape probability P_{esc} (color-coded) in dependence of microwave pulse duration and detuning Δ. The detuning was realized by changing the external flux bias at a fixed microwave frequency of 14.2 GHz. Sample `Hyp30S`.

In Fig. 4.21, a chevron pattern measured using sample `Hyp30S` driven at $\omega_{\mu w}/2\pi = 14.2$ GHz is presented. The vertical axis shows the detuning $\Delta = (\omega_{\mu w} - \omega_{10})/2\pi$, which was converted from the applied external flux to frequency using spectroscopy data. A linear approximation of the resonance frequency dependence on external flux in vicinity of the resonance at 14.2 GHz was hereby used.

The figure shows the expected increase of the oscillation frequency when the external flux is increased starting from the exact resonance, which results in a flatter potential well having a smaller transition frequency $\omega_{10} < \omega_{\mu w}$. However, close to the exact resonance the oscillation visibility rapidly decreases. We speculate that this is due to an increased probability of inducing transitions to higher levels when the microwave frequency is slightly smaller than the $|0\rangle \rightarrow |1\rangle$ transition frequency, as in this case the microwave is closer to the $|1\rangle \rightarrow |2\rangle$ resonance. Further reducing the detuning for $\Delta <$ -500 MHz, the system remains in the ground state, as the microwave frequency is below the $|0\rangle \rightarrow |1\rangle$ transition frequency.

For the same data, Fig. (4.22) contains plots of the characteristic oscillation parameters obtained by fitting the datasets at each detuning. The oscillation frequency plotted in Fig. 4.22 (a) follows closely the theoretical detuning dependence as expected

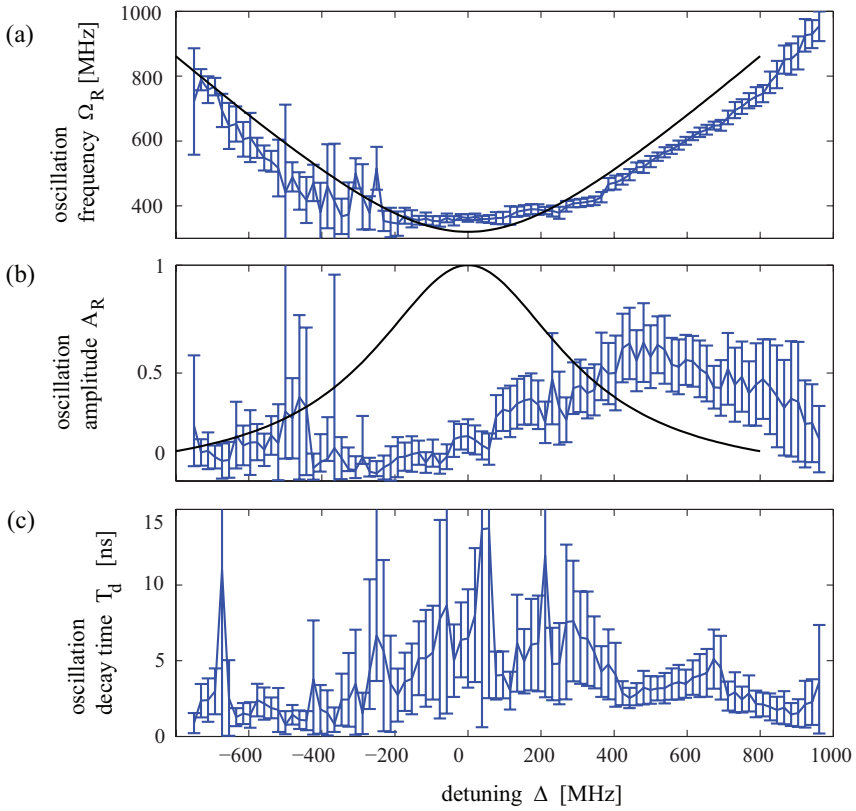

Figure 4.22: External flux dependence of the coherent oscillation in sample `Hyp30S`. (a) oscillation frequency, (b) oscillation amplitude, (c) oscillation decay time.

from Eq. (2.58), which is plotted by the solid line without free parameters. The small deviation can be explained by the only approximated flux to frequency conversion. The oscillation amplitude A_R shown in Fig. 4.22 (b), in contrast, shows the mentioned decrease for $\Delta \lessapprox 0$. We find a maximum visibility of Rabi oscillation for positive detuning. This does not confirm the expectation for a two-state system, which is plotted by the solid line again using Eq. (2.58). The data of extracted oscillation decay times T_d, plotted in Fig. 4.22 (c), suggest that the longest coherence times are obtained close to resonance, as expected. However, as the oscillation visibility at this point is very small, the uncertainty in this data is pretty large.

4.6.4 Results of SiN_x - based samples

To verify that the short coherence times we observed on standardly fabricated samples are not limited by our experimental setup, we also measured the custom-made, high-quality phase qubit sample `UCSB-SiN` provided by the group of J. Martinis [84]. Figure 4.23 contains a selection of Rabi oscillation data which we measured on this sample. Using experimental conditions identical to the measurements described above, we obtained decay times of $T_d \approx 110$ ns, a factor of about 20 times longer than in the samples based on Nb-SiO_x technology. These data agree with the independent findings [84], and thus it is safe to conclude that our measurement apparatus does not introduce

additional sources of decoherence which might affect the qubit dynamics on a time scale of less than 100 ns.

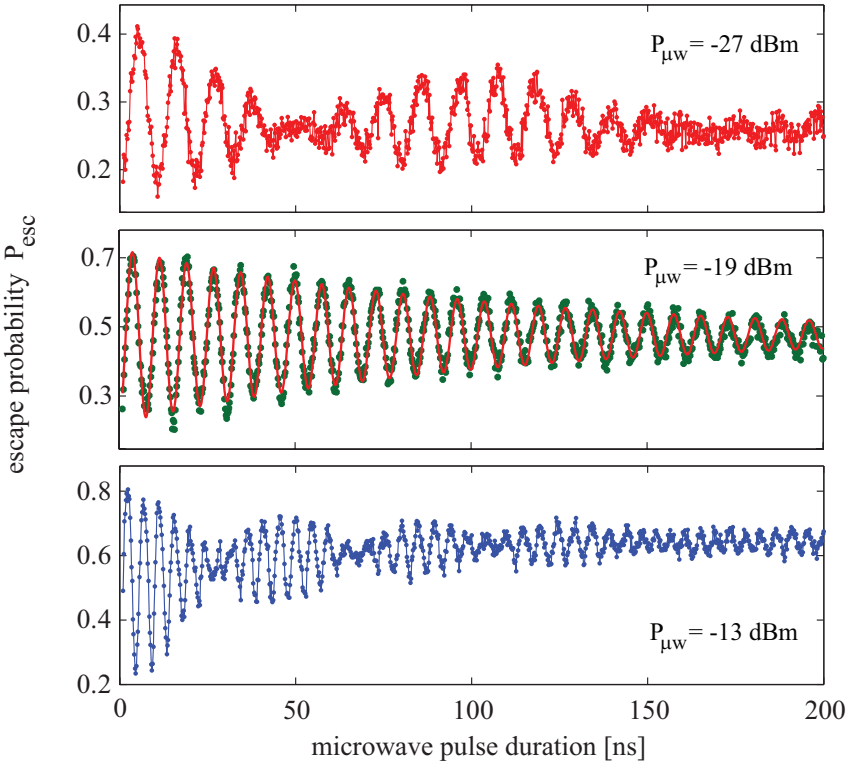

Figure 4.23: Rabi oscillation observed in sample UCSB-SiN, using a microwave frequency of 6.0 GHz at the indicated powers. At this particular flux bias, the oscillations showed a beating.

At certain values of external flux bias, we observe a beating in the coherent oscillation amplitude as shown in Fig. 4.23. The beating frequency depends on the Rabi frequency. This can be explained by coherent coupling to a parasitic two-level fluctuator as discussed in Sec. 4.6.1. While we observe this effect also in SiO_x-based samples, their short coherence times and larger expected density of parasitic fluctuators usually hinders observation of more than one beating period.

The dependence of the Rabi oscillation frequency on microwave amplitude is shown in Fig. 4.24 for a set of applied drive frequencies in the range of 6.0 to 8.7 GHz. Similarly to SiO_x-based samples, the oscillation frequency bends off from the linear dependence at large Rabi frequencies. It can be seen from this data that in a shallow potential well, corresponding to smaller drive frequencies, bending-off occurs at higher Rabi frequencies than that for the deep potential well. Also, at high drive amplitudes the oscillation frequency appears to saturate at a value which corresponds approximately to the anharmonicity of the potential well. For example, at a flux bias resulting in a resonance frequency of $\omega_{10}/2\pi = 6.5$ GHz, the anharmonicity is $(\omega_{10} - \omega_{21})/2\pi \approx 600$ MHz and at $\omega_{10}/2\pi = 8.7$ GHz it is ≈ 200 MHz (see Fig. 3.5). However, the curves obtained at 7.8 GHz and 8.15 GHz driving frequencies fall out of this direct propor-

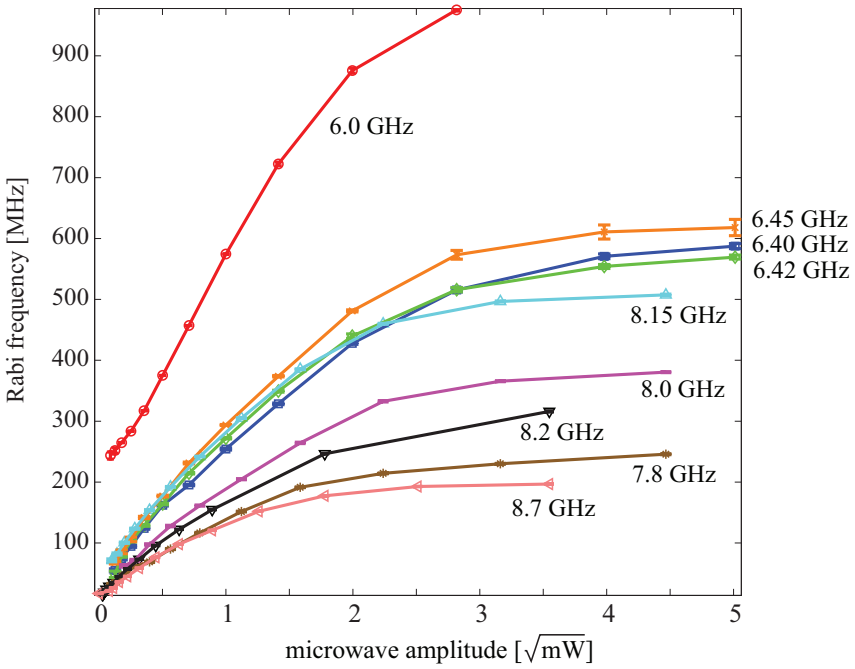

Figure 4.24: Rabi frequency vs. microwave amplitude measured using sample UCSB−SiN. Each curve was taken at the indicated resonant microwave frequency.

tionality, impeding a straightforward qualitative analysis.

The curve obtained using a microwave frequency of 6.0 GHz extrapolates to a Rabi frequency of about 200 MHz at zero drive amplitude. This can be explained by a detuning of the external flux bias from the exact resonance, which is expected to increase the oscillation frequency according to Eq. (2.58).

4.6.5 Conclusions

We observed driven coherent oscillations in phase qubits fabricated by standard technology employing SiO_x as insulator dielectric. Longest observed decay times were about 6 ns, while most samples showed typically $T_d \approx 3$ ns. We verified that these short coherence times do not originate from excess noise of our experimental setup. Measurements of a high-quality phase qubit sample employing SiN_x as a dielectric showed Rabi oscillation decay times above 100 ns, in agreement to independent measurements by the group of the University of California, Santa Barbara.

For weakly driven qubits, we find the expected linear dependence of the Rabi frequency on drive amplitude. At stronger driving, the oscillation frequency saturates at a value which is near the anharmonicity of the qubit potential well, indicating population of higher excited states.

Under strong driving conditions, we observe a reduction in oscillation amplitudes and decay times, which we attribute to population of higher excited states. This effect sets a limit to the shortest qubit gate operation time, which is given by the inverse of the Rabi frequency. Measurements of the coherent oscillation frequency dependence

on drive amplitude support the notion that higher excited states become populated when the Rabi frequency is comparable to the qubit anharmonicity.

4.7 Ramsey fringes

4.7.1 Theory

In the Bloch-sphere representation of the qubit state, Rabi oscillation can be understood as originating from continuous rotation of the Bloch-vector around the $\vec{x}$- or the $\vec{y}$ axis. In a Ramsey experiment [114], it is also possible to observe the precession around the $\vec{z}$-axis. Since these rotations do not change the $\vec{z}$-component of the Bloch vector, they are not affected by energy relaxation, but only by dephasing. This allows to directly measure the effective dephasing rate $1/T_2^*$, which is the sum of the dephasing rate by inhomogeneous broadening and the intrinsic dephasing rate,

$$\frac{1}{T_2^*} = \frac{1}{T_2'} + \frac{1}{T_2}. \tag{4.34}$$

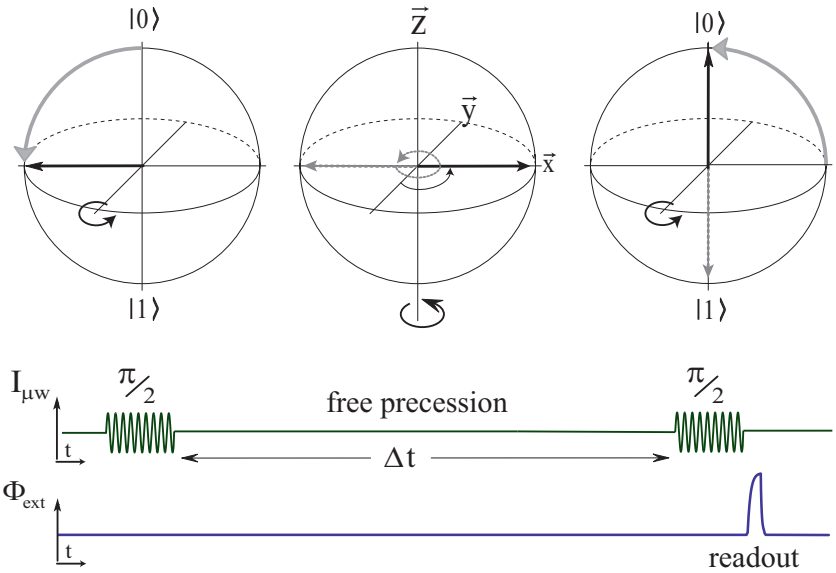

Figure 4.25: Illustration of the Ramsey experiment in the Bloch-sphere representation of the qubit state (top) and sequence of microwave and readout pulses (bottom). (a) A $\pi/2$-pulse rotates the Bloch-vector by 90° from $|0\rangle$ to the equator. (b) The vector precesses freely around the $\vec{z}$-axis during the time Δt. (c) A second $\pi/2$-pulse projects the acquired phase to the $\vec{z}$-axis. The qubit state is measured by the readout dc-flux pulse immediately afterwards.

Because only the $\vec{z}$-component of the Bloch vector is observable, a method is required to realize a phase-dependent projection to the $\vec{z}$-axis. A pulse sequence suitable to visualize the spin precession and dephasing is illustrated in Fig. 4.25. First, a so-called $\pi/2$-pulse is applied, which rotates the Bloch-vector by 90° to the equatorial plane. The duration of such a microwave pulse corresponds to one quarter of the Rabi

oscillation period, as it is determined beforehand at identical bias parameters. The qubit now undergoes free precession around the $\vec{z}$-axis at the Larmor frequency ω_{10}. After a variable delay time Δt, a second $\pi/2$-pulse is applied. The outcome of this second rotation now depends on the phase acquired during the time interval Δt.

If the microwave is tuned exactly to the Larmor frequency, it creates an effectively constant transversal field pointing to a fixed direction in the $\vec{x} - \vec{y}$-plane in the rotating frame, where no precession occurs. In contrast, if the microwave is detuned from the Larmor frequency, the effective field appears from the rotating frame to be rotating around the $\vec{z}$-axis at the frequency $\Delta = \omega_{\mu w} - \omega_{10}$. In this case, the second $\pi/2$-pulse in the Ramsey sequence can be understood as creating a rotation around either the $\vec{x}$- or $\vec{y}$-axis, depending on the phase $(\omega_{\mu w} - \omega_{10})\Delta t$ the microwave pulse acquired with respect to the rotating frame during the time Δt. The probability that the second $\pi/2$ microwave pulse rotates the Bloch vector to the excited state $|1\rangle$ therefore oscillates at the Ramsey frequency

$$\omega_{\mathrm{Ramsey}} = (\omega_{\mu w} - \omega_{10}) = \Delta, \tag{4.35}$$

which is equal to the detuning. Dephasing occurring during the free precession cycle then gives rise to a Ramsey fringe visibility which decays exponentially at the rate $1/T_2^*$.

4.7.2 Experimental results

Figure 4.26 shows the result of a Ramsey experiment performed on sample `UCSB-SiN` using two microwave pulses of frequency 7.7 GHz and duration 1.5 ns, which were detuned from the Larmor frequency by $\approx$ 300 MHz.

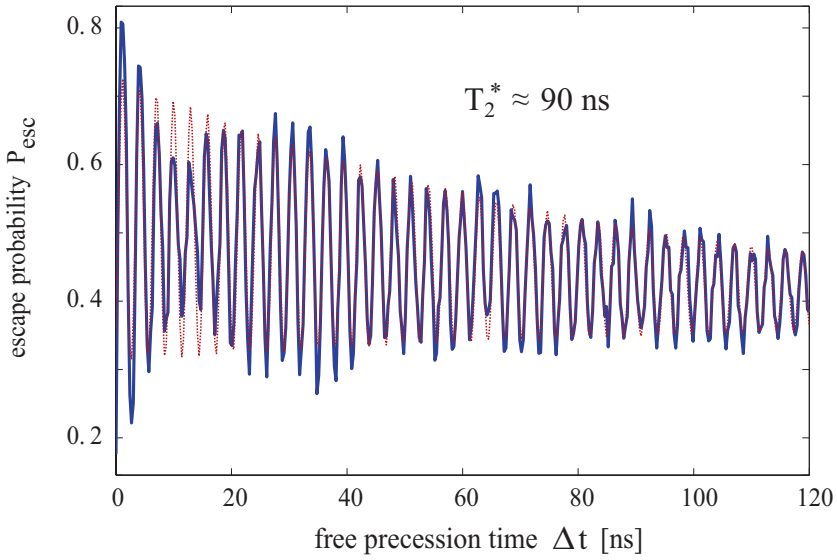

Figure 4.26: Result of an experiment to measure Ramsey oscillation using sample `UCSB-SiN`. The solid line connects measured data points, the dotted line is a fit to a sine function decaying exponentially with a time constant of $T_2^* = 90$ ns.

The escape probability was measured by applying the readout dc-pulse immediately after the second microwave pulse. It shows the expected oscillation at the detuning

frequency when the separation between the two pulses Δt is varied. Fitting these Ramsey fringes to an exponentially decaying cosine, as shown by the dotted line in Fig. 4.26, results in a dephasing time of $T_2^* \approx 90$ ns, in accordance to independent measurements using a similar sample [84].

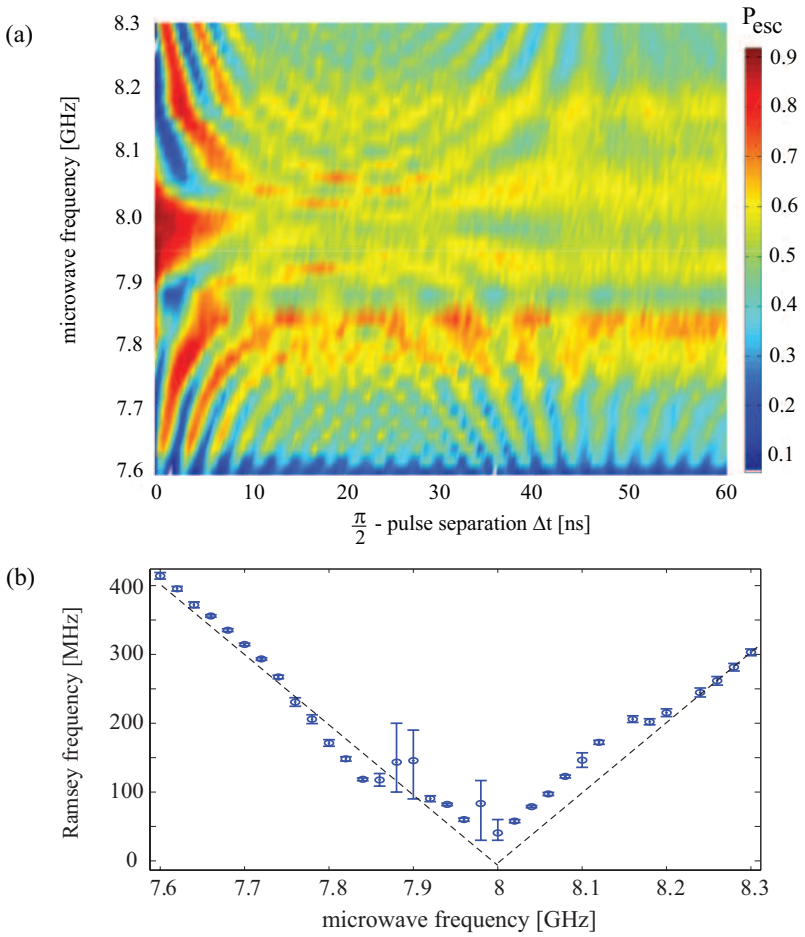

Figure 4.27: (a) Escape probability (color-coded) vs. the time delay between two $\pi/2$-pulses and the microwave frequency. Ramsey oscillation is observed at all frequencies except near the exact resonance close to 8.0 GHz. (b) Ramsey oscillation frequency vs. microwave frequency used to generate the $\pi/2$-pulses. Dashed lines have unity slope and originate at 8.0 GHz.

The amplitude of the Ramsey oscillation shows a low-frequency beating. This is expected to originate from the finite duration of the microwave $\pi/2$-pulses, during which some precession occurs when the detuning is large. In an improved pulse sequence [101], this is circumvented by using two $\pi/2$-pulses always at exact resonance and creating the detuning by a change of the Larmor frequency through a dc-flux pulse between the microwave pulses.

To check whether the observed Ramsey frequency indeed corresponds to the detuning, we repeated the measurement for several microwave frequencies. This data is

plotted in Fig. 4.27 (a), showing the escape probability color-coded vs. both the $\pi/2$-pulse separation Δt and the microwave frequency. The pattern shows the characteristic increase of oscillation frequency when the microwave is tuned away from the exact resonance close to 8.0 GHz. In this figure, the particular pattern near $\Delta t \approx 45$ ns is a plotting artefact. It originates in an interference effect which occurs when the Ramsey frequencies exceed the experimental resolution at which the detuning was varied.

We find the exact resonance by plotting the Ramsey oscillation frequency vs. the applied microwave frequency as it is shown in Fig. 4.27 (b). The two dashed lines have unity slope and are hence fitted to the data by solely shifting their origin, resulting in a Larmor frequency of 8.0 GHz.

An irregularity in the Ramsey oscillations is found in close vicinity of $\omega_{\mu w}/2\pi$ = 7.88 GHz microwave frequency which can be seen in Fig. 4.27. We speculate that this could be due to excitation of the $|1\rangle \rightarrow |2\rangle$-transition, which is calculated to have a frequency of $\omega_{21}/2\pi = 7.78$ GHz. The difference between the applied microwave frequency and $\omega_{21}/2\pi = 7.78$ is 100 MHz, which is close to the expected Ramsey frequency $\omega_{\mathrm{Ramsey}}/2\pi$ = 120 MHz at this point.

4.7.3 Conclusions

The long coherence times of the SiN_x-based sample allowed us to measure its dephasing time T_2^* directly in a Ramsey fringe experiment. The data show the expected linear dependence of Ramsey frequency on the detuning of the microwave from the exact qubit resonance. In agreement to independent measurements, we find a T_2^*-time of $\approx$ 90 ns, which indicates that no significant sources of low-frequency noise exist in our experimental setup.

4.8 Demonstration of the phase gate

For quantum computation it is necessary to have complete control of every qubit, which means that it must be possible to rotate the Bloch vector to an arbitrary point on the sphere. Any such rotation can be decomposed into three subsequent rotations around two orthogonal axes [19]. Whether a resonant microwave pulse induces a rotation around the $\vec{x}$- or $\vec{y}$-axis can be controlled by its phase, and therefore the ability of fast microwave phase modulation allows to perform any single qubit gate.

However, for phase qubits it is experimentally very easy to realize rotations around the $\vec{z}$-axis, which implements the qubit *phase gate*. This is done by applying a short dc-pulse of external flux, which changes the Larmor frequency by modifying the energy difference between the qubit states. The Bloch vector therefore drifts out of the frame which rotates at the microwave frequency, effectively changing the phase of subsequent microwave pulses. Any qubit operation can thus be realized by using a combination of fixed-phase microwave pulses and flux pulses.

4.8.1 Experimental results

We demonstrate this in an experiment using the pulse sequence shown in Fig. 4.28 (a). Between two microwave $\pi/2$-pulses of 7.7 GHz we applied a detuning flux pulse of constant duration 5.8 ns but varying amplitude. As the relative phase between microwave and Larmor frequencies is given by the integral over the time-dependent detuning, the probability to measure the excited state oscillates with increasing detuning

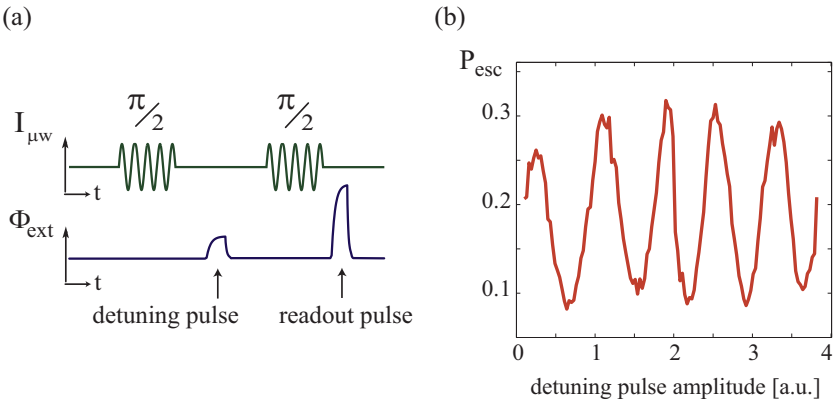

Figure 4.28: (a) Pulse sequence suitable to demonstrate the phase gate. (b) The oscillating escape probability originates in rotations around the $\vec{z}$-axis, whose velocity is controlled by the detuning pulse amplitude.

pulse amplitude as shown in Fig. 4.28 (b). The figure indicates that a pulse amplitude of 4 a.u. induces 5 $\vec{z}$-rotations, or about 0.4 π-rotations per nanosecond. Using larger detuning pulse amplitudes and shorter durations, this technique should allow to realize a $\vec{z}$-rotation by π in about one nanosecond.

4.8.2 Conclusions

We describe an implementation of the phase gate which is based on the application of a short detuning flux bias pulse. This technique does not require additional experimental resources and will be very useful for qubit state tomography. We demonstrate controlled rotation of the Bloch vector around the $\vec{z}$-axis by varying the amplitude of the detuning flux pulse. With this method, it is possible to realize a phase-π-gate within less than 2 ns.

4.9 Temperature dependence of coherence times

The study of the influence of temperature on coherence properties of superconducting qubits is important in many aspects. It may add new insights to understand better the origins of decoherence and can help to verify theoretical models. Whether it is possible to operate qubits at temperatures of a few hundred milikelvin is an important question regarding the realization of a quantum computing chip, which would contain hundreds of qubits. The large number of required biasing wires would increase the heat load to the cryostat and consequently raise its base temperature. Also, dissipative readout or control circuits like dc-SQUIDs or RSFQ logic give rise to a warming of the qubit chip. Lastly, exploring the limiting factors which hinder operation of contemporary qubits at higher temperatures may enable designing specific samples which work in the experimentally easily accessible temperature range of about 300 mK.

4.9.1 Theory

When it is possible to truncate the phase qubit to a two-level system it can be described as a spin-1/2 system which has the Hamiltonian

$$\mathcal{H}_q = -\frac{1}{2}\hbar\Delta\sigma_x + \frac{1}{2}\epsilon\sigma_z, \tag{4.36}$$

where ϵ is the difference of state energies and $\frac{1}{2}\hbar\Delta$ is the transition matrix element. If the latter is large, the system oscillates between its two states at the Rabi frequency Δ.

Decoherence is modelled in the Caldeira-Leggett approach [52] as resulting from coupling of the spin to an infinite set of harmonic oscillators. The dilemma that while quantum mechanics requires a system to evolve unitarily but dissipation is experienced as a non-reversible effect is hereby solved - the energy is distributed among a large number of degrees of freedom and unlikely to return to the spin. The coupled system is thus described by the so-called "spin-boson" Hamiltonian [52, 115, 60]

$$\mathcal{H} = \mathcal{H}_q + \sum_\alpha \left(\frac{1}{2}m_\alpha\omega_\alpha^2 x_\alpha^2 + \frac{p_\alpha^2}{2m_\alpha}\right) + \frac{1}{2}q_0\hat{\sigma}_z\sum_\alpha C_\alpha x_\alpha, \tag{4.37}$$

where the second term summarizes the α harmonic oscillators of the bath, each having a coordinate x_α , mass m_α, momentum p_α and eigen frequency ω_α. The third term adds the interaction between the spin and the bath, where a linear coupling of strength C_α between the coordinates of the oscillators and the z-component of the spin is assumed.

In thermal equilibrium, all information about the boson bath is contained in the spectral density function $J(\omega)$ [115]

$$J(\omega) = \frac{\pi}{2\hbar}\sum_\alpha \frac{C_\alpha^2}{m_\alpha\,\omega_\alpha}\,\delta(\omega-\omega_\alpha), \tag{4.38}$$

where the Dirac δ-functions add to a continuous function in the limit of infinitely many bath modes [60]. For an electric circuit having an impedance $Z(\omega)$, the spectral density function is [60]

$$J(\omega) = \omega\frac{R_Q}{\mathrm{Re}[Z(\omega)]}, \tag{4.39}$$

where $R_Q = h/(2e)^2$ is the superconducting resistance quantum and $\mathrm{Re}[Z(\omega)]$ denotes the real part of the circuit impedance.

Knowledge of the noise spectrum allows to derive the temperature dependence of the relaxation time T_1 and dephasing time T_2 [115, 116, 117, 118]. For finite temperature T,

$$T_1^{-1} \propto J(\omega)\,\coth\frac{\hbar\omega}{2k_BT}\bigg|_{\omega\to\Delta E/\hbar} \tag{4.40}$$

$$T_2^{-1} \propto \frac{T_1^{-1}}{2}\bigg|_{\omega\to\Delta E/\hbar} + J(\omega)\,\coth\frac{\hbar\omega}{2k_BT}\bigg|_{\omega\to 0}. \tag{4.41}$$

Equation (4.40) shows that the relaxation rate is only affected by bath modes at the qubit frequency $\omega_{10} = \Delta E/\hbar$. The dephasing rate Eq. (4.41) has a contribution from

the relaxation rate, which reflects the fact that phase information is lost when relaxation occurs. Additionally, dephasing is affected by the bath properties at low frequencies. When x is small, $\coth(x) \approx 1/x$, and the dephasing rate Eq. (4.41) can thus be written using Eq. (4.39) as [60]

$$T_2^{-1} \propto \frac{1}{2}\,\omega \frac{R_Q}{\mathrm{Re}[Z(\omega)]}\coth\frac{\hbar\omega}{2k_BT}\bigg|_{\omega\to\Delta E/\hbar} + \frac{2k_BT}{\hbar}\frac{R_Q}{\mathrm{Re}[Z(0)]}. \tag{4.42}$$

We see that beneath the coth-dependence, the dephasing rate increases linearly with temperature at a rate determined by the low-frequency impedance of the environment.

Thermal equilibrium populations

Thermal population of the excited qubit state will result in a loss of visibility of coherent oscillations. This becomes relevant when the thermal energy $k_B\,T$ is comparable to the energy difference ΔE between the two qubit states. In the following, the temperature dependence of the expected measurement contrast is calculated.

The maximal contrast at which a change in the level population can be observed is given by the population difference

$$n = N_g - N_e \tag{4.43}$$

in thermal equilibrium. The populations of the ground state N_g and excited state N_e evolve according to the principle of detailed balance [119],

$$\frac{\mathrm{d}N_g}{\mathrm{d}t} = W_\downarrow N_e - W_\uparrow N_g \tag{4.44}$$

$$\frac{\mathrm{d}N_e}{\mathrm{d}t} = W_\uparrow N_g - W_\downarrow N_e. \tag{4.45}$$

Taking into account relaxation of the excited state occuring at a rate $\Gamma_1 \equiv T_1^{-1}$, the transition rate from ground to excited state $W_\uparrow$ and the rate from excited to ground state $W_\downarrow$ read

$$W_\uparrow = W \tag{4.46}$$

$$W_\downarrow = W + \Gamma_1. \tag{4.47}$$

Here, W is the rate at which the thermal bath induces transitions between levels, which is equal in both directions. As in thermal equilibrium $\frac{\mathrm{d}N_g}{\mathrm{d}t} = 0$, we obtain a condition for the ratio of the transition rates from Eq. (4.44)

$$\frac{W_\uparrow}{W_\downarrow} = \frac{N_e^0}{N_g^0} = \exp\left(-\Delta E/k_BT\right). \tag{4.48}$$

In this equation, the ratio of the equilibrium populations N_g^0 and N_e^0 is given by the Boltzmann factor. Solving Eqs. (4.44) and (4.45) for n yields

$$\frac{\mathrm{d}n}{\mathrm{d}t} = \frac{n_0 - n}{T_1}, \tag{4.49}$$

where $T_1 = 1/(W_\downarrow - W_\uparrow)$ has been used. We arrive at the sought population difference in thermal equilibrium,

$$n_0 = \frac{W_\downarrow - W_\uparrow}{W_\uparrow + W_\downarrow} = \frac{1}{1 + 2\,W/\Gamma_1} = \tanh(\Delta E/2k_BT). \tag{4.50}$$

The last expression, which is the most important result of this section, has been obtained using Eq. (4.48) and the identity

$$\tanh(\Delta E/2k_BT) = \frac{1-\exp(\Delta E/k_BT)}{1+\exp(\Delta E/k_BT)}. \tag{4.51}$$

The maximal measurement contrast, assuming that it is limited only by the thermal bath equilibrating the population of the two qubit levels, hence follows the $\tanh$ dependence given in Eq. (4.50). At the temperature where $k_BT = \Delta E$, the contrast is expected to drop to n_0 = 46 %.

Integration of Eq. (4.49) shows that the system reaches thermal equilibrium after a mean time which is equal to the energy relaxation time T_1:

$$n(t) = n_0\left(1-\mathrm{e}^{-t/T_1}\right). \tag{4.52}$$

A similar calculation is used to find the equilibrium population difference n_D in a driven system. In the incoherent limit, the drive gives rise to a transition rate Γ_D which is equal for both directions $|g\rangle \leftrightarrow |e\rangle$, similar as the thermal bath. Detailed balance in this case results in

$$\frac{\mathrm{d}n_D}{\mathrm{d}t} = -2\,\Gamma_D\,n. \tag{4.53}$$

Finally, combining the rates Eq. (4.53) and Eq. (4.49),

$$\frac{\mathrm{d}n_{D0}}{\mathrm{d}t} = -2Wn + \frac{n_0-n}{T_1}, \tag{4.54}$$

we arrive at the population difference n_{D0} in steady state $\mathrm{d}n_{D0}/\mathrm{d}t$ = 0 for the continuously driven system coupled to a thermal bath,

$$n_{D0} = \frac{n_0}{1+2W/\Gamma_1}. \tag{4.55}$$

4.9.2 Measurement limitations

In order to observe the phase dynamics at higher temperatures it is essential to avoid thermal activation out of the shallow potential well. As it was discussed in Sec. 2.2.5, the activation rate increases exponentially as the potential barrier height becomes comparable to the thermal energy $k_{\mathrm{B}}T$. At high temperatures it is therefore required to operate in a deep potential well where thermal activation can be neglected.

On the other hand, the possibility to use an rf-SQUID as a quantum bit is build on the ability to truncate it to a two-state system. This requires the qubit potential to be sufficiently anharmonic, hereby separating higher states through the different transition frequencies between neighboring levels. However, as energy relaxation (and tunneling) give rise to a certain width of each energy level, this is only guaranteed as long as the condition

$$\hbar\omega_{21} + \frac{1}{2}(\delta E_1 + \delta E_2) \ll \hbar\omega_{01} \tag{4.56}$$

is satisfied. Here, δE_n is the full width of level n arising from its finite lifetime τ_n and ω_{fi} is the transition frequency from level i to level f, see Fig. 4.29 for illustration. The finite width of the ground state is hereby given by the tunnel rate through the potential barrier.

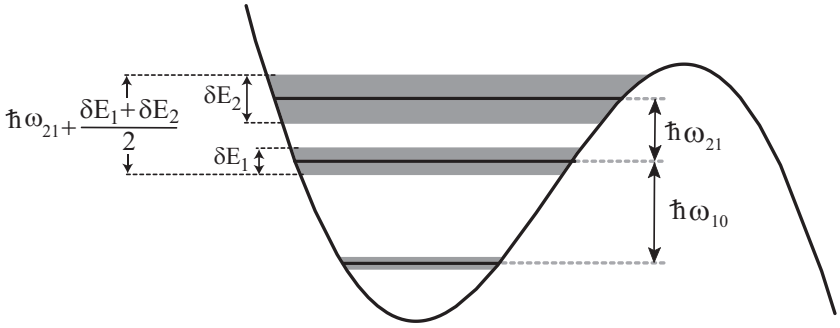

Figure 4.29: Sketch of a qubit potential well containing three energy levels, indicating the transition frequencies ω_{10} and ω_{21} and the level widths δE_n.

As it is indicated in Fig. 4.29, the life time of the nth excited states is expected to be shorter by roughly a factor of about n than that of the first excited state. Using the time-energy-uncertainty relation $\delta E_1\, \tau_1 \cong \hbar$ to estimate the width of the first level from its measurable lifetime $\tau_1 = T_1$, Eq. (4.56) becomes

$$\Delta\omega > \frac{3}{2}\, T_1^{-1}, \tag{4.57}$$

where $\Delta\omega = \omega_{10} - \omega_{21}$ expresses the anharmonicity of the potential well and $\delta E_2 = 2\delta E_1$ has been assumed. This crude estimation indicates that for the investigated standardly fabricated samples, having T_1-times of about 3 ns, to avoid population of the second excited state the anharmonicity $\Delta/2\pi$ must be larger than 80 MHz.

Note that this estimation disregards leakage to higher states due to large drive amplitudes as discussed in Sec. 4.6.1. To avoid this effect, the Rabi frequency ω_R must be smaller than the anharmonicity,

$$\Delta\omega > \omega_R. \tag{4.58}$$

Taking into account the required Rabi frequencies $\omega_R \approx 2\pi\, T_1^{-1}$ to allow observation of coherent oscillations in the short-living excited state population, the condition Eq. (4.58) turns actually more stringent than Eq. (4.57).

We conclude that the study of the coherence times of phase qubits at higher temperature requires operating them in deep potential wells in order to avoid thermal activation. The limit of the two-level operation is set by the energy relaxation rate T_1^{-1}, which has to be smaller than the anharmonicity $\Delta\omega$. Due to their short coherence times, our SiO_x-based samples at higher temperatures can only be studied in the nearly classical multi-level limit. In contrast, the much longer coherence times of the SiN-based sample `UCSB-SiN` allowed its operation in the two-level limit also at higher temperatures and using deep potential wells.

4.9.3 Measurement protocol

Before coherent dynamics were investigated at higher temperatures, we measured the dependence of the escape rate from the ground state on temperature, as described in Sec. 4.2.2. This allowed to determine a suitable working point of external flux at which thermal activation remained negligible. Microwave spectroscopy was then performed at the base temperature in order to find the qubit resonance at the working point. After

observation of coherent oscillations at the working point, external flux bias, microwave frequency and amplitude were varied by small amounts in order to maximize the oscillation amplitude and life time.

All measurements presented in the remainder of this chapter were obtained while keeping the qubit bias parameters constant at all temperatures. In order to preserve high measurement contrast the amplitude of the readout pulse had to be reduced at high temperatures, where qubit escape from the excited state to the deep well becomes possible not only by quantum tunnelling but also by thermal activation over the barrier. We adjusted the readout amplitude at each temperature by the automated calibration procedure described in Sec. 4.3.5.

The width of the measured switching-current histogram of the readout dc-SQUID increases in the thermal regime, which reduces the contrast between the two qubit states. We therefore separated the contributions of the two states to the readout SQUID switching-current distribution by the fitting procedure using weighted histograms of the two flux states as described in Sec. 3.4.2.

A complete data set to observe the temperature dependence of coherent oscillation consists of approximately 8000 histograms. At each of the typically 40 temperature values in the range of 20 mK to 800 mK, the escape probability was probed for about 200 values of the microwave pulse duration. As each histogram comprises at least 1000 measurements, in total about 8 million measurements were acquired at a typical rate of 300 measurements per second. Up to five minutes were necessary to allow for stabilization of the dilution unit temperature at every set point. One complete measurement thus took a time of more than 10 hours. The stability of the external qubit parameters during this time was guaranteed by using a mains supply to energize the biasing electronics. It was impossible to measure in an automated fashion at temperatures above 800 mK because the He^3/He^4-mixture began to evaporate at about 900 mK.

4.9.4 Temperature dependence of Rabi oscillations

Results of SiO_x - based samples

We measured the influence of temperature on coherent oscillations in the SiO_x based samples `Hyp30S` and `VTT30`, both having comparable coherence times and qubit parameters. In the following we only present results obtained on sample `VTT30`, which were similar to those acquired using the other sample.

Figure 4.30 (a) displays coherent oscillations in sample `VTT30` at the indicated temperatures. The microwave drive frequency was $\omega_{\mu w}/2\pi$ = 16.5 GHz and its amplitude was adjusted to result in a coherent oscillation frequency of $\omega_R/2\pi$ = 750 MHz. For the same bias parameters, Fig. 4.30 (a) contains the result of a measurement of the oscillation frequency dependence on drive amplitude, indicating that the chosen amplitude of $\approx 0.28\sqrt{\mathrm{mW}}$ was small enough to remain in the linear regime. The observed oscillations decay at the lowest temperature with a time constant of about 4 ns, as it is typical for all our SiO_x - based samples. Remarkably, even at the highest temperature of 800 mK oscillations can be clearly seen, though their amplitude and decay time are both reduced by about a factor of 2.

A systematic evaluation of the temperature dependence of coherent oscillation amplitude and decay time is given by the data presented in Fig. 4.31, using the fitting procedure described in Sec. 4.6.3. This figure also includes measurements using dif-

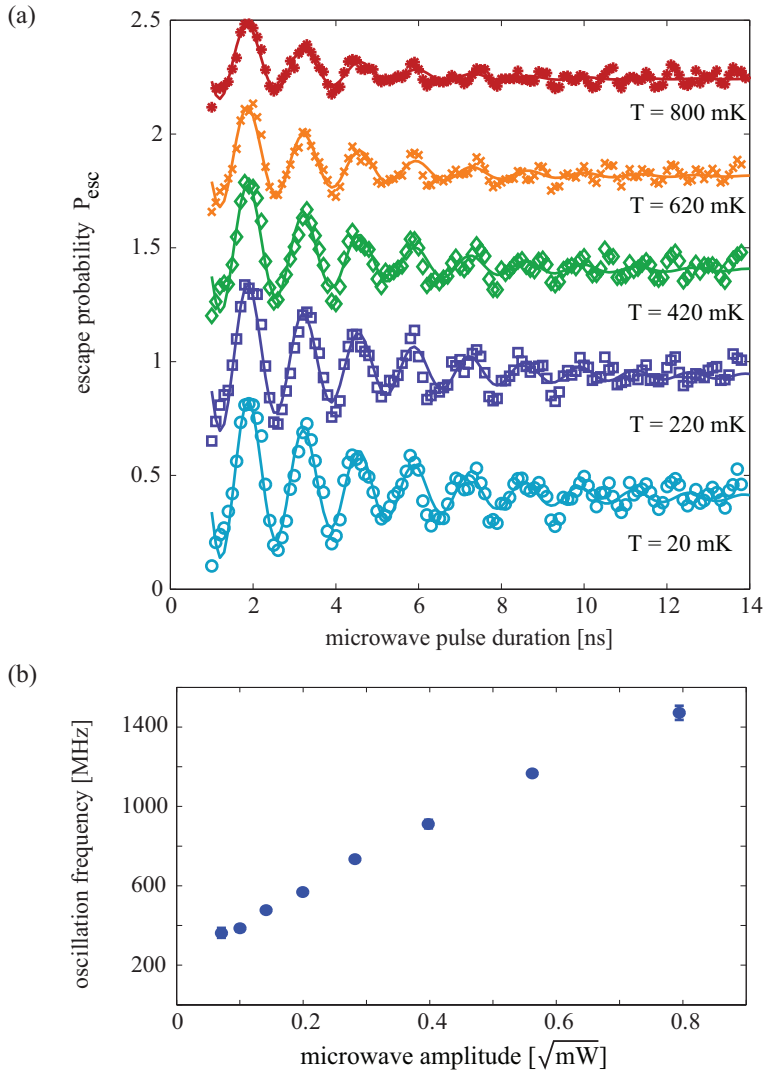

Figure 4.30: (a) Coherent oscillations observed using sample VTT30, driven at 16.5 GHz microwave frequency and amplitude $0.28\sqrt{\mathrm{mW}}$, at the indicated temperatures. Each curve is offset by P_{esc}=0.5 for clarity. (b) Coherent oscillation frequency vs. microwave drive amplitude at identical bias parameters, measured at T=20 mK.

ferent external flux biases, corresponding to qubit resonances at 15.7 GHz, 16.5 GHz and 17.3 GHz. At 15.7 GHz, the coherent oscillation frequency was $\omega_R/2\pi$ = 750 MHz and thus equal to the 16.5 GHz data, while for 17.3 GHz it was with $\omega_R/2\pi$ = 830 MHz about 10 % larger. The oscillation frequency changed with temperature less than $\approx$ 2 %, which is within the confidence intervals of the fits. Figure 4.31 (a) shows that for all datasets the oscillation amplitude remained unchanged below a temperature of about 200 mK and then decreased monotonically to approximately 50% of its value at the highest measured temperature of 800 mK. The solid lines in this figure are plots

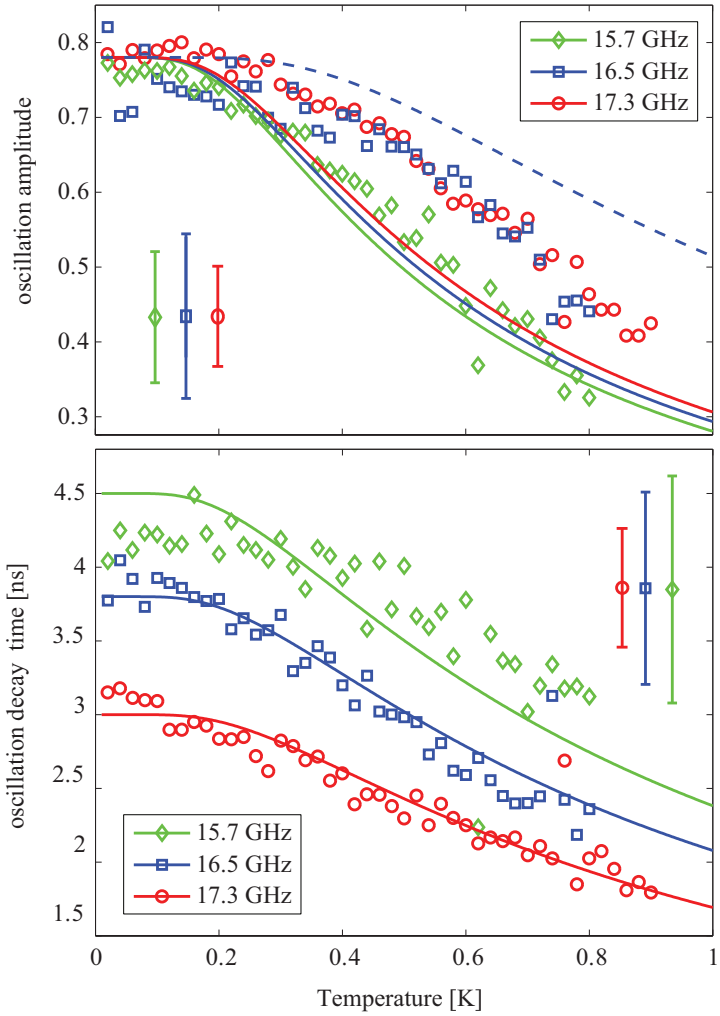

Figure 4.31: (a) Coherent oscillation amplitude (top) and decay time (bottom) versus temperature, measured using sample VTT30. Each data set corresponds to an adjusted magnetic field resulting in resonance at the applied microwave frequency $\omega_{\mu w}/2\pi$ indicated in the legend. In (a), the solid lines show the expected contrast following $C_0 \cdot \tanh(\hbar\omega_{\mu w}/2k_BT)$ and the dashed line is the expected contrast for a $|0\rangle \leftrightarrow |2\rangle$-oscillation. In (b), the solid lines show the expected T_1-times Eq. (4.60) for $\Delta E = \hbar\omega_{\mu w}$. Error bars in the insets give average confidence intervals of the fits.

to the equation

$$C(T) = C_0 \tanh\left(\frac{\hbar\omega_{\mu w}}{2k_BT}\right), \tag{4.59}$$

which according to Eq. (4.50) is the theoretical expectation for the oscillation visibility reduction due to thermal population of the first excited qubit state. For these plots, C_0 was set to the observed amplitude at the lowest temperature and $\omega_{\mu w}$ corresponds to the applied microwave frequency. The oscillation amplitude measured in the most shallow potential well using 15.7 GHz microwave frequency does indeed show the expected

temperature dependence, while the other two data sets display a larger amplitude than expected at high temperatures. This could be explained by assuming that the oscillation in the deeper potential wells involves the second excited state, which is less affected by thermal population due to its about twice larger energy. The dashed line in Fig. 4.31 (a) is a plot of Eq. (4.51) using $\omega_{\mu w}/2\pi = 2{\cdot}16.5$ GHz to show the expected contrast of a $|0\rangle \leftrightarrow |2\rangle$ oscillation. However, as it was pointed out before, the effective environment of the qubit may change drastically when changing the flux bias due to coupling to parasitic fluctuators, rendering a quantitative analysis difficult.

The temperature dependence of the oscillation lifetime obtained from the same data is shown in Fig. 4.31 (b). The difference in the absolute values of the lifetimes when changing the flux bias may be interpreted either as being due to varying coupling to parasitic resonators or to an increased probability of leakage to higher levels for deeper potential wells. For phase qubits, the expected temperature dependence of the energy relaxation time was given by Eq. (3.1.2), which is shown in the figure by the solid lines being plots of the equation

$$T_1 = 2\,T_1^0 \left[1 + \coth\left(\frac{\Delta E}{2k_B T}\right)\right]^{-1}, \tag{4.60}$$

where $\Delta E = \hbar\omega_{\mu w}$ was the applied microwave frequency and T_1^0 is the fitting parameter for the lifetime at zero temperature. In contrast to the oscillation amplitude, the theoretical expectation for the relaxation time is more closely met by the datasets obtained at 16.5 GHz and 17.3 GHz driving frequencies. The dataset obtained at 15.7 GHz shows a weaker temperature dependence. As it was mentioned in Sec. 4.6.1, the decay rate of Rabi oscillation is determined by the mean of relaxation and dephasing rates. Comparing the decay rate of Rabi oscillation to the temperature dependence of the T_1 time is therefore inaccurate. Nevertheless, relaxation contributes a large part to the dephasing rate as it was shown by Eq. (4.41).

Results of the SiN_x - based sample

The temperature dependence of coherent oscillations in the high-quality qubit sample `UCSB-SiN` was measured using microwave frequencies in the range of 7.4 GHz to 8.7 GHz. Figure 4.32 exemplarily shows data obtained using 7.4 GHz drive frequency at three temperatures. At 15 mK, the oscillations showed a life time of about 100 ns and an amplitude corrected for histogram overlap of about 0.85, whereas at 335 mK both amplitude and life time were substantially smaller. The results obtained by fitting the oscillations to exponentially decaying sine functions are summarized in Fig. 4.33 for three external flux biases adjusted to result in resonance at the chosen microwave drive frequency indicated in the legends.

The oscillation amplitudes display a distinct behavior which is shown in Fig. 4.33 (a). Increasing the temperature, the amplitude of the oscillation taken at 7.4 GHz is reduced slowly up to a temperature of about 250 mK, beyond which it decreases rapidly and reaches zero at 350 mK. The data for 8.0 GHz microwave frequency does not depend on temperature below about 300 mK, but quickly approaches zero close to 400 mK. Most peculiar, the oscillation amplitude recorded using 8.7 GHz drive frequency first drops by about 30 % at 200 mK, but with further increasing the temperature reaches a maximum value at 315 mK, which is actually larger than its value at 15 mK. Beyond the maximum, the oscillation decays quickly and at a similar rate as

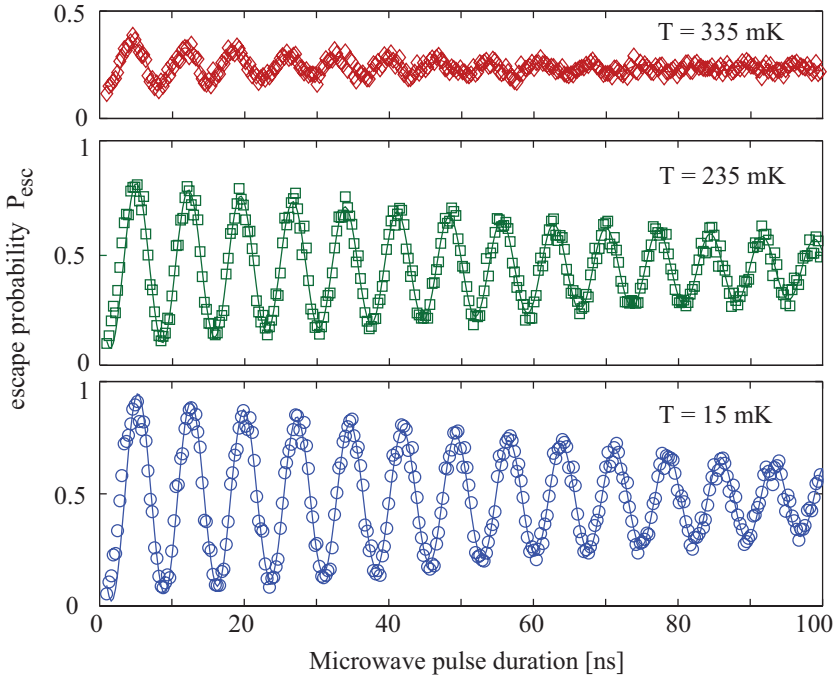

Figure 4.32: (a) Coherent oscillations observed using sample UCSB−SiN, driven at 7.4 GHz microwave frequency, at the indicated temperatures.

observed for the other drive frequencies, vanishing at a temperature of 415 mK. This non-monotonic temperature dependence was reproducible and was also observed at drive frequencies of 8.6 GHz and 8.9 GHz.

To explain the non-monotonic temperature dependence, we speculate that the oscillation amplitude is limited by coupling to parasitic two-level fluctuators. Increasing temperature, on one hand, may reduce the fluctuators-induced decoherence as some part of the two-level fluctuators gets saturated by energy absorbed from the thermal bath. On the other hand, higher temperature leads to conventional loss of oscillation visibility due to thermal population of the excited state as described in Sec. 4.9.1.

We find that the temperature T_Δ up to which the oscillation can be seen at a chosen flux bias is very correlated with the energy difference between the two qubit states as $T_\Delta = \Delta E/k_B$. Assuming that the microwave was adjusted to exact resonance we have $\Delta E = \hbar\omega_{\mu w}$, from which we calculate T_Δ = 355 mK at $\omega_{\mu w}/2\pi$ = 7.4 GHz, T_Δ = 384 mK at $\omega_{\mu w}/2\pi$ = 8.0 GHz, and T_Δ = 418 mK at $\omega_{\mu w}/2\pi$ =8.7 GHz, in striking agreement to experimental observation. However, the very rapid decrease of the amplitude close to T_Δ can not be explained only by taking into account thermal depolarization of the qubit as discussed in Sec. 4.9.1, because this process results in a less rapid loss of contrast with temperature, which is shown in Fig. 4.33 (a) by solid lines plotting the function $C_0 \cdot \tanh(\hbar\omega_{\mu w}/2k_BT)$.

The temperature dependence of the Rabi oscillation decay time is given in Fig. 4.33 (b), which shows a similar behavior at all studied microwave frequencies. To facilitate comparison between the data sets, the decay times obtained at 8.0 GHz and 8.7 GHz were multiplied by a constant factor to make them coincide with the 7.4 GHz data at

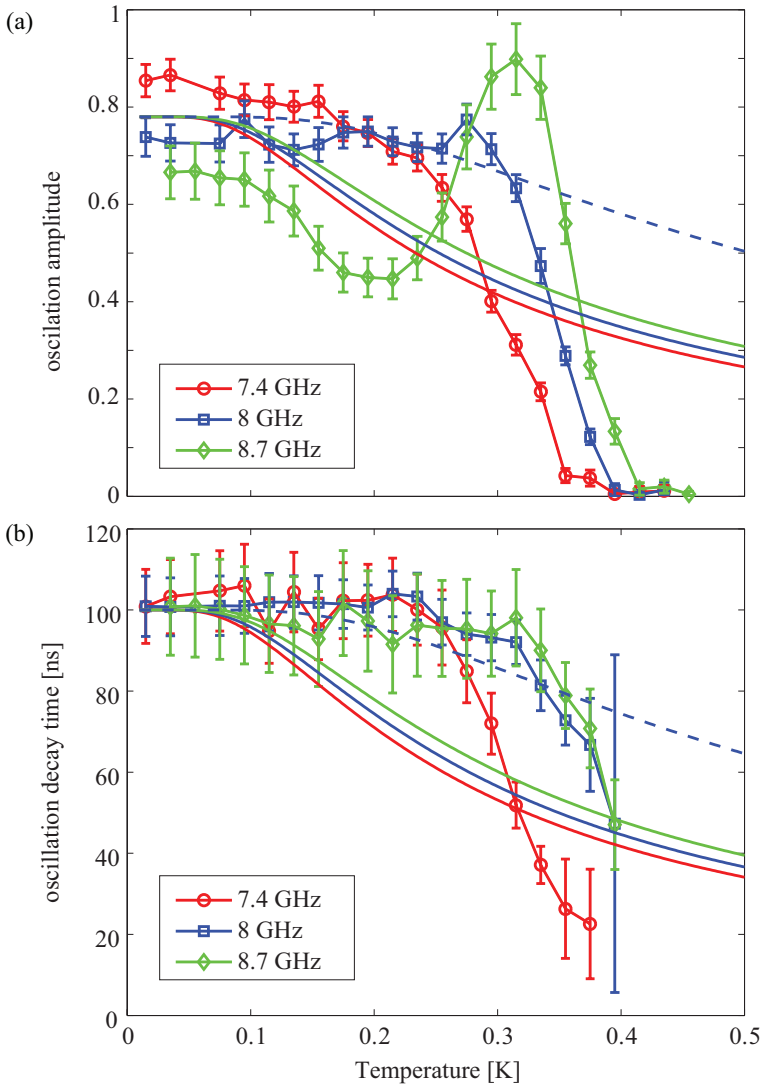

Figure 4.33: (a) Amplitude of coherent oscillation vs. temperature obtained at the indicated microwave frequency $\omega_{\mu w}/2\pi$. Solid lines: expected contrast following $C_0 \cdot \tanh(\hbar\omega_{\mu w}/2k_BT)$, dashed line: expected contrast for a $|0\rangle \leftrightarrow |2\rangle$-oscillation. (b) Coherent oscillation lifetime T_d vs. temperature. Solid lines: expected T_1-time Eq. (4.60) for $\Delta E = \hbar\omega_{\mu w}$, dashed line: Eq. (4.60) for $\Delta E = 2\,\hbar\omega_{\mu w}$ for $\omega_{\mu w}/2\pi$=8.0 GHz.

the temperature of 15 mK. These decay times at the lowest temperature were 29.5 ns at 8.0 GHz and 42.5 ns at 8.7 GHz. The scaled plots show that the oscillation decay time does not depend on temperature up to about 300 mK and rapidly decreases at higher temperatures, similarly to the oscillation amplitude.

The solid lines in Fig. 4.33 (b) are plots of the T_1 time Eq. (4.60), showing the $[1 + \coth(\Delta E/k_BT)]^{-1}$ - behavior. In contrast to the data for the SiO_x-based sample `VTT30`, none of the datasets fits to this dependence. The model predicts a smooth

decrease of the T_1 time starting above about 100 mK, whereas the data show a rapid decrease above 300 mK. For comparison, the figure also includes a plot of Eq. (4.60) for the decay time of the second excited state, which better fits the data below a temperature $T_\Delta = \Delta E/\hbar$. As a matter of fact, a small population of the second excited state can not be completely ruled out for the datasets obtained at 8.0 GHz microwave frequency and above. As Fig. 3.5 shows, the anharmonicity of the potential well $\Delta\omega$ is calculated to be approximately 310 MHz at 7.4 GHz, 224 MHz at 8.0 GHz and 158 MHz at 8.7 GHz. For the shown data, the ratios between the Rabi frequency ω_R and the anharmonicity were 0.44 at 7.4 GHz, 0.92 at 8.0 GHz and 0.98 at 8.7 GHz.

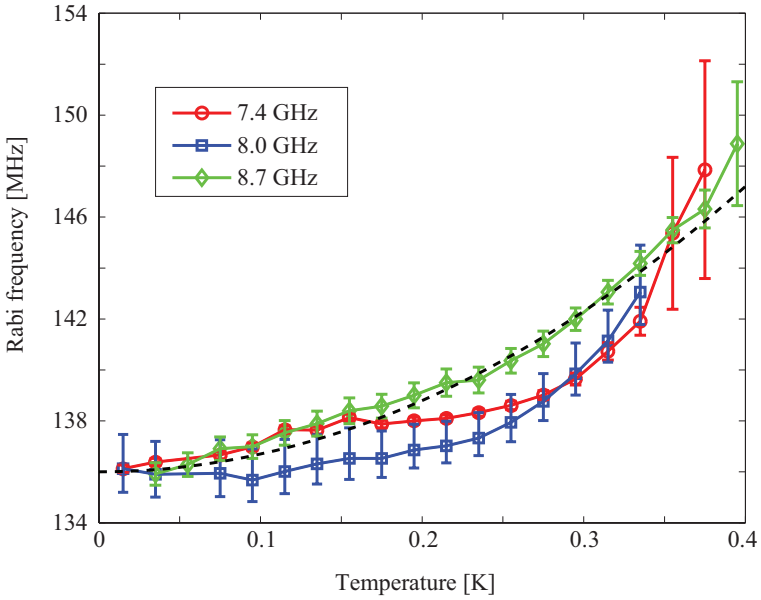

Figure 4.34: Rabi frequency temperature dependence obtained on sample UCSB−SiN. The data for 8.0 GHz and 8.7 GHz driving frequency were normalized to the data at 7.4 GHz. Real frequencies at 15 mK were 205 MHz at 8 GHz drive frequency and 155 MHz at 8.7 GHz. The dashed line is a quadratic fit to the data at 8.7 GHz.

The long coherence times of sample UCSB−SiN allow to measure precisely the temperature dependence of the Rabi oscillation frequency. For all chosen flux biases, we observe that the Rabi frequency increases slightly with temperature at approximately the same rate. This is shown in Fig. 4.34, for which the oscillation frequencies measured at microwave frequencies of 8.0 GHz and 8.7 GHz were multiplied by a constant factor for ease of comparison. The unscaled Rabi frequencies at 15 mK temperature were 205 MHz and 155 MHz at the microwave drive frequencies of 8.0 and 8.7 GHz, respectively. At 300 mK, the oscillation frequency increased by less than 4 %. The dashed line in the figure, which is a plot of the equation $\omega_R/2\pi = (136 + 70\,T^2)$ MHz, shows that the Rabi frequency increases approximately quadratically with temperature.

This Rabi frequency change can be explained by a temperature dependence of the qubit critical current, giving rise to a detuning between the external microwave and the qubit resonance. The smallness of the observed change of Rabi frequency however

renders the possibility to have a significant impact on the coherence times unlikely.

4.9.5 Ramsey fringes temperature dependence

To extract the influence of temperature on the dephasing time T_2^*, we measured the temperature dependence of the amplitude and decay time of Ramsey oscillations using sample UCSB−SiN. In the single performed experiment we were using the same parameters as discussed in Sec. 4.7.2, *i.e.* the microwave frequency of a $\pi/2$-pulse of 1.5 ns duration was 7.7 GHz.

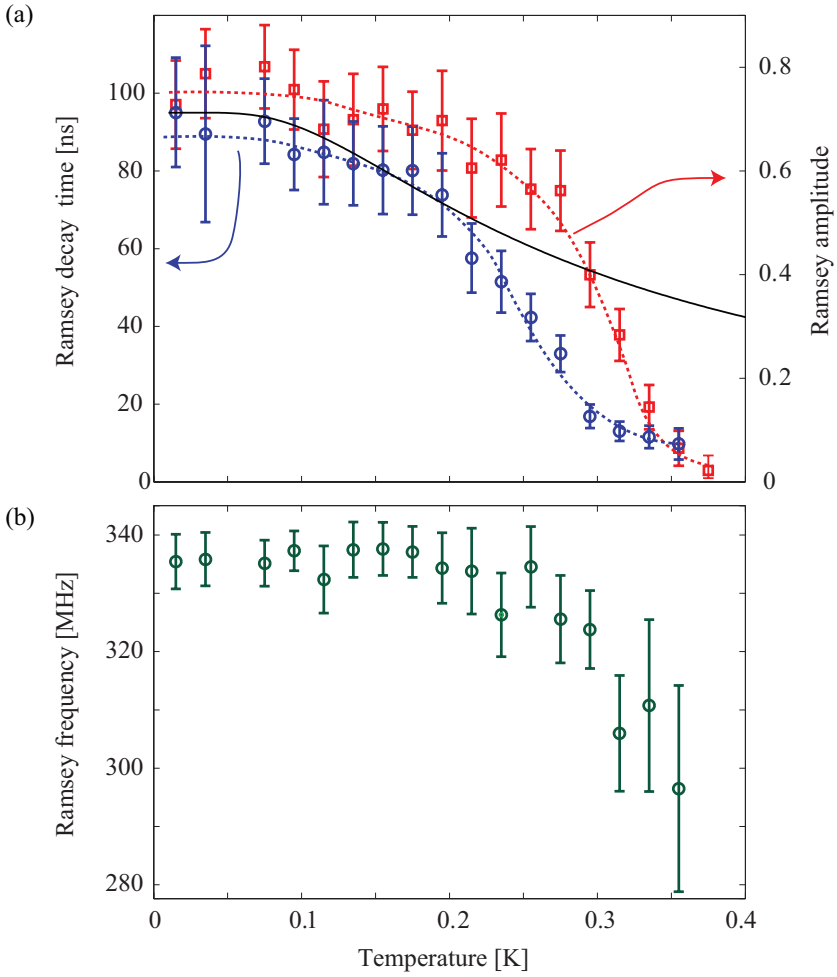

Figure 4.35: Ramsey oscillation parameters vs. temperature, measured using sample UCSB−SiN. (a) Ramsey oscillation amplitude (right axis) and decay time (left axis). Dashed lines are guides to the eye, solid line is a plot of $\tanh(\Delta E/2k_BT)$ using $\Delta E = 8.0$ GHz. (b) Frequency of Ramsey oscillation vs. temperature.

Figure 4.35 (a) shows that the decay time of Ramsey oscillation changes smoothly from about 90 ns below 100 mK temperature to $\approx$ 70 ns at 200 mK, followed by a rapid drop to below 20 ns around 300 mK temperature. The amplitude of Ramsey oscillation

was found to have a similar temperature dependence, shrinking rapidly above a temperature of about 250 mK and reaching zero at 375 mK, while only a small reduction is found below 200 mK. The general temperature dependence of Ramsey oscillation is quite similar to that of Rabi oscillation. The model given by Eq. (4.41), of which the $\tanh(\Delta E/2k_BT)$ - part is plotted as a solid line in Fig. 4.35 (a), does not predict any steep decay around $T_\Delta = \Delta E/k_B$ which we observe experimentally.

In contrast to the Rabi frequency which we found was increasing with temperature, the Ramsey oscillation frequency decreases above 250 mK, which is shown in Fig. 4.35 (b). This means that the Larmor frequency of the qubit decreases at higher temperatures, thus reducing the detuning to the external microwave which was adjusted to be about 335 MHz below the exact qubit resonance at 15 mK. A smaller Larmor frequency may be due to a reduced critical current or an increasing capacitance. Since this sample uses aluminum as electrode materials, a small reduction of the critical current above about 300 mK temperature is expected [120].

4.9.6 Temperature dependence of the energy relaxation time T_1

The energy relaxation time T_1 was measured as described in Sec. 4.5, using a resonant π-pulse whose duration was found from observation of coherent oscillation at same bias parameters and microwave frequency. The T_1 time was extracted by fitting the exponentially decaying excited state population when the readout pulse delay after the populating microwave pulse was increased. At each temperature we adjusted the amplitude of the readout pulse to compensate for thermal activation, while all other external parameters were kept fixed. We find that for both types of samples T_1 depends on temperature similarly to the decay time of Rabi oscillation.

Results of SiO_x - based samples

The temperature dependence of the T_1 time measured using sample `VTT30` is shown in Fig. 4.36 for two values of external flux bias, resulting in resonance at 16.5 GHz and 17.3 GHz microwave frequency, respectively. The data obtained using 16.5 GHz drive frequency shows the T_1-time to decrease smoothly from 1.9 ns at 15 mK temperature to about 1.5 ns at 800 mK. In contrast, using 17.3 GHz drive frequency, hardly any change of the T_1 time with temperature could be measured. Comparing this data to the expected relaxation rates given by Eq. (4.60), which are plotted in the figure by solid lines, shows that for both datasets the T_1-time depends on temperature weaker than it is expected for a two-state system. The data obtained in a shallow potential well at 16.5 GHz are closer the expectation than those measured in a deeper well at 17.3 GHz.

Results of SiN_x - based sample

The T_1 time has been measured in sample `UCSB-SiN` at two values of external flux bias which were identical to those used for observation of the Rabi oscillation temperature dependence discussed above. In both experiments using microwaves of 7.4 GHz and 8.0 GHz frequency, we find no change of the exponential decay time below 250 mK. This is shown in Fig. 4.37, in which the data obtained at 8.0 GHz have been multiplied by a factor of 1.49 to make them coincide at T=195 mK with the data taken at 7.4 GHz.

The T_1 time decreases rapidly above a temperature of 250 mK at an equal rate regardless of the external flux bias and reaches zero at about 350 mK. This behavior is

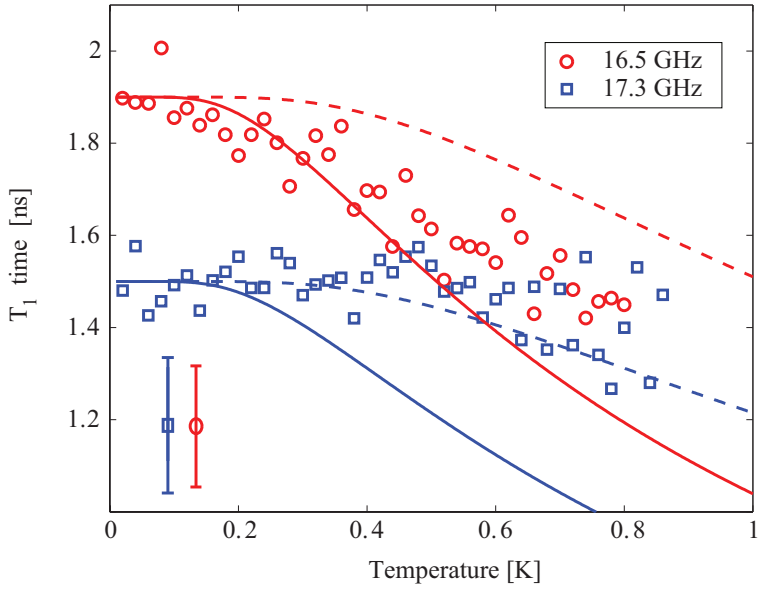

Figure 4.36: Temperature dependence of the T_1 time, measured on sample `VTT30` at an external flux bias resulting in resonance at the applied microwave frequency $\omega_{\mu w}/2\pi$ indicated in the legend. Solid lines: expected relaxation time Eq. (4.60) for $\Delta E = E_1 - E_0 = \hbar\omega_{\mu w}$, dashed lines: Eq. (4.60) for $\Delta E = 2\,\hbar\omega_{\mu w}$. Error bars in the inset represent an average confidence interval of the fits.

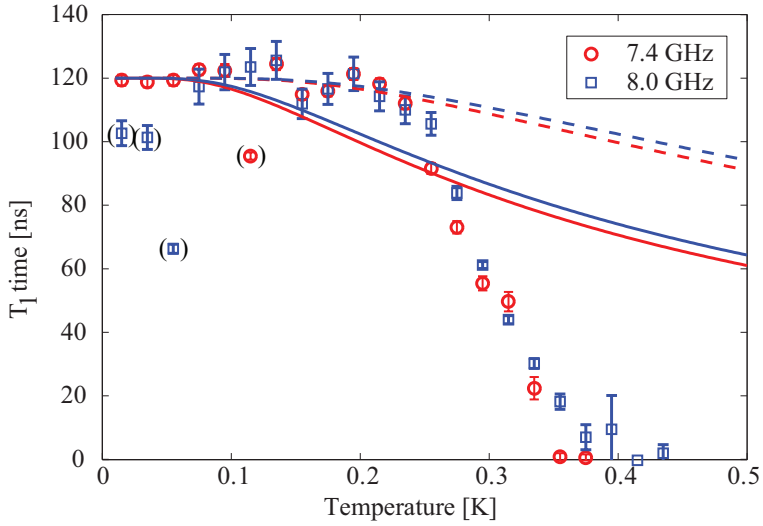

Figure 4.37: Temperature dependence of the T_1 time, measured on sample `UCSB-SiN` at an external flux bias resulting in resonance at the applied microwave frequency $\omega_{\mu w}/2\pi$ indicated in the legend. The 8.0 GHz data has been scaled by 1.49. Solid lines: expected relaxation time Eq. (4.60) for $\Delta E = E_1 - E_0 = \hbar\omega_{\mu w}$, dashed lines: Eq. (4.60) for $\Delta E = 2\,\hbar\omega_{\mu w}$.

very similar to the Rabi oscillation data taken at the same bias parameters. Accordingly, the expected temperature dependence of the relaxation time Eq. (4.60) does not fit the data.

4.10 Conclusions

In this section, we present the results of a systematic study of the temperature dependence of coherence times in phase qubits. In order to avoid thermal activation, at higher temperatures it is necessary to operate the qubit in a deep potential well. As this reduces the anharmonicity of the well, parasitic population of higher excited states can only be avoided for small drive amplitude and, accordingly, small Rabi frequency. Since our Nb/SiO_x - based samples have short coherence times of below 8 ns, we must drive them strongly to allow for observation of several periods of the Rabi oscillation before decoherence occurs. Therefore, these qubits were operated in the multi-level limit using the deep potential well required at higher temperatures. In contrast, the qubit sample which was made using SiN_x as a dielectric could be operated in the two-state quantum limit also at higher temperature. This is due to its much longer coherence time of about 100 ns.

We observed semi-classical Rabi-like oscillations in samples operated in the multi-level limit up to temperatures of 900 mK. Hereby, a loss of contrast due to thermal activation in the detector dc SQUID is avoided by a newly implemented data evaluation procedure which is based on weighted fitting of the switching-current distribution. A systematic evaluation of the temperature dependence of the Rabi-like oscillation amplitude and decay time shows that these values depend only weakly on temperature in samples operated in the multi-level limit. The same is true for the temperature dependence of the T_1 time.

The Al/SiN_x-sample which was operated in the two-level quantum limit showed a qualitatively different temperature dependence. The T_1 time, the decay time of Rabi oscillations and the T_2^* time, which was measured from a Ramsey fringe experiment, altogether rapidly decrease close to the temperature where the thermal energy $k_\mathrm{B}T$ is equal to the energy difference ΔE of the two qubit states. Below this temperature, which for the used samples was ≈ 400 mK, the coherence times depend only weakly on temperature. The Rabi oscillation amplitude in contrast showed a particular non-monotonic temperature dependence when the qubit was operated in very deep potential wells.

These peculiar results do not agree with the temperature dependence which is expected from models describing thermal population of the excited state and taking into account accelerated relaxation at higher temperatures. These models predict a stronger temperature dependence of decoherence for low temperatures. The rapid decrease of coherence time, which was observed in the sample operated in the two-level limit when $k_\mathrm{B}T \approx \Delta E$, also is not expected from these models.

We speculate that, at low temperatures, qubit coherence is limited by a mechanism which gets less effective at higher temperatures. Such a mechanism could be the coupling of the qubit to a bath of two-level fluctuators, which saturate at higher temperatures.

Summary

In this thesis, the coherent dynamics of superconducting phase quantum bits (qubits) are studied. A flux-biased phase qubit consists of a superconducting loop which is interrupted by a Josephson junction. The single degree of freedom of such a device is the phase difference φ of the superconducting order parameter across the junction, which depends on the magnetic flux threading the loop. As the logical states, a phase qubit uses two eigenstates of the Josephson phase φ which are kept confined in a metastable potential well. An externally applied magnetic flux is used to control the energy difference between the two qubit states.

I describe the phase qubit principles and designs of samples which were fabricated using a standard commercial photolithographic process. These samples were successfully operated in the quantum regime, demonstrating coherent qubit control by microwave and dc flux pulses.

The experimental methods required to operate phase qubits in the coherent quantum regime are discussed. For qubit readout, we implement a technique which is based on the application of a short magnetic flux pulse. It reaches a contrast close to 100%, which is limited only at higher temperatures by thermal activation occurring during the readout pulse. Microwave spectroscopy was used to characterize the energy level structure of the samples. For strong driving, we observed transitions to higher excited qubit states induced by multi-photon absorption processes. We evaluate the qubit coherence time T_2' by analyzing the resonance peak width dependence of microwave power. These experiments indicate the existence of decoherence sources which give rise to inhomogeneous resonance broadening.

A prominent source of phase qubit decoherence is energy relaxation, which we measure directly by observing the exponential decay of the excited state. The samples fabricated in standard technology had T_1 decay times of less than 8 ns. Short coherence times in this type of qubits are due to a coupling of the qubit to a large number of two-level fluctuators which reside in the oxide dielectrics used in junction fabrication. This is confirmed by our measurements on a sample which was made using SiN_x dielectric, showing a much longer T_1 time of about 100 ns.

Logical operations on the phase qubit are accomplished by resonant interaction with an applied microwave field, inducing coherent Rabi oscillation between the energy levels. We observe these oscillations in the time domain by driving the qubits with microwave pulses of varying duration. In standard samples fabricated using SiO_2-dielectric, the oscillations decay after a mean time of about 3 - 5 ns. In the SiN_x-based sample, we observe Rabi oscillation decay times of about 100 ns, in agreement with independent measurements of the UCSB group. This confirms that the noise level in

our experimental setup is low enough not to affect the coherent dynamics on the studied time scale.

For weakly driven qubits, the Rabi frequency depends linearly on drive amplitude, as expected. At strong driving, we find a saturation of the oscillation frequency at a value which is close to the anharmonicity of the qubit potential well, which indicates that higher excited states are taking part in coherent oscillations.

Using the high quality SiN_x-based sample, we demonstrate a Ramsey fringe experiment and characterize qubit decoherence caused by dephasing. In agreement with independent measurements, we find a dephasing time of $T_2^* \approx 90$ ns, which indicates that no significant sources of low-frequency noise exist in our experimental setup. In a similar experiment, we demonstrate an implementation of the phase gate which is based on the application of a short detuning flux bias pulse. This technique will be useful for qubit state tomography.

We performed a first systematic study of the temperature dependence of coherence times in phase qubits. In order to avoid thermal activation, at higher temperatures it is necessary to operate the qubit in a deep potential well. As this reduces the anharmonicity of the well, parasitic population of higher excited states can only be avoided for small drive amplitude and, accordingly, small Rabi frequency. Since our Nb/SiO_x-based samples have short coherence times of below 8 ns, we must drive them strongly for observation of several periods of the Rabi oscillation. Therefore, these qubits were operated in the multi-level limit using the deep potential wells required at higher temperatures. In contrast, the qubit sample which was made using SiN_x as a dielectric could be operated in the two-state quantum limit also at high temperature due to its long coherence time.

Semi-classical Rabi-like oscillations were observed in samples operated in the multi-level limit up to temperatures of 900 mK. Hereby, a loss of contrast due to thermal activation in the detector dc SQUID is avoided by a newly implemented data evaluation procedure which is based on weighted fitting of the switching-current distribution. A systematic evaluation of the temperature dependence of the Rabi-like oscillation amplitude and decay time shows that these values depend only weakly on temperature in samples operated in the multi-level limit. A similar result was obtained for the temperature dependence of the T_1 time.

In contrast, the Al/SiN_x-sample which was operated in the two-level quantum limit showed a qualitatively different temperature dependence. The T_1 time, the decay time of Rabi oscillations and the T_2^* time, which was measured from a Ramsey fringe experiment, altogether rapidly decrease close to the temperature where the thermal energy $k_{\mathrm{B}}T$ is equal to the energy difference ΔE of the two qubit states. Below this temperature, which for the used sample was ≈ 400 mK, the coherence times depend only weakly on temperature. The Rabi oscillation amplitude in contrast showed a particular non-monotonic temperature dependence when the qubit was operated in very deep potential wells.

These striking new results remain to be analyzed by theoretical models dealing with mechanisms that cause decoherence in superconducting Josephson junction qubits. Our experimental results also suggest that currently existing qubits can be operated at much higher temperatures than those reported till now, without degrading already achieved coherence times.

Zusammenfassung

Diese Dissertation fasst die Ergebnisse einer Untersuchung der quantenkohärenten Zeitentwicklung von supraleitenden Phasen-Quantenbits (Qubits) zusammen. Diese bestehen aus einer supraleitenden Schleife, die durch einen kleinen Josephson-Kontakt unterbrochen ist. Der einzige Freiheitsgrad eines solchen Systems ist die Phasendifferenz φ des supraleitenden Ordnungsparameters über dem Kontakt, welche vom magnetischen Fluss durch die Schleife abhängt. Ein Phasenqubit verwendet als logische Zustände zwei Eigenzustände der Josephson-Phase φ, wobei diese auf eine metastabile Potentialmulde beschränkt werden. Die Energiedifferenz zwischen den beiden Zuständen des Qubits wird durch einen angelegten magnetischen Fluss kontrolliert.

Ich beschreibe die Grundlagen des Phasen-Qubits und stelle das Design der Proben vor, welche mittels eines standardisierten photolithographischen Verfahrens kommerziell hergestellt wurden. Diese Proben wurden erfolgreich im Quantenregime betrieben, wobei die Manipulation des Qubitzustandes mittels Mikrowellen- und Magnetfeldpulsen demonstriert wurde.

Es werden die zum Betrieb von Phasen-Qubits im kohärenten Quantenregime notwendigen experimentellen Methoden dargelegt. Zum Auslesen des Qubits verwenden wir ein Verfahren, welches auf der Erzeugung eines kurzen Magnetfeldpulses basiert. Gemäß einer numerischen Untersuchung dieses Verfahrens erwarten wir eine hohe Auslesegenauigkeit von nahezu 100 %, die lediglich bei hohen Temperaturen durch thermische Aktivierung während der Dauer des Magnetfeldpulses begrenzt wird.

Wir charakterisieren die Struktur der Energieniveaus der Proben mittels Mikrowellenspektroskopie. Im Fall großer Mikrowellenamplituden beobachten wir Übergänge zu höher angeregten Qubitzuständen, welche durch Mehrphotonenabsorption entstehen. Wir haben die Kohärenzzeit T_2' der Proben durch eine Analyse der Abhängigkeit der Resonanzlinienbreite von der Mikrowellenamplitude bestimmt. Diese Experimente deuten darauf hin, dass in den getesteten standard-Qubits die Ursache der Dekohärenz auch zu inhomogener Resonanzlinienverbreiterung führt.

Die hauptsächliche Ursache von Dekohärenz bei Phasen-Qubits ist Energierelaxation. Diese führt zum Zerfall des angeregten Qubitzustandes, welchen wir im zeitlichen Verlauf direkt beobachten. Die in standardisierten Prozessen hergestellten Qubits zeigten eine Zerfallszeit T_1 von weniger als 8 ns. Solch kurze Kohärenzzeiten sind in diesen Proben bedingt durch die Kopplung des Qubits an eine grosse Zahl von zwei-Niveau Zuständen, welche im SiO_2-Dielektrikum des Josephson-Kontaktes bestehen. Dies wurde durch unsere Messungen an einem Qubit bestätigt, welches in einem speziellen Prozess unter Verwendung eines SiN_x-Dielektrikums hergestellt wurde und entsprechend lange Kohärenzzeiten von $T_1 \approx 100$ ns zeigt.

Logische Qubit-Operationen werden durch resonante Wechselwirkung mit einem angelegten Mikrowellenfeld erreicht, die zur Erzeugung von Rabi-Oszillationen in der Besetzung der Energieniveaus führt. Wir beobachten diese Oszillationen im zeitlichen Verlauf unter Verwendung eines Mikrowellenpulses variabler Dauer. In herkömmlichen Proben, die unter Verwendung eines SiO_2-Dielektrikums hergestellt wurden, zeigen diese Oszillationen eine Abklingzeit von 3 bis 5 ns. In den Proben, die auf SiN_x-Dielektrikum basieren, beobachten wir Abklingzeiten der Rabi-Oszillation von etwa 100 ns in Übereinstimmung mit unabhängigen Messungen. Dieses Ergebnis bestätigt, dass der Rauschpegel unseres experimentellen Aufbaus niedrig genug ist, um die kohärente Qubit-Dynamik auf einer Zeitskala von 100 ns nicht zu beeinträchtigen.

Bei kleiner angelegter Mikrowellenleistung messen wir die erwartete lineare Abhängigkeit der Rabi-Frequenz von der Amplitude der Anregung. Bei höheren Leistungen beobachten wir eine Sättigung der Oszillationsfrequenz bei einem Wert nahe der Anharmonizität der die Qubitzustände enthaltenden Potentialmulde. Dies deutet darauf hin, dass bei diesen Leistungen höhere Qubitzustände angeregt werden und an der kohärenten Oszillation teilnehmen.

Unter Verwendung des hochwertigen, auf SiN_x-basierenden Qubits demonstrieren wir ein Experiment zur Messung von Ramsey-Oszillationen, welches erlaubt, den Anteil von Dephasierung an der Dekohärenz zu bestimmen. In Übereinstimmung mit unabhängigen Messungen beobachten wir eine Dephasierungszeit von $T_2^* \approx 90$ ns, was darauf schliessen lässt, dass in unserem experimentellen Aufbau keine signifikanten Quellen von niederfrequentem Rauschen vorhanden sind. In einem ähnlichen Experiment zeigen wir die Realisierung des Phasengatters, welches auf der Erzeugung eines kurzen Magnetfeldpulses zur Verstimmung des Qubits basiert. Diese Methode wird sich für tomographische Messungen des Qubitzustandes als nützlich erweisen.

Wir präsentieren die erste systematische Untersuchung der Temperaturabhängigkeit der Kohärenzzeiten in Phasenqubits. Bei hohen Temperaturen muss thermische Aktivierung dadurch vermieden werden, dass das Qubit in einer tiefen Potentialmulde betrieben wird. Da dies die Anharmonizität der Potentialmulde verkleinert, kann eine ungewünschte Anregung hoher Qubitzustände nur bei kleiner Anregungsamplitude und enstprechend kleiner Rabi-Frequenz vermieden werden. Da unsere auf Nb/SiO_x-basierenden Proben sehr kurze Kohärenzzeiten von weniger als 8 ns haben, ist es notwendig, diese mit hoher Anregungsamplitude zu betreiben, um einige Perioden der Rabi-Oszillation beobachten zu können. Es ist deshalb unmöglich, diese Proben als Zweiniveausystem in den bei hohen Temperaturen notwendigen tiefen Potentialmulden zu betreiben. Im Unterschied dazu ist es möglich, die über ein Dielektrikum aus SiN_x verfügende Probe auch bei höheren Temperaturen im Zweiniveau-Quantenlimit zu betreiben.

Unter Verwendung der als Mehrniveausystem betriebenen Proben konnten wir semiklassische Oszillationen, welche Rabioszillationen ähneln, bis zu einer maximalen Temperatur von 900 mK beobachten. Hierbei konnte eine Abnahme des Messkontrastes aufgrund von thermischer Aktivierung im Detektor-DC-SQUID durch eine neuartige Methode der Datenauswertung vermieden werden, welche auf einer Regressionsanalyse der Schaltstrom-Wahrscheinlichkeitsverteilung basiert. Eine systematische Auswertung der Temperaturabhängigkeiten von Amplitude und Abklingzeit der semiklassischen Oszillationen sowie der Lebenszeit des angeregten Zustandes T_1 erbrachte, dass diese Werte nur schwach von der Temperatur abhängen.

Im Gegensatz hierzu zeigt die als Zweiniveau-System betriebene Probe eine qualitativ unterschiedliche Temperaturabhängigkeit. Die T_1-Zeit, die Abklingzeit der Rabi-

Oszillation als auch die Abklingzeit T_2^* der Ramsey-Oszillation nahmen schnell ab sobald die Probentemperatur einen Wert erreichte, bei dem die thermische Energy $k_{\mathrm{B}}T$ gleich der Energiedifferenz ΔE zwischen den beiden Qubitzuständen ist. Unterhalb dieser Temperatur, welche für die verwendete Probe bei ca. 400 mK liegt, hängen die Kohärenzzeiten nur schwach von der Temperatur ab.

Diese bemerkenswerten neuen Ergebnisse müssen in theoretischen Modellen Berücksichtigung finden, die die Dekohärenz von auf Josephson-Kontakten basierenden Qubits beschreiben. Unsere Experimente zeigen darüber hinaus, dass momentan verfügbare Qubits bei sehr viel höheren Temperaturen betrieben werden können als es bisher bekannt war.

Bibliography

[1] E. Schrödinger, Naturwissenschaften **48, 49, 50**, 807, 823, 844 (1935).

[2] R. Voss and R. Webb, Phys. Rev. Lett. **47**, 265 (1981).

[3] M. Devoret, J. Martinis, and J. Clarke, Phys. Rev. Lett. **55**, 1908 (1985).

[4] J. M. Martinis, M. H. Devoret, and J. Clarke, Phys. Rev. Lett. **55**, 1543 (1985).

[5] M. H. Devoret, D. Esteve, and J. M. Martinis, Phys. Rev. B **36**, 58 (1987).

[6] J. E. Mooij, T. P. Orlando, L. Levitov, L. Tian, C. H. van der Wal, and S. Lloyd, Science **285**, 1036 (1999).

[7] J. R. Friedman, V. Patel, W. Chen, S. K. Tolpygo, and J. E. Lukens, nature **406**, 43 (2000).

[8] A. Barone and G. Paternò, *Physics and Applications of the Josephson Effect* (Wiley, New York, 1982).

[9] J. Clarke and A. Braginski, *SQUID Handbook*, vol. 1 (WILEY-VCH, 2004).

[10] J. Martinis, S. Nam, J. Aumentado, and C. Urbina, Phys. Rev. Lett. **89**, 117901 (2002).

[11] I. Chiorescu, Y. Nakamura, C. J. Harmans, and J. E. Mooij, Science **299**, 186 (2003).

[12] Y. Nakamura, Y. A. Pashkin, and J. S. Tsai, nature **398**, 786 (1999).

[13] D. Vion, A. Aassime, A. Cottet, P. Joyez, H. Pothier, C. Urbina, D. Esteve, and M. Devoret, Science **296**, 286 (2002).

[14] Hypres Inc., Elmsford, NY 10523, U.S.A.

[15] A. Steane, quant-ph/9708022 (1997).

[16] E. Rieffel and W. Polak, quant-ph/9809016 (1998).

[17] R. Feynman, Int. J. Theor. Phys. **21** (1982).

[18] D. Deutsch, Proc. R. Soc. Lond. **400**, 97 (1985).

[19] M. A. Nielsen and I. L. Chuang, *Quantum Computation and Quantum Information* (Cambridge University Press, 2000).

[20] R. Hughes *et. al.*, *A quantum information science and technology roadmap* (2004), http://qist.lanl.gov/qcomp_map.shtml.

[21] D. P. DiVincenzo, Fortschritte der Physik **48**, 771 (2000), http://arxiv.org/abs/quant-ph/0002077.

[22] K. Likharev and V. Semenov, IEEE Trans. Appl. Supercond. **1**, 3 (1991).

[23] S. O. Valenzuela, W. D. Oliver, D. M. Berns, K. K. Berggren, L. S. Levitov, and T. P. Orlando, Science **314**, 1589 (2006).

[24] P. Shor, Phys. Rev. A **52**, 2493 (1995).

[25] A. Steane, Phys. Rev. Lett. **77**, 793 (1996).

[26] R. C. Bialczak, R. McDermott, M. Ansmann, M. Hofheinz, N. Katz, E. Lucero, M. Neeley, A. D. O'Connell, H. Wang, A. N. Cleland, *et al.*, *1/f flux noise in josephson phase qubits* (2007), http://www.citebase.org/abstract?id=oai:arXiv.org:0708.2125.

[27] R. Simmonds, K. Lang, D. A. Hite, S. Nam, D. P. Pappas, and J. Martinis, Phys. Rev. Lett. **93**, 0770031 (2004).

[28] S. Lloyd, Phys. Rev. Lett. **75**, 346 (1995).

[29] R. McDermott, R. W. Simmonds, M. Steffen, K. B. Cooper, K. Cicak, K. D. Osborn, S. Oh, D. P. Pappas, and J. M. Martinis, Science **307**, 1299 (2005).

[30] J. Clarke, T. L. Robertson, B. Plourde, A. García-Martinez, P. Reichardt, D. V. Harlingen, B. Chesca, R. Kleiner, Y. Makhlin, G. Schön, *et al.*, Physica Scripta **T102**, 173 (2002).

[31] T. Filippov, S. Tolpygo, J. Mannik, and J. Lukens, IEEE Trans. Appl. Supercond. **13**, 1005 (2003).

[32] M. G. Castellano, F. Chiarello, R. Leoni, D. Simeone, G. Torrioli, C. Cosmelli, and P. Carelli, Applied Physics Letters **86**, 152504 (2005).

[33] A. Blais, A. M. van den Brink, and A. M. Zagoskin, Phys. Rev. Lett. **12**, 127901 (2003).

[34] K. B. Cooper, M. Steffen, R. McDermott, R. Simmonds, S. Oh, D. Hite, D. Pappas, and J. Martinis, Phys. Rev. Lett. **93**, 180401 (2004).

[35] J. Lisenfeld, *Probing quantum states in josephson junctions by microwaves* (2003), diploma thesis, Friedrich-Alexander Universität Erlangen-Nürnberg.

[36] J. Claudon, F. Balestro, F. Hekking, and O. Buisson, Phys. Rev. Lett. **93**, 187003 (2004).

[37] B. Josephson, Phys. Lett. **1**, 251 (1962).

[38] W. C. Stewart, Appl. Phys. Lett **12**, 277 (1968).

[39] D. E. McCumber, J. Appl. Phys. **39**, 3113 (1968).

[40] M. Weihnacht, Phys. Stat. Sol. **32**, K169 (1969).

[41] M. Devoret, D. Esteve, and C. Urbina, *Macroscopic Quantum Effects in the Current-Biased Josephson Junction* (Elsevier Science Publishers, 1992), chap. 6.

[42] M. Devoret, J. M. Martinis, D. Esteve, and J. Clarke, Phys. Rev. Lett. **53**, 1260 (1984).

[43] J. E. Marchese, M. Cirillo, and N. Grønbech-Jensen, Europ. Phys. Journ. on Special Topics **147**, 333 (Aug. 2007), arXiv:0708.3701.

[44] M. V. Fistul and A. V. Ustinov, Phys. Rev. B **63**, 024508 (2000).

[45] L. D. Landau and E. M. Lifschitz, *Mechanik* (Akademie-Verlag Berlin, 1976).

[46] A. Wallraff, T. Duty, A. Lukashenko, and A. V. Ustinov, Phys. Rev. Lett. **90**, 370031 (2003).

[47] H. A. Kramers, Physica **7**, 284 (1940).

[48] H. Grabert, P. Olschowski, and U. Weiss, Phys. Rev. B **36**, 1931 (1987).

[49] M. Büttiker, E. Harris, and R. Landauer, Phys. Rev. B **28**, 1268 (1983).

[50] K. K. Likharev, *Dynamics of Josephson junctions and circuits* (Gordon and Breach Science, 1986).

[51] A. O. Caldeira and A. J. Leggett, Phys. Rev. Lett. **46**, 211 (1981).

[52] A. O. Caldeira and A. J. Legget, Ann. of Phys. **149**, 374 (1983).

[53] P. Silvestrini, V. G. Palmieri, B. Ruggiero, and M. Russo, Phys. Rev. Lett. **79**, 3046 (1997).

[54] I. Affleck, Phys. Rev. Lett. **46**, 388 (1981).

[55] J. M. Martinis, M. H. Devoret, and J. Clarke, Phys. Rev. B **35**, 4682 (1987).

[56] C. Cohen-Tannoudji, B. Diu, and F. Laloë, *Quantum Mechanics*, vol. 1 (Wiley-Interscience, 1977).

[57] S. Han, Y. Yang, and X. e. a. Chu, Science Magazine **293**, 1457 (2001).

[58] J. M. Martinis, S. Nam, J. Aumentado, K. M. Lang, and C. Urbina, Phys. Rev. B. **67**, 094510 (2003).

[59] C. H. van der Wal, A. C. J. ter Haar, F. K. Wilhelm, R. N. Schouten, C. Harmans, T. P. Orlando, S. Lloyd, and J. E. Mooij, Science **290**, 773 (2000).

[60] T. L. Robertson, *Fundamentals of Flux-based Quantum Computing*, Ph.D. thesis, University of California, Berkely (2005).

[61] R. Simmonds, D. Hite, R. McDermott, M. Steffen, K. Cooper, K. Lang, J. Martinis, and D. Pappas, *Quantum Computation: solid state systems* (Springer Verlag, Berlin, 2005), chap. Junction Materials Research using Phase Qubits.

[62] D. Esteve, M. H. Devoret, and J. M. Martinis, Phys. Rev. B **34**, 158 (1986).

[63] A. Berkley, *A Josephson junction qubit*, Ph.D. thesis, University of Maryland (2003).

[64] R. M. Lewis, H. Paik, S. K. Dutta, T. A. Palomaki, K. Mitra, B. K. Cooper, A. Przybysz, C. J. Anderson, J. R.and Lobb, and F. C. Wellstood, *Quantum Information and Computation IV* (2006), vol. 6244 of *Proceedings of the SPIE*, chap. Some properties of a dc SQUID qubit.

[65] K. Lang, S. Nam, J. Aumentado, C. Urbina, and J. M. Martinis, IEEE Transactions on Applied Superconductivity **13**, 2003 (2003).

[66] J. Zimmermann and A. Silver, Phys. Rev. **157**, 317 (1967).

[67] A. G. Kofman, Q. Zang, J. M. Martinis, and A. N. Korotkov, Phys. Rev. B **75**, 014524 (2007).

[68] Q. Zhang, A. G. Kofman, J. Martinis, and A. N. Korotkov, Phys. Rev. B **74**, 2145181 (2006).

[69] R. Rouse, S. Han, and J. E. Lukens, Phys. Rev. Lett. **75**, 1614 (Aug 1995).

[70] K. Likharev, Physica B p. 1079 (1981).

[71] V. Lefevre-Seguin, E. Turlot, C. Urbina, D. Esteve, and M. H. Devoret, Phys. Rev. B. **46**, 5507 (1992).

[72] F. Chiarello, P. Carelli, M. G. Castellano, C. Cosmelli, L. Gangemi, R. Leoni, S. Poletto, D. Simeone, and G. Torrioli, Supercond. Sci. Tech. **18**, 1370 (2005).

[73] V. Schmidt, P. Müller, and A. Ustinov, *The Physics of Superconductors* (Springer Verlag Berlin, 1997).

[74] V. Lefevre-Seguin, E. Turlot, C. Urbina, D. Esteve, and M. Devoret, Phys. Rev. B **91**, 5507 (1992).

[75] F. Balestro, J. Claudon, J. Pekola, and O. Buisson, Phys. Rev. Lett. **46**, 158301 (2003).

[76] C. van der Wal, F. Wilhelm, C. Harmans, and J. Mooij, Eur. Phys. J. B **31**, 111 (2003).

[77] T. A. Fulton and L. N. Dunkleberger, Phys. Rev. B **9**, 4760 (1974).

[78] A. Wallraff, A. Lukashenko, C. Coqui, T. Duty, and A. V. Ustinov, Rev. Sci. Instr. **74**, 3740 (2003).

[79] T. L. Robertson, B. L. T. Plourde, T. Hime, S. Linzen, P. A. Reichardt, F. K. Wilhelm, and J. Clarke, Phys. Rev. B **72**, 024513 (2005).

[80] T. Hime, P. Reichardt, B. Plourde, T. Robertson, C.-E. Wu, A. Ustinov, and J. Clarke, Science **314**, 1427 (2006).

[81] VTT Technical Research Center, Finland.

[82] Whiteley Research Inc., Sunnyvale, CA 94086, U.S.A., *FastHenry v3.0wr*.

[83] E. Il'ichev, N. Oukhanski, A. Izmalkov, T. Wagner, M. Grajcar, H.-G. Meyer, A. Y. Smirnov, A. M. van den Brink, M. H. S. Amin, and A. M. Zagoskin, Phys. Rev. Lett **91**, 097906 (2003).

[84] M. Steffen, M. Ansmann, R. McDermott, N. Katz, R. Bialczak, E. Lucero, M. Neeley, E. Weig, A. Cleland, and J. Martinis, Phys. Rev. Lett. **97**, 050502 (2006).

[85] Aeroflex / Inmet Inc., Ann Arbor, MI 48103, U.S.A., http://www.aeroflex-inmet.com.

[86] Huber + Suhner GmbH, D-82024 Taufkirchen, Germany, http://www.hubersuhner.de.

[87] A. Lukashenko and A. V. Ustinov, to appear in Rev. Sci. Instr. (2007).

[88] Vacuumschmelze GmbH & Co. KG, D-63450 Hanau, http://www.vacuumschmelze.de.

[89] Texas Instruments, *DAC714 datasheet*, http://www-s.ti.com/sc/ds/dac714.pdf.

[90] Maxim Integrated Products, http://www.maxim-ic.com.

[91] Stanford Research Systems, *SR 620 universal time interval counter*.

[92] Y. S. Greenberg, A. Izmalkov, M. Grajcar, E. Il'ichev, W. Krech, and H.-G. Meyer, Phys. Rev. B **66**, 224511 (2002).

[93] A. Lupaşcu, C. J. Verwijs, R. N. Schouten, C. J. Harmans, and J. E. Mooij, Phys. Rev. Lett. **93**, 177006 (2004).

[94] The Mathworks Inc., http://www.mathworks.com.

[95] Marki Microwave Inc., *M8-0420*, http://www.markimicrowave.com.

[96] ARRA inc., *power divider model 0200-2*, http://www.arra.com/.

[97] D. Schwartz, B. Sen, C. Archie, and J. Lukens, Phys. Rev. Lett. **55**, 1547 (1985).

[98] J. Kurkijärvi, Phys. Rev. B **6**, 832 (1972).

[99] H. Grabert, P. Olschowski, and U. Weiss, Phys. Rev. B. **32**, 2712 (1985).

[100] H. Grabert, P. Olschowski, and U. Weiss, Phys. Rev. Lett. **57**, 265 (1986).

[101] R. McDermott, M. Steffen, M. Ansmann and J.M. Martinis, private communication.

[102] F. Bloch, Phys. Rev. **70**, 460 (1946).

[103] M. Goordon, *Theory of Josephson persistent-current qubits with driving and dissipation*, Master's thesis, Delft University of Technology (2002).

[104] S. Saito, M. Thorwart, H. Tanaka, M. Ueda, H. Nakano, K. Semba, and H. Takayanagi, Phys. Rev. Lett. **93**, 037001 (2004).

[105] Y. Nakamura, Y. A. Pashkin, and J. S. Tsai, Phys. Rev. Lett. **87**, 246601 (2002).

[106] A. Ratchov, *Étude du couplage de petits systèmes quantiques avec leur environnement: fluctutations et décohérence à basse température*, Ph.D. thesis, Université Joseph Fourier, Grenoble (2005).

[107] M. Weissman, Rev. Mod. Phys. **60**, 537 (1988).

[108] A. Abragam, *The Principles of Nuclear Magnetism* (Oxford University Press, Glassgow, 1961).

[109] F. Bloch and A. Siegert, Phys. Rev. **57**, 522 (1940).

[110] L. Ku and C. Yu, Phys. Rev. B **72**, 024526 (2005).

[111] M. Amin, Low Temp. Phys. **32**, 198 (2006).

[112] F. Meier and D. Loss, Phys. Rev. B **71**, 094519 (2005).

[113] L. Tian and S. Lloyd, Phys. Rev. A **62**, 050301 (2000).

[114] N. F. Ramsey, Phys. Rev. **78**, 695 (1950).

[115] L. Tian, S. Lloyd, and T. Orlando, Phys. Rev. B **65**, 144516 (2002).

[116] F. K. Wilhelm, M. J. Storcz, C. H. van der Wal, C. J. P. M. Harmans, and J. E. Mooij, Adv. Solid State Phys. **43**, 763 (2003).

[117] A. Leggett, S. Chakravarty, A. Dorsey, M. Fisher, A. Garg, and W. Zwerger, Rev. Mod. Phys. **59**, 1 (1987).

[118] M. Grifoni, E. Paladino, and U. Weiss, Eur. Phys. J. B **10**, 719 (1999).

[119] C. Slichter, *Principles of magnetic resonance* (Springer Verlag, 1990).

[120] V. Ambegaokar and A. Baratoff, Phys. Rev. Lett. **10**, 486 (1963).

List of Publications

- J. Lisenfeld, A. Lukashenko, and A.V. Ustinov, *High-contrast readout of superconducting qubits beyond the single-shot resolution limit*, to be published in Appl. Phys. Lett. (2007)

- J. Lisenfeld, A. Lukashenko, M. Ansmann, J. M. Martinis, and A.V. Ustinov, *Temperature dependence of coherent oscillations in Josephson phase qubits*, Phys. Rev. Lett. **99**, 170504 (2007)

- X. Jin, J. Lisenfeld, Y. Koval, A. Lukashenko, A.V. Ustinov, and P. Müller, *Enhanced Macroscopic Quantum Tunneling in $Bi_2Sr_2CaCu_2O_{8+\delta}$ Intrinsic Josephson Junction Stacks*, Phys. Rev. Lett. **96**, 177003 (2006)

- J. Lisenfeld, A. Lukashenko, and A.V. Ustinov, *Macroscopic quantum coherence in rf-SQUIDs*, Proceedings of the International Symposium on Mesoscopic Superconductivity and Spintronics, NTT R&D Center, Atsugi, Kanagawa, Japan (2006)

- B. Ivlev, G. Pepe, R. Latempa, A. Barone, F. Barkov, J. Lisenfeld, and A.V. Ustinov, *Extreme multiphoton phenomena in Josephson junctions: Euclidean resonance*, Phys. Rev. B **72**, 094507 (2005)

- A. Wallraff, A. Lukashenko, J. Lisenfeld, A. Kemp, M. Fistul, Y. Koval, and A.V. Ustinov, *Quantutm dynamics of a single vortex*, Nature **425**, 155 (2003).